Elastic-Resonator-Interference-Stress-Microscopy (ERISM)

Method and Application to Cells of the Nervous System

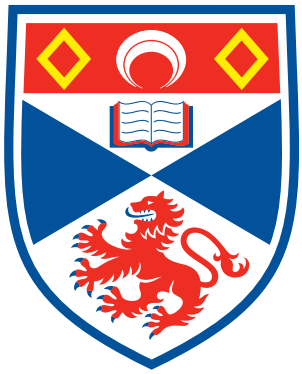

University of
St Andrews

Philipp Liehm

This thesis is submitted in partial fulfilment for the degree of

Doctor of Philosophy

Department of Physics and Astronomy

24 February 2017

Abstract

The forces biological cells apply to their environment are recognised to be critical during processes like migration, division, wound healing, and stem cell differentiation. Methods to measure these forces have been extremely valuable in contributing to our understanding of cell-substrate and cell-cell interactions. However, existing force sensing techniques struggle to measure forces cells apply perpendicular to the plane of their substrate although these out-of-plane forces have been demonstrated to be important in many processes. In addition, most currently used force sensing techniques require fluorescence imaging which can lead to photo-toxic effects if high frame rates are required. Finally, many methods require detaching of cells after the measurement which prevents measuring the same cells repeatedly or using immunostaining, which is an important tool for linking biomechanical and biochemical observations.

In this thesis, we introduce a novel high-throughput and low-light-intensity force sensing technique which is inherently well suited to measure vertical forces. Elastic-Resonator-Interference-Stress-Microscopy (ERISM) measures the spatially resolved reflectance of an elastic micro-cavity. With fully automated hyperspectral imaging and data analysis supported by transfer-matrix modelling, this allows tracking of nanometre thickness changes across a large area of the cavity. By combining Atomic-Force-Microscopy with a Finite-Element-Method, we extract basic material properties of the micro-cavities to calculate stress and force.

Using the example of different neural cells, we provide experimental evidence that ERISM measurements can be performed over hours at high frame rates or repeatedly over weeks for the same sample to investigate a variety of cellular processes like cell spreading, growth

cone migration, and stem cell differentiation. We perform immunostaining for cell specific markers on ERISM micro-cavities as detaching of the cells is not required. Furthermore, we find that the high throughput of ERISM allows us to find significant differences between wild-type and knock-out cell populations for a gene associated with dyslexia.

Declaration

1. Candidate's declarations:

I, Philipp Liehm, hereby certify that this thesis, which is approximately 45.000 words in length, has been written by me, and that it is the record of work carried out by me, or principally by myself in collaboration with others as acknowledged, and that it has not been submitted in any previous application for a higher degree.

I was admitted as a research student in August, 2013 and as a candidate for the degree of Doctor of Philosophy in August, 2013; the higher study for which this is a record was carried out in the University of St Andrews between 2013 and 2016.

Philipp Liehm 2017/02/24

2. Supervisor's declaration:

I hereby certify that the candidate has fulfilled the conditions of the Resolution and Regulations appropriate for the degree of Doctor of Philosophy in the University of St Andrews and that the candidate is qualified to submit this thesis in application for that degree.

Prof. Malte C. Gather 2017/02/24

3. Permission for publication:

In submitting this thesis to the University of St Andrews I understand that I am giving permission for it to be made available for use in accordance with the regulations of the University Library for the time being in force, subject to any copyright vested in the work not being affected thereby. I also understand that the title and the abstract will be published, and that a copy of the work may be made and supplied to any bona fide library or research worker, that my thesis will be electronically accessible for personal or research use unless exempt by award of an embargo as requested below, and that the library has the right to migrate my thesis into new electronic forms as required to ensure continued access to the thesis. I have obtained any third-party copyright permissions that may be required in order to allow such access and migration, or have requested the appropriate embargo below.

The following is an agreed request by candidate and supervisor regarding the publication of this thesis:

No embargo on the print copy but embargo on all of the electronic copy for a period of 2 years on the following ground: publication would preclude future publication.

Prof. Malte C. Gather 2017/02/24 Philipp Liehm 2017/02/24

Acknowledgements

First, I want to thank Professor Malte C. Gather. He not only gave me the opportunity to be part of his young scientist group, where I could do my PhD on such a challenging and fascinating topic, but he is also one of the most inspiring people I met so far. His intuition to give me the right pointers at the right time to push my research further has amazed me numerous times. I learned a lot from him through his critical thinking in all the discussions we had, and I am very grateful for the freedom and the support he gave me to pursue the projects I was interested in. Malte, you have been a great mentor to me, I know I could not have been luckier! Thank you for everything!

I like to thank Nils M. Kronenberg for pushing with me the ERISM project from scratch towards a great technique. Working with him taught me a lot to become a better scientist and he certainly was a fun officemate! Thank you Nils that I could always count on you that you will run into the bugs of my software:)!

Anja Steude and Andrew Morton did their best to make me at least partially a biologist, this was extremely helpful for me as this allowed me to do most of my experiments independently!

I thank Silvia Paracchini and Rebeca Diaz Vasquez for pulling me even further towards the edge of biology. My PhD greatly benefited from their support in starting stem cell experiments in our own lab and from the collaboration on their fascinating project which allowed me to perform measurements on KIAA0319 wild-type and knock-out cells.

Thanks to everyone else in the GatherLab: Laura, Marcel, Markus, Alasdair, Andrew (Meek), Joanna, Caroline, Jan, and Elena, I will look back to such a fun group!

I also thank my second supervisor Andrea Di Falco. Although I was never in need to consult him because of problems with my supervisor, he made sure I knew that I could come to him any time, and I am happy that I could contribute a bit to his work on coccolithophores.

I like to thank Kristian Franze and his group for all the fruitful discussions and for the chance to visit his lab in Cambridge to learn how traction-force-microscopy measurements are performed.

My gratitude also goes to the EPSRC, without the funding I would not have been able to do this PhD.

The Capoeira Society is what kept my body going, thank you Bruno for teaching us this great martial arts dance.

St Andrews is a small place, and the three years here might have been a bit too long if it would not have been for the St Andrews Tango Society. Ewa Bieniecka, it was such a fortune to meet you here, creating the tango society together with you opened a whole new world for me, three years ago I could not have imagined myself to teach tango to so many other people! Dancing with the people here in St Andrews gave me the right work-life balance and I am very happy that I can now call so many of the people who wanted to learn tango my friends. In particular I like to thank Max and Naomi, who have always been amazing partners for discussions about physics or anything else, not to mention their cooking skills!

Franzi and Sarah, you have been the best friends I could possibly ask for! Thank you for visiting me, thank you for being such relaxed friends, I am so much looking forward to see you more often again!

Viliina, you have been a wonderful loving person and partner to me. Thank you for sharing your life with me here in St Andrews, I am very grateful that I met you.

I thank my parents and the rest of my family who has been very understanding about the long times I did not visit Germany. I am lucky to have you!

List of Publications

1. *Philipp Liehm*, Caroline Murawski, Mauro Furno, Björn Lüssem, Karl Leo, and Malte C. Gather: “Comparing the emissive dipole orientation of two similar phosphorescent green emitter molecules in highly efficient organic light-emitting diodes”, *Appl. Phys. Lett.* 101, 253304 (2012).

2. Caroline Murawski, *Philipp Liehm*, Karl Leo, and Malte C. Gather: “Influence of cavity thickness and emitter orientation on the efficiency roll-off of phosphorescent organic light-emitting diodes”, *Adv. Funct. Mater.* 24, 1117 (2014).

3. Arko Graf, *Philipp Liehm*, Caroline Murawski, Simone Hofmann, Karl Leo, and Malte C. Gather: “Correlating the transition dipole moment orientation of phosphorescent emitter molecules in OLEDs with basic material properties”, *J. Mater. Chem. C* 2, 10298 (2014)

4. Marcel Schubert, Anja Steude, *Philipp Liehm*, Nils M Kronenberg, Markus Karl, Elaine C. Campbell, Simon J. Powis, Malte C. Gather: "Lasing within Live Cells Containing Intracellular Optical Microresonators for Barcode-Type Cell Tagging and Tracking", *Nano Letters* 15,5647 (2015)

5. Nils M. Kronenberg, *Philipp Liehm*, Anja Steude, Johanna A. Knipper, Jessica G. Borger, Giuliano Scarcelli, Kristian Franze, Simon J. Powis, Malte C. Gather: "Long-Term Imaging of Cellular Forces with High Precision by Elastic Resonator Interference Stress Microscopy", submitted (2016)

6. *Philipp Liehm*, Nils M. Kronenberg, Malte C. Gather: in preparation (2016)

Table of contents

Chapter 1

Introduction

It has been known to humans for over two thousand years that looking through a spherically shaped transparent object like water in a bowl, ice or crystal can visually magnify an object on the other side. However, only with the invention of the first compound light-microscope around sixteen-hundred, we could see for the first time that living beings are build of smaller units we call *cells*. The possibility to actually see cells, observe how they multiply and migrate, opened a whole new field - cell biology. With the advancement of lens shaping and optimised combinations of lenses, researchers pushed the optical resolution towards the *Abbe Limit* which enables us to distinguish two objects as close as ~200 nm if visible light is used.[1, 2] Utilizing fluorescent molecules, super-resolution techniques like Stimulated-Emission-Depletion-Microscopy (STED) and Stochastic-Optical-Reconstruction-Microscopy (STORM) pushed the optical resolution even beyond the diffraction limit [3–5].

By today, a vast variety of tools is available to researchers to investigate cellular processes optically, electrically, and chemically in order to advance our understanding of cells and organisms, the origins of diseases and to ultimately develop new treatments for these diseases. However, the challenge of filling fundamental gaps in cell biology lies in the complexity of how molecular processes driven by diffusion and chemical bonds lead to a composition of living cells and how multiple cells interact to form living organisms. Therefore, gathering information about the interaction between cells and their environment is crucial. Besides electrical and chemical stimuli, this also includes mechanical processes.

For instance, the example of muscle cells shows that cells can actively exert forces, in this case via contraction. Although the beating of a heart or the use of our arm muscles is a collective process involving billions of cells, the desired reaction is only possible because of the contraction of each individual cell. On the other hand, our sense of touch is proof that at least some cells, if not all, have the capability of probing the stiffness of their mechanical environment. Similar to the numerous techniques for the optical investigation of cells, a set of tools to measure displacements, stress, and forces exerted by cells have emerged over the last two decades[6–8]. Indeed, researchers discovered that cells sense their mechanical environment leading to alterations in: cell migration pattern, phenotype, gene expression, growth cone guidance, and stem cell fate [9–18]. Furthermore, the active exertion of forces is fundamental for: locomotion, immune response, morphogenesis, wound healing, tumour metastasis, tissue formation, and extra cellular matrix deposition [19–24].

Whilst the current state-of-the-art force sensing techniques have significantly advanced the field of cell-mechanics, important limitations remain. For example, a major restriction for traction force microscopy (TFM), the currently most widely used method, is that the cells need to be removed after a measurement, in order to obtain a reference image in the relaxed state. Therefore, measuring a same sample of cells over days or weeks is not possible, a feature required to investigate e.g. stem cell differentiation. Furthermore, TFM is based on the use of fluorescent markers which requires either the high light-intensities of fluorescent lamps or lasers, possibly leading to photo-toxic effects restricting frame rate and long-term applicability of the techniques. In addition, most force sensing techniques are only able to measure stress in the plane of the substrate, however, it has been shown that cells can apply similar stresses out-of-plane.

My PhD was part of a group effort to develop a new technique to measure displacements and stress exerted by biological cells to overcome the above stated limitations of other force-sensing techniques. We developed Elastic-Resonator-Interference-Stress-Microscopy (ERISM) with the goal to visualise forces of biological cells live, i.e. as they are exerted on the substrate, and to investigate processes, like stem cell differentiation, over several weeks. As an interferometric technique, ERISM is inherently well suited to detect out-of-plane

displacements with nanometre precision corresponding to forces in the piconewton regime. Similar to conventional light-microscopy ERISM is a wide-field technique which facilitates the observation of many cells at the same time. Without the need to ever detach the cells after the measurement, ERISM can be combined with antibody staining on fixed cells e.g. for proof of stem cell differentiation. ERISM is a cost-efficient and easy to implement technique which we expect to be adapted by other researchers.

This thesis is structured as follows: After this introduction I will give a short overview of the biology of cells and the cytoskeleton which is at the heart of cell mechanics. With a review of existing techniques I will place ERISM in the context of the current state-of-the-art force measurements and highlight why we think that ERISM can significantly contribute to the field of cell mechanics. In the third chapter I will explain the concept of ERISM, elaborate on the computations involved to extract displacements and stress from the raw data and describe important design parameters. In order to demonstrate the value of ERISM, I will use its key features to investigate cells from the central nervous system (CNS) which are potentially challenging to measure due to their weak force generation. I will finish my thesis with concluding remarks on ERISM with respect to existing techniques and its potential through further improvements and applications.

Chapter 2

Background

In this chapter we will look at the basic biology of cells. After explaining the main parts of the cytoskeleton, the mechanisms behind cell adhesion and cell migration will briefly be introduced. The chapter will close with an overview of nowadays commonly used force sensing techniques to motivate where ERISM can contribute to the investigation of cell mechanical problems.

2.1 Basics of Cell Biology and Cell Mechanics

This section is in particular relevant for readers with a background outside biology to establish a common ground for the scientific vocabulary used in the following chapters. If not stated otherwise, information is taken from the book "Essential Cell Biology" by Alberts et al.[2]

2.1.1 Main-Parts of a Cell

The cells found on earth are classified into two groups: *Prokaryotes* and *Eukaryotes*. Prokaryotes are the most abundant form of cells and can be divided into *bacteria* and *archaea*. In contrast to eukaryotes, prokaryotes do not have a nucleus and do not form multicellular organisms. The group of eukaryotes covers single cell organisms like yeasts and amoebae

but also multicellular organisms like fungi, plants, and animals. In this work we will focus only on animal cells.

A schematic of an animal cell can be seen in Fig.2.1a. The whole cell is enclosed by the plasma membrane. Although one of its functions is to separate and protect the inside of the cell from the outside, ions and molecules can pass through the membrane via diffusion or active processes regulated by the cell. The cytoplasm is everything within the cell membrane except for the nucleus, it is composed mainly of water with salts, vitamins, and proteins needed for the cellular processes and contains organelles other than the nucleus. The cell nucleus encloses the DNA (deoxyribonucleic acid) and regulates gene expression. Of major importance for this work is the cytoskeleton which will be covered in more detail in the next section.

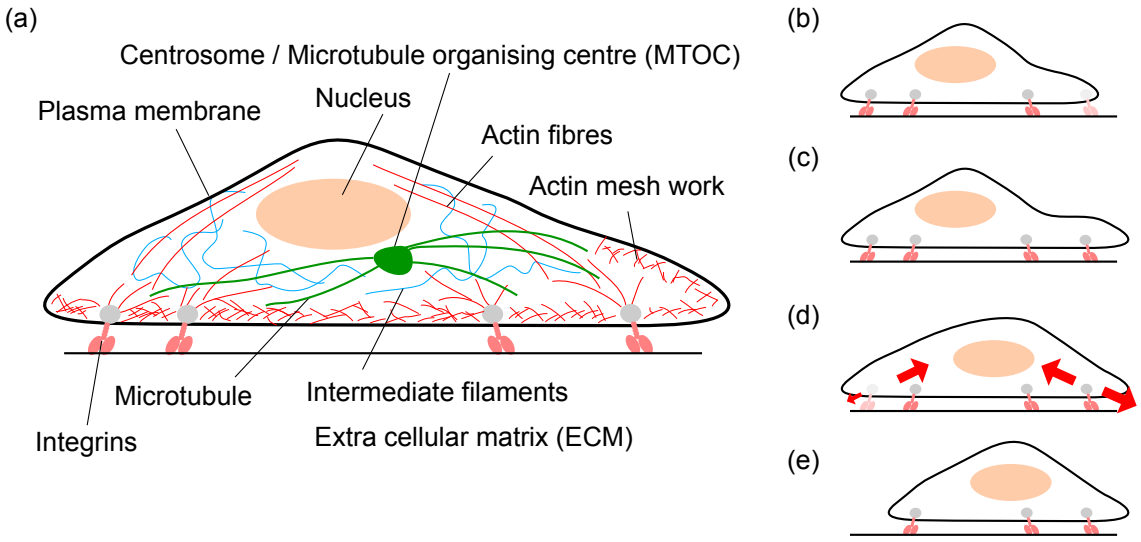

Figure 2.1: (a) Schematic of eukaryotic cell with cytoskeleton. (b)-(e) Mechanism of mesenchymal cell migration. (b) Cell forms lamellipodium and filopodia at leading edge and establishes cell-ECM contacts. (c) Maturation of cell-ECM contacts. (d) Contraction of cell body towards front via actin-myosin contraction. (e) Detachment of cell-ECM contact at the end of the cell.

2.1.2 Cytoskeleton

In contrast to the stiff skeleton of animals, the cytoskeleton in cells is a dynamic construct of proteins, assembling and disassembling to support the functions of the cell. This dynamic

nature allows a fast response to external and internal stimuli which is vital for the function and survival of the cell. Structural support when encountering external stress is one of the main functions of the cytoskeleton. However, it is also crucial for fast directional transport of organelles and chemicals inside the cell. The cytoskeleton is comprised of three main components: *microtubules*, *intermediate filaments*, and *actin filaments*. All three are based on monomers which bind together to more complex polymer structures.[2, 25]

Microtubules are formed by α-tubulin and β-tubulin building strong pillars reaching from the *microtubule organising centre* (MTOC) to the edge of the cell. The polarised polymers allow bidirectional cargo transport inside the cell by molecular motors like dynein and kinesin. Furthermore, microtubules play a major role during cell division (mitosis) by forming the mitotic spindle for segregation of the chromosomes.

Actin forms tightly wound helical filaments (F-actin) which are less rigid than microtubules, however, they can bind to crosslinking proteins to form different types of highly organised, stiff structures (actin meshwork). Actin filaments are build of *globular actin* (*G-actin*). Actin filaments are polarised and polymerisation/depolymerisation occurs at the plus/minus end. Based on the concentration of G-actin and of other proteins in the cytoplasm interacting with actin filaments may be completely depolymerised, growing, or exhibit stable lengths. The continuous polymerisation of actin at the leading edge of the cell is a key player in forming protrusions to probe the environment and to facilitate cell movement[26, 27, 25, 28]. Of significance for this works is the interaction of F-actin with myosin, especially with myosin-II. Muscle contraction of skeletal muscles as well as the contraction inside cells required for cell migration (see below), and neuronal growth cone migration strongly rely on the actin-myosin-II interaction[2, 28, 29].

Intermediate filaments are called “intermediate” because their diameter of around 10 nm is between the diameter of microtubules (25 nm) and actin filaments (7 nm). They are less stiff than microtubule and actin filaments and are not polarised like the other two polymers, hence, they are not suitable for transport via molecular motors. Due to their high flexibility and resistances against tensile forces, intermediate filaments strongly support the integrity of the whole tissue and the cell itself.

2.1.3 Cell Adhesion and Migration

Cell adhesion and cell migration are important processes in the developing human body as well as during its live. The mechanism of forming tight bonds between cells and the ECM or other cells is vital — simply to hold the organism together. More specifically, cell adhesion is crucial during tissue formation and cell migration[30, 26]. In addition, cell adhesion to other cells or the ECM provides one of the pathways for cell migration. The ability to actively change location allows cells to be produced in one place but to fulfil their function in another. It allows them to actively track down pathogens, like bacteria, in order destroy them by phagocytosis. Only the controlled adhesion of specialised cell types enables the formation of tissue and organs.

There exists a huge variety of proteins involved in establishing cell-cell or cell-ECM contact. This variety enables the cells to attach selectively, e.g. to specific ECM proteins which for instance could mediate when a cell does attach or not. Proteins involved in cell-cell junctions are usually of the family of *cadherins* and cell-ECM contacts involve often proteins of the *integrin* family. For this work we are more interested in the integrins as we will mainly talk about single cell adhesion and migration. Fundamental for cell adhesion are *focal adhesions* (FA), large macromolecular assemblies which bind to the ECM. Besides anchoring the cell to the ECM, they also serve as signalling interface between the ECM and the cell. The FA are comprised of integrins which reach through the plasma membrane and bind to the ECM — which can consist of fibronectins, collagens, laminins — via multiprotein complexes including *talin* or *vinculin* to the actin filaments[26, 31–33]. However, there are more than 100 different proteins involved in FA formation, indicating a high functional diversity[34–36].

Cells have developed different ways of migration. Here, we are interested in the pathways based on the interaction between cells and ECM. This means we exclude for instance microswimmers like sperm cells. Furthermore, we will focus on the so called *mesenchymal cell migration* pattern, based on FA-ECM interaction, found in many adherent cells, e.g. fibroblasts or mesenchymal cells. Another mode of cell migration is via the formation of

blebs. Recent publications show that cells can switch between different modes of migration depending on the environment[37–39].

The current model for a mesenchymal cell migration pattern involves the following steps (cf. Fig.2.1b-e). If a cell senses external stimuli, like chemical cues or a change in the physical environment, this can lead to a formation of protrusions like lamellipodia. This is driven by actin monomers assembling at the leading edge of the cell and polymerising into actin filaments and networks. The second step involves the formation of a new focal adhesion to anchor the cell at the front. The whole cell is then pulled forwards by actin myosin interactions similar to the contraction happening in muscle cells. At the back of the cell the actin network and the focal adhesion is depolymerised to allow further movement. It is evident that in the whole process forces are applied to the substrate. Measuring these forces can therefore contribute to a comprehensive understanding of this process. [40, 41, 26, 42]

2.2 State-of-the-Art Methods to Measure Cellular Forces

An easy-to-realise macroscopic force measurement could be to use a spring with a known spring constant k and fix it on one side (cf. Fig.2.2a). On the free side the force would be applied along the axis of the spring, and by measuring the displacement x of the end of the spring one can calculate the applied force via $F = -kx$. Many techniques for the measurement of cellular forces are based on the very same principle: tracking displacements of a material with known mechanical properties. Following the analogy of a spring, the Young's modulus E describes how the strain ε that an elastic material experiences is related to the applied stress σ:

$$\sigma(\varepsilon) = \varepsilon E(\varepsilon) \tag{2.1}$$

A material with a Young's modulus independent of the strain — i.e. a material that does not become stiffer or softer when deformed — is referred to as a *linear elastic material*. If in addition the Young's modulus is the same along all three axis, then the material is a linear *isotropic* elastic material. The term *elastic* highlights that once the exerted stress is released from the deformed object it will relax into its initial shape. Linear isotropic elastic materials

are ideal for the application of force measurements since the material will not change its properties while it is deformed and force calculations from displacements are much more straight forward than compared to *anisotropic* elastic or *viscoelastic* materials. However, the ECM (in vivo) is not always necessarily a linear isotropic elastic material, therefore, the substrates used in force measurements are often a trade-off between being able to perform accurate force measurements and providing a physiological environment.

In the following sections, the two most commonly used techniques to measure forces exerted by cells — Traction Force Microscopy (TFM) and using Micro-Pillar-Arrays — are introduced. Furthermore, for higher spatial and force resolution one can utilise the optical response induced by the conformational change of molecules under stress.

It should be noted that the three approaches discussed below are tailored to sense forces actively exerted by cells. However, for a comprehensive understanding of cell mechanics, the mechanical properties (e.g. Young's modulus) of the cells themselves have to be known as well. Amongst others, techniques designed for this purpose are: Micro-Pipette-Aspiration[43], Optical-Traps and Optical-Tweezers[44, 45], Magnetic-Twisting-Cytometry[46], Brillouin Spectroscopy[47], Atomic-Force-Microscopy[48]. Atomic-Force-Microscopy will be introduced later in Section 3.5.1 as a tool to characterise the elastic micro-cavities used in ERISM measurements.

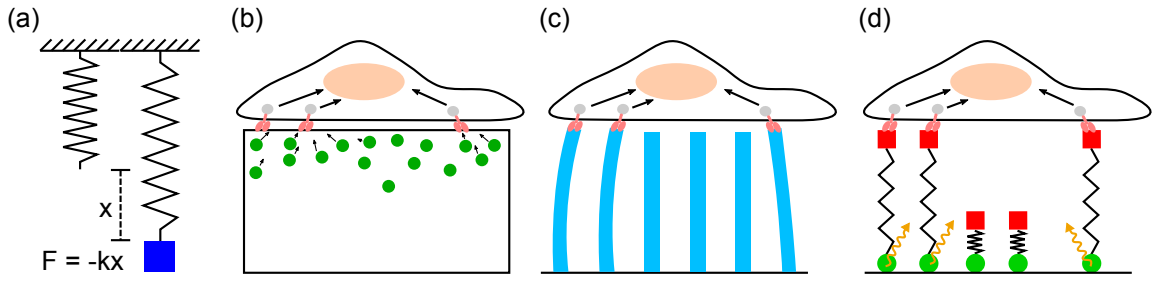

Figure 2.2: Simplified schematic illustration of a selection of force sensing techniques. (a) Macroscopic force sensor based on a spring. (b) TFM. (c) Micro-Pillar-Array. (d) Force sensor based on small molecules with quencher (red rectangle) and fluorophore (green circles)

2.2.1 Traction-Force-Microscopy (TFM)

Harris et al. already observed in 1980 that thin polydimethylsiloxane (PDMS) layers show wrinkling patterns whilst under stress exerted by cells[49]. Since wrinkling is a highly non-linear process the actual stress exerted by the cells was difficult to estimate which raised the need for a technique which could observe substrate deformation in the linear regime.

TFM has been introduced by Dembo and Wang in 1999 to measure traction forces of cells based on tracking the displacement of fluorescent beads inside an elastic material[50]. In its simplest form, a TFM experiment would be designed as follows (cf. Fig.2.2b)[51]. First, fluorescent beads with a diameter of typically 0.04–0.2 µm are mixed into a two component polyacrylamide (PAA) gel or PDMS[52]. The Young's modulus of the cross-linked gel can be adjusted in a range of 0.1–1000 kPa by changing the mixing ratio of the two components. Before seeding the cells a surface coating is applied to allow cell attachment on the PAA. Then the position of the fluorescent beads is measured with an inverted microscope in combination with a fluorescence lamp, similar to standard fluorescence imaging of cells. In order to determine by how much the beads are displaced from the relaxed state, the cells have to be detached or their ability to exert stress inhibited and the bead positions of the relaxed state is measured. With a cross-correlation algorithm, the displacements of the spatially randomly distributed beads can be calculated from these data sets. The stress at each point of the image is calculated by solving the inverse problem with the displacement map as input. The last step is one of the big challenges in TFM as this is an ill-posed problem which requires regularisation of the input data[53–55, 7].

To gain more insight into the force generation of cells, two main points had to be considered to extend standard TFM. First, with standard TFM only the force component lateral to the substrate can be measured, therefore, measuring forces in vertical direction requires to track the bead displacement in all three dimensions. Second, the spatial- and force resolution are linked since more accurate measurements in bead displacement lead to higher force resolution.

Out-of-plane stresses can be measured by using a confocal microscope to track the bead positions not only in lateral but also in vertical direction[56]. This approach is sometimes

referenced in the literature as 2.5D-TFM as the cells are still on a 2D substrate but the stress is measured in three dimensions[57–60]. In organisms, cells are surrounded in all three dimensions by other cells or by the ECM and cell experiments in 3D matrices as opposed to flat substrates have become more and more common due to their higher physiological relevance[61]. Leagant et al. have shown that bead displacements can be tracked in real 3D substrates to investigate the stress exerted by cells. Although 3D-TFM would therefore be for many cell types the method of choice, the experimental and computational challenges of this technique allowed so far only single cell experiments and the method has not been adapted by other groups so far[62].

For higher *spatial resolution*[1] the bead density has to be increased to achieve a finer sampling of the deformations. This is achieved by: using smaller beads, increasing the amount of beads, and using beads with different colours to allow higher bead density whilst still being able to distinguish two beads which are very close to each other. Use of a confocal microscope is crucial to determine the bead positions as accurately as possible. Recently, Colin-York et al. showed that STED and TFM can be combined to improve the spatial- and *stress resolution* even further[63].

For standard 2D-TFM with a fluorescence lamp the *time resolution* is determined by the exposure time required to measure the bead position. However, when using a confocal microscope, the time resolution suffers from increasing image size.

With all these different possibilities to improve TFM, researchers investigated a huge variety of cell mechanical questions. High resolution TFM was used by Plotnikov et al. who found that force fluctuations within focal adhesions mediate sensing the ECM rigidity and directs cell migration[64]. Taking the force balance between cells into account and/or using a finite element method (FEM) approach, it is possible to investigate the forces in *connected cells* which is for instance highly relevant to wound healing by epithelial cells[65, 23, 66]. The migration of neuronal growth cones requires high force and temporal resolution and was investigated by different groups with TFM[16, 67–69]. This will be discussed in more detail in Chapter 4.4 as it is of particular relevance to this thesis.

[1] Minimum distance for which two point forces can still be distinguished.

Even though TFM has been used to investigate many different cell mechanical questions, its application also revealed the following limitations. 2.5D-TFM showed that even on 2D substrates vertical stress is exerted by cells. Although, investigating the forces applied normal to the surface with TFM is thus possible, it comes at the cost of more complex data analysis and the increased exposure of the cells to light which may lead to photo-toxic effects. In fact, even with 2D-TFM Polackwich et al. observed neurite retraction induced by light exposure when fluorescence images were taken every 2 s over 30 min[68]. In addition, since TFM requires taking images without cell traction, this technique is not suitable for observing cells on the same substrate over several days or weeks as for instance required to investigate the forces involved in stem cell differentiation. Theoretically it would be possible to take this zero-force-image before the cells attach on the substrate, however, this would add on more day to the experiment in which the cells have to be in an incubator on the measurement setup. Moreover, in experiments it is often required to select cells of interest, for instance, in one field of view may be too many cells in contact with each other but often single cells are required for correct force measurements. Hence, in order to observe enough cells which can be investigated, a large area has to be covered, i.e. many fields-of-view, limiting the time-resolution of the technique. It should also be noted that only after the data analysis is completed the researcher will know where and how strong the cells deformed the substrate.

2.2.2 Micro-Pillar-Arrays

Tan et al. introduced another technique to measure lateral cell forces based on tracking displacements of individual micro-pillars of a micro-pillar-array (cf. Fig.2.2c)[70]. PDMS is structured such that pillars with a controlled diameter and height serve as a substrate for cells. The displacement of the top-end of the pillars can either be measured with common light-microscopy or by tracking fluorescent tags. The displacement is proportional to the force exerted by the cells. In addition, there is no coupling between the pillars, and the position of the pillars is — at least roughly — known due to the grid-like structure. Therefore, forces can be calculated with significantly less computational effort compared to TFM.

Du Roure and Saez et al. proved that this technique is suitable for measuring forces exerted by multicellular assemblies by performing measurements on epithelial cell sheets [71, 72]. The technique is well suited to investigate cell-cell contacts as the force balance between the cells can be easily calculated because of the independent bending of the posts. However, this also implies that cell-cell signalling might be disturbed as forces can not be transduced through the substrate. Another inherent drawback of this technique is that an array of micro-pillars is a non-physiological environment especially since surface coatings will only be present at the micro-pillars' surfaces. Experiments investigating the influence of different substrates stiffnesses on cell behaviour may suffer especially from this as for each substrate stiffness the geometry of the posts would change. Based on the geometry of this technique, the measurement of forces applied vertical to the substrate plane is not possible. Finally, monitoring the cell morphology by standard bright-field or phase-contrast imaging is more difficult as the light path is disturbed by the micro-pillar-array[73, 7].

2.2.3 Single Protein Tension Probes

Whilst the two methods described above are utilising the deformations of a substrate in order to determine cell traction forces, Grashoff et al. followed a very different approach to measure the stress, single proteins encounter inside the focal adhesions of living cells [74]. The authors modified the protein vinculin such that two fluorophores coupled via a flagelliform linker sequence were inserted into the vinculin protein. Depending on the stress applied to the protein the distance of the two fluorophores varies and hence, the efficiency of fluorescent resonance energy transfer (FRET) between these two fluorophores decreases with increasing stress, i.e. increasing distance of the fluorophores. Using this technique the authors found that in stable focal adhesions the average tension one protein molecule encounters is approx. 2.5 pN whereas higher (lower) tension is associated with adhesion assembly (disassembly).

Instead of using molecular sensors which bind to proteins inside the cell, Berkley et al. and Wang et al. proposed DNA based molecular sensors which can be applied to a broad range of surfaces [75, 76]. Here a fluorescent dye and a quencher are linked to a DNA

sequence. The force required to separate dye and quencher can be tuned by varying the DNA sequence length.

With a force resolution in the lower piconewton regime these techniques offer the highest sensitivity amongst the techniques discussed here. The main drawbacks are that the direction of the forces can not be extracted and that although multiple probes could be tagged to one adhesion complex, it remains unclear how many non fluorescent proteins contribute to the total mechanical stress.

Chapter 3

Methods

After we discussed in the previous chapter the need to measure cellular forces but also identified the limitations of the currently existing techniques, this chapter will introduce in detail *Elastic-Resonator-Interference-Stress-Microscopy* (ERISM) as a novel tool to measure cellular forces. As we can conclude from Chapter 2, it would be beneficial to add the following features to the capabilities of the currently available group of force-sensing techniques: 1) Accurately measure forces vertical to the substrate. 2) Decrease photo-toxicity to enable long-term measurements without risking apoptosis during the measurement. 3) Increase throughput of cells to improve the statistical significance of the result. 4) Remove the need for zero-force images to investigate cells over days and to allow antibody staining. 5) Enable the researcher to see where forces are exerted during the measurement.

In the following sections we will discuss how ERISM works and addresses each of the points mentioned above. The chapter will start with an overview of the concept of ERISM, highlighting its strengths compared to other techniques. Then, we will look in detail at each step involved in measuring the forces which cells exert on a substrate. This includes an in-depth description of the optical setup and the software we developed to perform the measurements and calculations, as well as a discussion of the design parameters involved in each step.

3.1 How ERISM Works

The general concept of ERISM is summarised in Fig. 3.1. The core of ERISM is an in-house fabricated elastic optical micro-cavity that consists of two semi-transparent gold mirrors sandwiching an elastic material (elastomer) in between them (cf. Fig. 3.1 (a) and (b)). The top mirror can be functionalised with a bio-coating (e.g. fibronectin) before seeding cells on the micro-cavity.

Our optical setup is based on a commercially available inverted fluorescence microscope which allows standard phase-contrast and fluorescence imaging. In addition, by illuminating and imaging the micro-cavity with a microscope objective from underneath using monochromatic light, an interference fringe pattern is formed (cf. Fig. 3.1 (c) and (d)). Dark areas represent positions where a light-wave reflected at the first gold layer and a light-wave reflected at the second gold layer have a phase shift of 180° with respect to each other. This destructive interference occurs if the wavelength of the incident light is:

$$\lambda = \frac{4Ln(\lambda)}{2m+1} \tag{3.1}$$

In Eq. 3.1 L is the local thickness of the micro-cavity, $n(\lambda)$ is the wavelength dependent refractive index of the elastic spacing material and m is the order of interference ($m = 0, 1, \ldots, N$). Figure 3.2 shows a schematic visualising the phase difference between a wave reflected at the bottom mirror and reflected at the top mirror for different L and how this phase difference is linked to the observation of dark areas (destructive interference) and bright areas (constructive interference). A perfectly flat micro-cavity (with homogeneous thickness) will show the same reflectance at every point. However, if a localised vertical force is applied to the surface of the micro-cavity, the cavity thickness L at this position and hence the resonance wavelength will change. As the whole field of view is illuminated at once, any changes in cavity thickness, and thus, any forces cells apply to the surface of the micro-cavity, across the field of view are directly apparent from the reflectance image recorded at one wavelength of illumination (cf. Fig 3.1d).

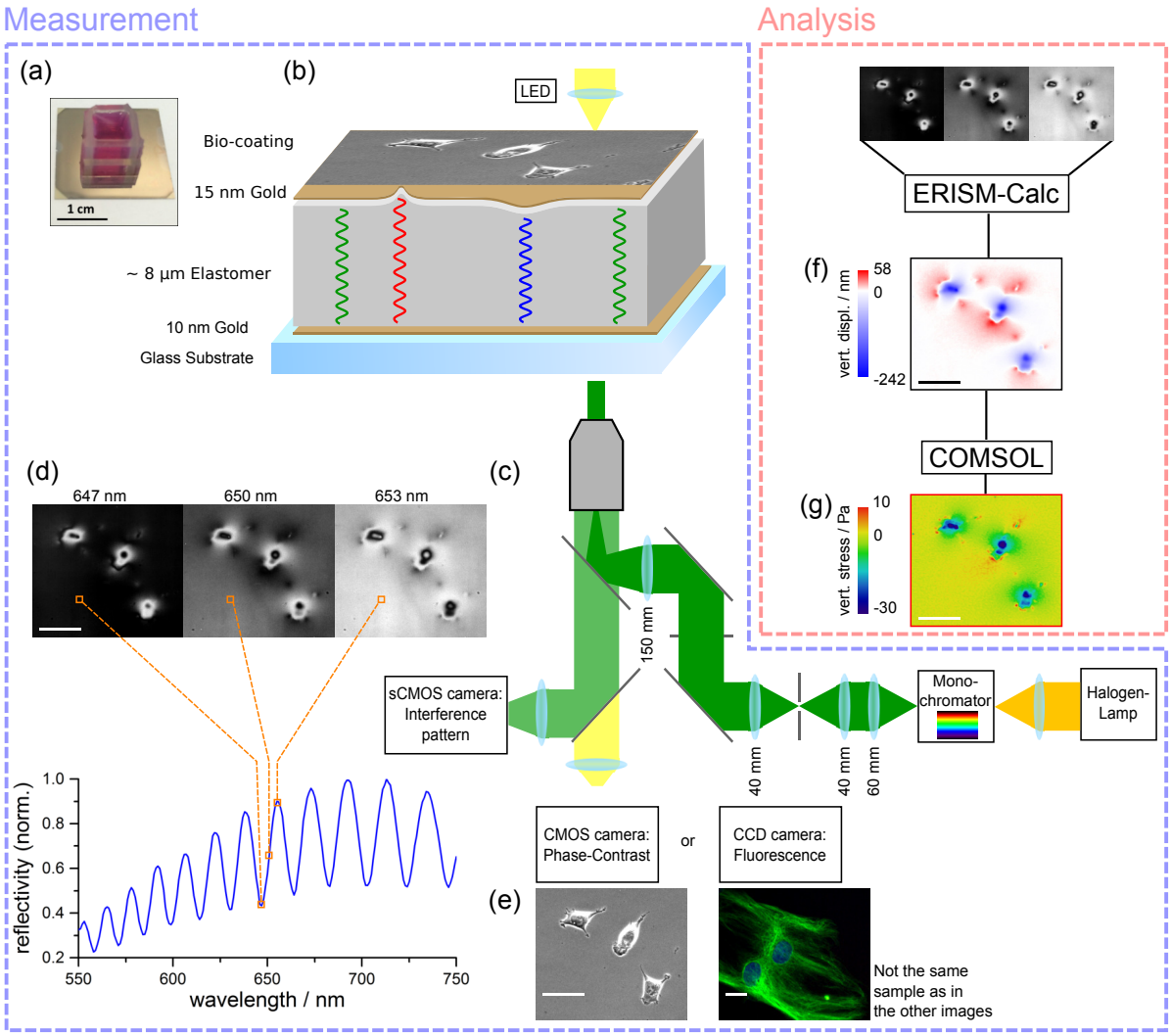

Figure 3.1: Overview of ERISM. The blue and red boxes indicate which processes are done online at the setup and which steps are done after the measurement. (a) Micro-cavity with silicone chamber filled with cell medium and cells. (b) Schematic of the layer structure of the micro-cavity. (c) Optical beam path of the fluorescence microscope with added monochromatic light source. (d) Representative images acquired for different wavelengths (top) and corresponding reflectivity for one pixel in the range of 550–750 nm (bottom). (e) Phase-contrast and fluorescence image. (f) Displacement image calculated from the acquired experimental data with the software *ERISM-Calc* that was developed in-house. (g) Vertical stress exerted by the cells. Calculated with *COMSOL* from the displacement image.

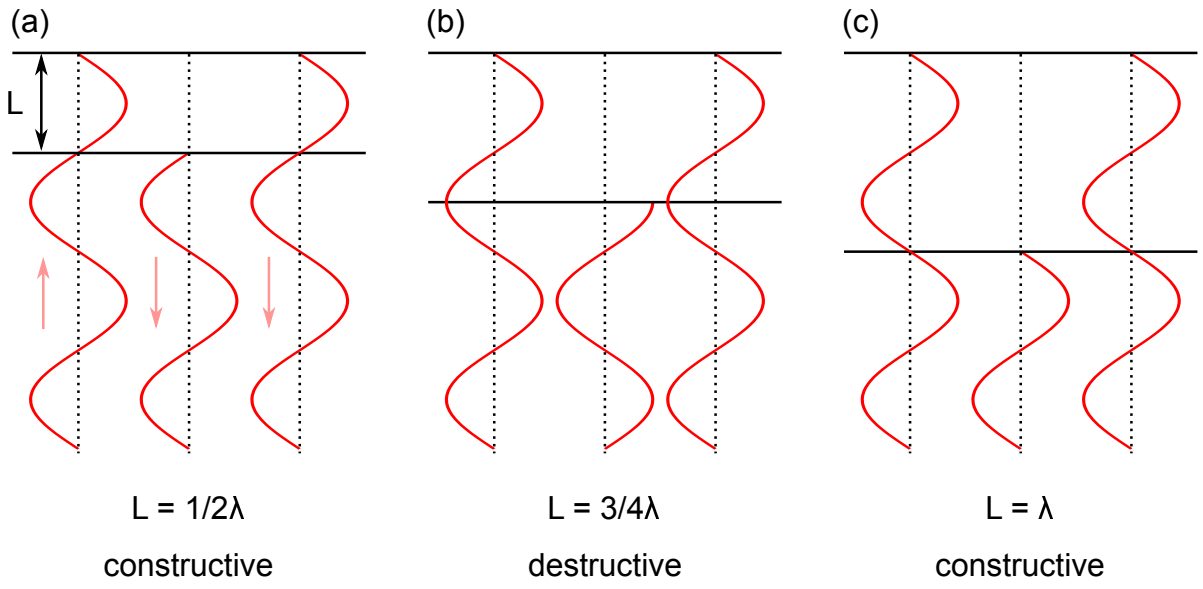

Figure 3.2: Schematic visualising how the phase shift between a wave reflected at the bottom mirror and reflected at the top mirror of a planar micro-cavity depends on the cavity thickness L according to Eq. 3.1. In (a), (b), and (c) the first wave is propagating upwards, the second wave downwards after being reflected at the bottom mirror, and the third wave propagating downwards after being reflected at the top mirror. In this schematic the refractive index of the resonator is equal to the refractive index surrounding the micro-cavity.

To accurately determine the local cavity thickness, we record images of the reflectance (cf. Fig. 3.1d) of the cavity over a wavelength range (typically 550–750 nm with 1 nm step size) that is large enough to capture multiple resonance wavelengths. By recording one such stack of images, reflectance spectra (cf. Fig. 3.1d bottom, for an example for one pixel) are acquired for each point within the field of view. The minima in these spectra, which represent the resonance wavelengths of the micro-cavity, can then be used to calculate the thickness for every pixel in the image with the program *ERISM-Calc* which was developed during the course of this PhD (cf. Section 3.4).

Because of the very planar surfaces of the micro-cavities, we can subtract a background plane from the map of absolute thickness values to obtain the vertical displacements with nanometre precision, without the need to ever detach the cells (cf. Fig. 3.1f). This, in combination with the low-power light source, allows us to investigate cells on the same substrate over weeks, by either measuring continuously on the ERISM setup, which is equipped with an on-stage incubator, or by moving the sample between cell culture incubator and ERISM setup. Moreover, we can fix cells after an ERISM measurement on the micro-cavity to apply antibody staining (cf. Section 4.3.2), e.g. to check for cell type specific markers or to visualise focal adhesions.

In many cases, knowing the displacements is already sufficient to determine, e.g. where the cells apply the strongest forces or if the applied forces differ for different cell populations. However, with a finite-element-method (FEM) we can calculate the stress exerted by the cells from the displacement map (cf. Fig. 3.1 (f) and (g) and Section 3.5.3).

The micro-cavity with cells is placed on a motorised stage to allow measurements at multiple positions on the same substrate. In addition, the whole setup is fully automated and controlled via the self-written *LabVIEW* program *ERISM-Read*. Therefore, we can investigate multiple cells, at multiple positions and over a long time, which is why ERISM can provide results with very good statistics.

3.2 Micro-Cavity Fabrication

In this section I will describe how the micro-cavities which we use as substrates are produced. The fabrication and the development of the fabrication process has been carried out by Dr. Nils M. Kronenberg[77] but is provided here to allow the reader to get a comprehensive picture of ERISM.

The micro-cavity is processed on a 500–600 µm thin cleaned glass substrate, sized 24 mm x 24 mm. Except for the elastomer and the bio-coating, all layers are deposited via evaporation in vacuum (thermal or electron-beam). First, a 0.5 nm thin chromium layer is evaporated onto the glass to allow better adhesion for the 10 nm thin gold layer evaporated in the next step. To prevent wrinkling of the elastomer layer spin-coated later, a 50 nm thin SiO_2 layer is evaporated. The two component elastomer is thoroughly mixed in a 1:1 volume ratio and degassed under vacuum for 1 min. The thickness of the elastomer is controlled by adjusting the spin-coating speed. Here, the elastomer is spin coated for 1 min at 3000 rpm which yields an approximately 8 µm thick elastomer layer. After the spin-coating, the sample is heated for one hour at 110 °C to allow cross-linking between the two components. As before, to avoid wrinkling of the elastomer, the surface energy has to be increased. This is done by a mild oxygen plasma treatment (power, 15 W; duration, 30 s) which results in another thin SiO_2 layer on top of the elastomer. As a top mirror, 15 nm of gold are evaporated on top of the structure. The entire fabrication process is done in a clean-room environment to avoid contamination with particles.

3.3 Read-Out-System

3.3.1 Optical Setup

A detailed list of the main parts used for the optical setup is listed in the Appendix A.

In addition to the optical implementation of the force sensing technique, cell mechanical investigations require phase-contrast imaging to track morphological changes and fluorescence imaging, e.g. to visualise actin filaments. We therefore chose a commercially available

inverted fluorescence microscope as the core module for ERISM. The monochromatic light is created via a halogen lamp coupled to a monochromator (cf. Fig. 3.1c, right). The spectral width of this light can be controlled by changing the widths of the entrance and exit slits of the monochromator. We will discuss the influence of the slit width on the ERISM signal in Section 3.4.5.

The monochromatic light is coupled in epi-illumination configuration via custom-built Köhler-like illumination optics into the beam path of the microscope to minimise uneven illumination caused by the lamp filament or dirt on the lenses[1]. The light is then focussed on the back-focal-plane of the objective to expose the micro-cavity to collimated light. This is necessary to achieve a high contrast between constructive and destructive interference. The light reflected at the sample is collected with the same objective and follows the same beam path in the microscope as light from standard dia-illumination/phase-contrast illumination. We replaced the built-in halogen lamp of the microscope (for phase-contrast imaging) with an LED (cf. Fig. 3.1b, top) to allow fast on and off switching. This improves overall time resolution whilst minimising light exposure to the cells during long-term measurements.

The focal planes of the phase-contrast imaging and the ERISM signal are not identical. More precisely, the focus for phase-contrast imaging is on top of the micro-cavity where the cells are, and the focus for the ERISM signal is at the bottom of the micro-cavity where light reflected at the top- and bottom-mirror interferes. Instead of switching between these two focal planes by moving the objective, we use two cameras to collect ERISM signal and dia-illumination signal simultaneously (cf. Fig. 3.1c, bottom left). For this purpose one of the cameras is mounted on a translation stage to allow adjustment of the focus for the ERISM signal.

Inside the microscope a beam splitter directs 80% of the light from the sample to a cooled sCMOS low noise camera and 20% of the light goes to a less sensitive but more cost-efficient CMOS camera. Both, dia-illumination and ERISM signal are collected by both cameras, however, they can be separated by switching the dia-illumination on only when a

[1] Done by Dr. Nils M. Kronenberg.

phase-contrast image is taken[2]. Additionally, it is possible to view both signals at the same time on the two different cameras. This is achieved by using a set of filters to separate the spectral range for the ERISM signal from the dia-illumination signal.

We use a motorised stage to control the x-y-position of the sample. This is especially useful for long-term measurements as different positions on the sample can be investigated repeatedly over time. We can also cover big areas at high magnification and thus avoid that migrating cells leave the field-of-view. In addition, we attached a motor to the manual z-position controller to compensate for sample tilt when covering a larger sample area or to correct z-drift during long-term measurements (see Section 3.3.2). ERISM micro-cavities with cells can be placed in an on-stage incubator (*Okolab*) to maintain a physiological environment for the cells (e.g. 37 °C and 5% CO_2). The temperature of the sample is stable within ±0.1 °C as it is controlled via a feedback loop with a reference temperature sensor inside a water reservoir 2 cm next to the sample.

Fluorescence imaging is done in epi-illumination configuration as well. As of now, we did not implement a motorised switching mechanism of the filter cubes as required for long-term measurements including fluorescence imaging. However, this is commercially available and could be implemented in the future.

3.3.2 "*ERISM-Read*" - Program to Acquire Spatially Resolved Reflectance Spectra

An essential part of this PhD was to develop a fully automated way of recording ERISM for high throughput long-term measurements. This involved design of suitable optical and mechanical components and implementation of an extensive *LabVIEW* program (*ERISM-Read*, cf. Fig. 3.3). In this section, we will first discuss the core features of *ERISM-Read* which allow multiple ERISM measurements over time. Then we will discuss the requirement for an auto-focus system and an x-y-translation stage to allow multipoint measurements over time. Finally, we will discuss the current temporal resolution of ERISM.

[2]The monochromatic illumination does not need to be switched off as the LED provides significantly higher light intensity, outweighing the ERISM signal.

Core Features

ERISM-Read controls: both cameras, LED (on/off), x-y-stage and z-drive, wavelength of monochromator. The program is designed such that for the sCMOS camera parameters like exposure time, binning, and image size can be controlled and a live view of the ERISM signal can be seen. At all times, the standard CMOS camera will show a live phase-contrast image for a selected exposure time. The LED can be switched on and off in the program and the brightness can be adjusted manually with a controller. The wavelength of the monochromator can be changed in the program and is also displayed while the program is changing it during a scan. It is useful to change the wavelength such that at areas without cells the image is dark. If this is the case, even displacements of a few nanometres can be seen as brighter spots in the interference image. The stage position can be set by changing the stage position values in *ERISM-Read* but can also be manually controlled with a joystick. The joystick is inactive during a running measurement to avoid any accidental changes of the sample position.

ERISM-Read can be used for different kinds of measurements. First, one can simply see the live image of the ERISM signal and the phase-contrast image. This is convenient to get a first impression about the forces which cells apply to a micro-cavity. This mode is also used to find the positions on the micro-cavity which shall be investigated.

Second, one can set a wavelength range over which a scan should be done. A scan over a wavelength range, e.g. 550–750 nm in 1 nm steps, is performed as follows: 1) The monochromator moves to the first wavelength (550 nm). 2) The sCMOS camera takes an image at this wavelength. 3) The monochromator moves to the next wavelength (551 nm). This is repeated until the last wavelength (750 nm) is reached. Then, 4) The LED is switched on and a phase-contrast image is taken with the CMOS to track cell movement. Note, the LED is only switched on to take the phase-contrast image but is switched off during a scan. This is especially important if many successive scans are taken to avoid photo-toxic effects on the cells. It is possible to automatically save the images of each scan to the hard disk. One such scan is equivalent to measure the displacement of the current field-of-view for one time point.

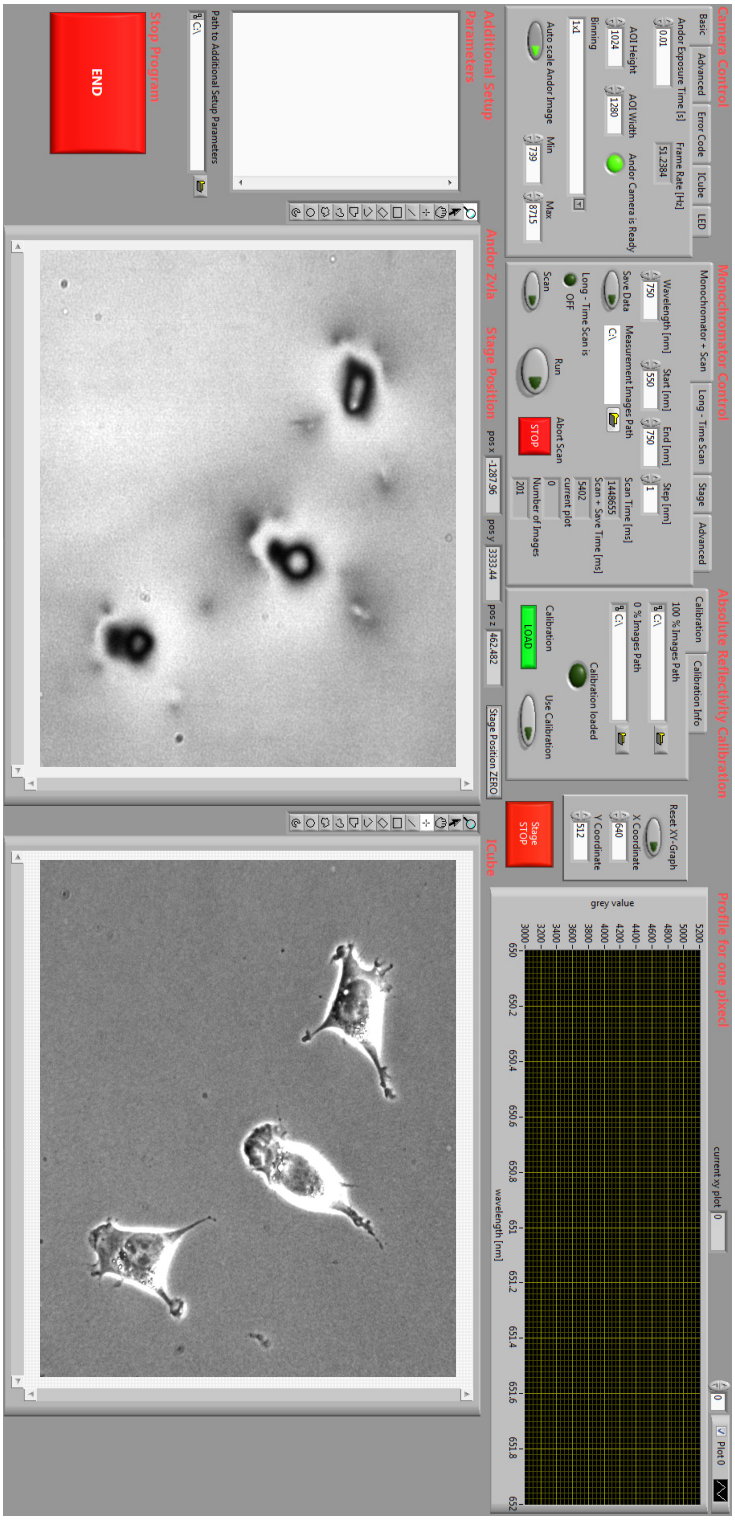

Figure 3.3: Image of the graphical user interface of *ERISM-Read*.

As a third option one can choose to perform a long-term measurement. Wavelength range, pause time between each measurement, and different stage positions can be chosen. It is therefore possible to measure for instance at ten different positions every five minutes, i.e. one complete ERISM measurement will be taken every 5 minutes for each of the ten positions. If selected, a bright-field image will also be taken after each scan to correlate ERISM displacements with observed movement of the cells in the bright-field image. Furthermore, when a long-term measurement is performed, the program collects in a separate folder both a bright-field image and an image of the cavity reflection at a wavelength in the middle of a chosen range. This allows to see thickness changes already during the measurement without any further data analysis.

In addition, *ERISM-Read* can also be utilised to take only bright-field images at different positions over a set time period with a given frame rate.

Auto-Focus

Drift in lateral and vertical direction is mainly caused by the slow thermal expansion of the different components in the microscope. Drift in lateral direction is usually easy to correct after the measurement by using image stabilising algorithms based on particle tracking. However, z-drift moves the specimen out of focus which leads to blurry images which are of little use in the data analysis. To circumvent this problem one can either try to prevent thermal fluctuations, e.g. by placing the whole setup in a thermally controlled environment, or one can implement a mechanism to correct for the z-drift. Especially in a lab with many users, controlling the temperature is difficult due to opening of doors and ventilation and enclosing the whole setup would restrict accessibility. We therefore implemented into the *ERISM-Read* software a standard auto-focus routine based on edge detection to determine if the sample is in focus in combination with the z-drive to adjust the focus position if needed.

This routine works as follows: The user defines a z-range (e.g. $\pm 10\,\mu m$) and an increment (e.g. $1\,\mu m$) by which the z-position will be changed with respect to the current position. The program will then take a phase-contrast image at each z-position. If the phase-contrast image is in focus, the edges and the organelles inside the cells should appear dark (cf.

Fig 3.4a). Therefore, all images are filtered with a *Sobel* filter[3], which basically detects edges. Regions with high contrast have high values in the filtered images. In the next step, the standard deviation of the histogram for each filtered image is calculated. The filtered image with the highest standard deviation correlates with the image which is best focused(cf. Fig. 3.4c). This is because the histogram will become broader with the increasing number of bright pixels for images in-focus (cf. Fig. 3.4b). Finally, the program changes the z-position to the z-value corresponding to the image in focus. The user can chose in *ERISM-Read* the time interval of the auto-focus (e.g. every minute or every hour) during the long-term measurement.

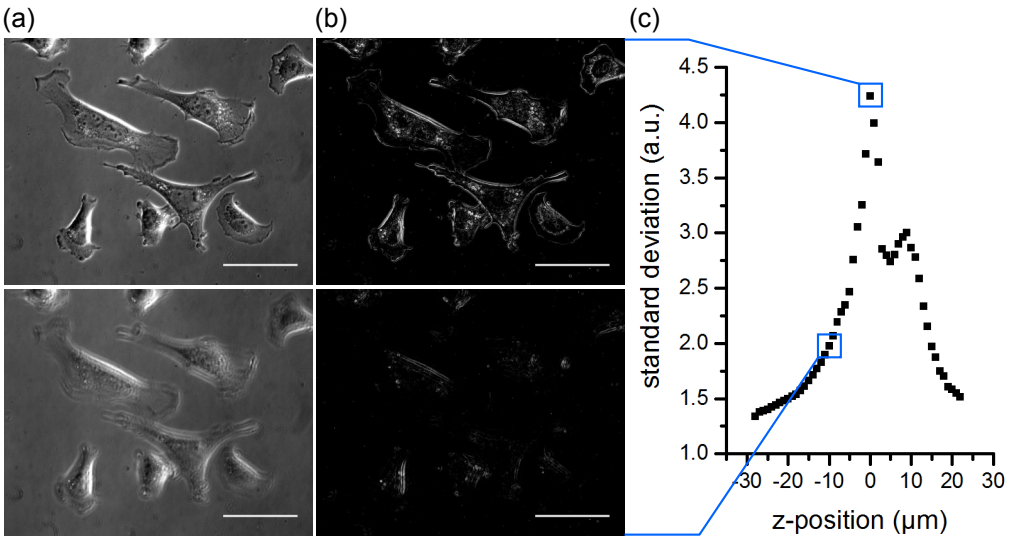

Figure 3.4: Summary of the auto-focus routine. (a) Phase-contrast images. Upper image in focus as controlled by auto-focus routine, lower image 10 µm closer to the objective out-of-focus. (b) Images from (a) after filtering with Sobel-Filter. Contrast is enhanced by the same amount for both images for better visibility. (c) Standard deviation of the histograms for each filtered image. All scale bars are 50 µm.

It is noteworthy that cells are not completely flat. Therefore, depending on the depth of focus of the objective it is not possible to have the whole cell in focus. However, our routine works particularly well for focussing on to the edges and processes of cells (like growth-cones of neurons), and this is what is required to correlate stress images with phase-contrast images.

[3]Other edge detection filter-kernels give similar results, however, the Sobel filter yields the best contrast between images in-focus and out-of-focus.

Multi-Point Analysis

Cell biological experiments often require collecting datasets of multiple cells to obtain conclusive results supported by statistics. Each cell is different and testing a hypothesis should be done on cell populations as opposed to single cells. ERISM is especially suitable to investigate many cells over days or weeks because it is not required to detach the cells. To exploit the full potential of ERISM we use the x-y-z-position capability of the setup to collect data at different positions of the sample.

In *ERISM-Read* the user can first search for the positions where measurements should be done and add each of these positions to an array. The array is therefore already extremely useful during the choice of the target cells, as it is straight forward to find the cells of interest again. The array can be edited by hand to add, correct, and delete positions. During a long-term measurement the program will move to each position stored in the array to take a scan. If the auto-focus function is enabled the z-drift will be determined for the first position and then the z-position will be corrected accordingly for all positions. The array with the positions can be saved as a text file. If the sample position is marked in the on-stage incubator, the sample can be removed from the setup and when reinserted later it is possible to find the positions again. When placed back on the setup, the sample might not be at the exact same position, however, this can be corrected at one position and the whole array transformed accordingly.

3.3.3 Temporal-Resolution of ERISM

The temporal resolution of any imaging technique is a crucial part which determines how well dynamic processes can be investigated. If a cell moves from one position to another but images are only taken at the start and end, nothing will be known about what happened during the migration. In the same way, if the substrate is dynamically deformed by cells, a characterisation of the process dynamics is only possibly if the time increment is small enough.

We take images in the range of 550–750 nm with a step size of 1 nm to calculate later on the thickness at each image pixel. In addition, we take a phase-contrast image after the 201 images at different wavelengths have been taken. If this is done continuously to track thickness changes as fast as possible, the sets of images are acquired with a temporal resolution of (8.0 ± 0.5) s. The temporal resolution is limited by the time the monochromator needs to move to the different wavelengths, by the exposure time set for the cameras, and by the software itself. To achieve (8.0 ± 0.5) s temporal resolution we use an exposure time of 10 ms for the sCMOS camera and 64 ms for the CMOS camera[4]. This means that a total of 2 seconds ($201 * 0.01\,\text{s} + 0.064\,\text{s} = 2.01\,\text{s}$) is spent on taking images. The monochromator needs 4 seconds to move in one direction from 550–750 nm in 1 nm steps, 1.5 seconds to come back in one go to 550 nm, and 0.5 seconds are spent in the software, e.g. to allocate image buffers.

Although 8 seconds is fast enough for many cellular processes, we can decrease this to 2 seconds by using a smaller wavelength range (650–690 nm). As mentioned above, a range of 201 nm is needed to acquire multiple interference minima to determine the *absolute* thickness of the micro-cavity. However, dynamic thickness *changes* can be followed by tracking the position of one single minimum, which allows us to decrease the measurement range. We will discuss this in more detail in Section 3.4.5 when we look at the calculation of the cavity thickness. For a typical long-term measurement with 2 seconds temporal resolution, we first take one wavelength scan over 550–750 nm (8 seconds) and the successive scans are taken with a range of 650–690 nm (2 seconds)[5].

Keeping the time required for each wavelength scan shorter than the time over which significant stress changes occur is also important to avoid measurement artefacts: If during a scan over the wavelength the thickness of the micro-cavity changes (e.g. due to cell movement), the recorded reflectivity versus wavelength dataset will be distorted. More precisely, the micro-cavity thickness at the time when the 550 nm image is taken, and the thickness at the time when the 750 nm image is taken, are not the same. It would therefore

[4] How the exposure time influences the measurement quality will be discussed in Section 3.4.5.

[5] Dr. Nils M. Kronenberg measured the relaxation time of the micro-cavities to be below 0.5 s[77], therefore, the time resolution of our measurements is not limited by the mechanical response of the micro-cavities.

not be valid to use this data set to calculate the cavity thickness[6]. In Section 3.4.5 we will validate that decreasing the wavelength range indeed improves thickness calculation of fast moving and indenting objects.

If multiple positions on the sample are investigated, the temporal resolution is reduced by a factor proportional to the number of positions plus the time the stage needs to travel between these positions.

[6] TFM in combination with a confocal microscope has a similar problem, because not all bead positions are measured at the same time.

3.4 Thickness Calculation ("*ERISM-Calc*")

In this section we will discuss all steps to calculate the cavity thickness from the spatially resolved reflectance data. Figure 3.5 visualises the data flow after data acquisition to the fitted cavity thickness at each position of the image. In the following, we briefly summarise the involved steps; each part of the schematic is explained in detail in the next sections.

In the beginning of this chapter we explained that the raw data contains dark and bright fringes, depending on the phase-shift between the light reflected at the top gold mirror and the bottom gold mirror. The minima in the reflectance spectra, or dark areas in the images, are at wavelengths for which the phase-shift between these two beams is 180°. To fit the cavity thickness with the measured reflectance spectra as input, we can compare these minima positions to theoretical predictions for the interference condition.

If the gold layers provided wavelength independent perfect reflection and no other layers except the cavity material were present, one could use Eq. 3.1 to calculate the thickness from the wavelength at which the reflectance spectrum has local minima (cf. Fig. 3.1d bottom; in the following referred to as minima positions). Since in a real device we do not have perfect mirrors but instead a wavelength dependent non-ideal phase shift upon reflection and a dispersive medium within the cavity, we use a transfer matrix algorithm to calculate the expected reflectance spectrum of our micro-cavity structure for different micro-cavity thicknesses. To reduce computation time, the transfer matrix calculation is performed in advance for every possible micro-cavity thickness and a database is created which links each cavity thickness to a set of minima positions (cf. Fig. 3.5 left side). With this database, we can then fit the cavity thickness by simply comparing the minima positions of the experimental data to the minima positions in the database. The use of an optimised algorithm is crucial as — depending on the image size —– the thickness for more than one million pixels has to be fitted for each field of view that is analysed.

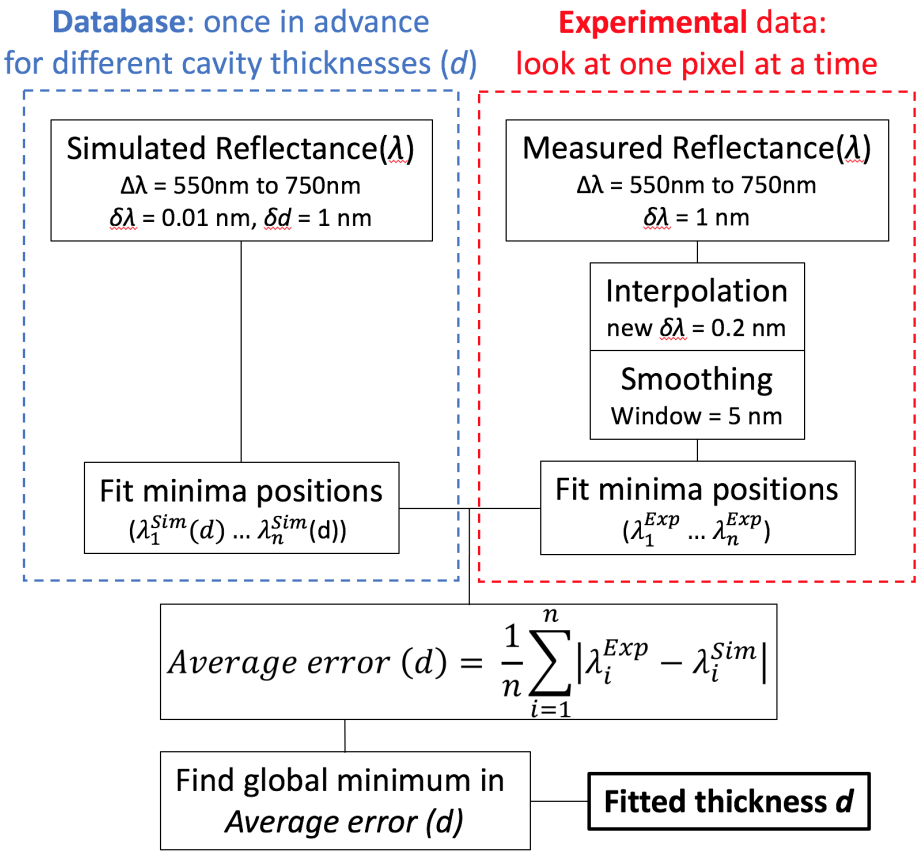

Figure 3.5: Schematic of the algorithm used to fit the cavity thickness for one pixel within the field of view, i.e. for one reflectance over wavelength dataset. The parameters (wavelength range, $\Delta\lambda$; wavelength step size, $\delta\lambda$; thickness step size, d, and smoothing window) listed here are the parameters we use as a standard, but these can be adjusted as needed. The left-hand side (blue box) illustrates how the database containing sets of resonance wavelength $(\lambda_1^{\mathrm{Sim}}(d), \lambda_2^{\mathrm{Sim}}(d), \dots, \lambda_n^{\mathrm{Sim}}(d))$ is created. The right-hand side (red box) describes how the measured reflectance spectrum is treated.

3.4.1 Optical Simulation with Transfer Matrix Method

The code we use for all transfer matrix simulations shown in this thesis is based on an open source *Python* code (*openTMM 0.1.0*) by Yuffa et al.[78]. The core part of transfer matrix calculations in optics is to calculate the Fresnel coefficients at every material interface to determine how much light is transmitted or reflected at each interface. These coefficients are then combined by matrix multiplication to yield the total transmission and reflectance of the structure. Transfer matrix calculations have become a standard tool to characterise and optimise multilayer structures in optics. Therefore, we will not discuss the details in this thesis as the theory is discussed e.g. in the paper of Yuffa et al. To ensure that the open source code of Yuffa et al. yields the correct values, we calculated the reflectivity with the code of Yuffa et al. and the commercially available program *FilmWizard*^{TM} (Scientific Computing International) for different layer structures. Both calculations yielded the same results.

The layer structure for the micro-cavities is (cf. Section 3.2): 0.5 mm glass, 0.5 mm chromium, 10 nm gold, 50 nm SiO_2, 8000 nm elastomer, 15 nm gold. The thicknesses of the gold layers represent a trade-off between high Q-factor, high mechanical sensitivity and sufficient transmittance of light through the cavity to allow combination with phase contrast and fluorescence imaging. A thick top mirror on top of the elastomer would allow increasing the Q-factor but would increase the effective stiffness and thus make the device less sensitive to stress exerted by cells. We will discuss the mechanical characteristics of the micro-cavity in more detail in Section3.5.

We use the following values for the wavelength dependent refractive index $n(\lambda)$ and extinction coefficient $k(\lambda)$: air, $n = 1$, $k = 0$; glass, $n = 1.5$, $k = 0$; gold, values from Ref. [79]; SiO_2, values from Ref. [80]; chromium, values from Ref. [81]; elastomer, refractive index measured with standard ellipsometry, cf. Appendix B.

We simulate the reflectance of this layered structure at normal incidence for a wavelength range from 550–750 nm and for elastomer thicknesses between 7500 nm and 8500 nm

(Fig. 3.6; we find that cells normally do not deform the micro-cavity by more than ±500 nm)[7]. The line plots in Fig. 3.6 show the reflectance at the red and blue lines in the 2D map shown in the main part of the figure. From Fig. 3.6 it is clear that when keeping the wavelength constant, one will see multiple dark areas (fringes) if the cavity thickness changes by more than 230 nm across the field of view. This is beneficial as it provides a real time estimate of thickness differences. On the other hand, it also shows that one cannot determine the local absolute thickness of the micro-cavity from knowing the value of just one resonance wavelength. The free spectral range (FSR) —– which is the spectral separation of two reflectance minima (usually in terms of frequency rather than wavelength) —– is the quantity that determines the order of interference and hence the absolute thickness. Using the frequency ν instead of wavelength as the dependent variable, the FSR for a Fabry-Pérot interferometer can be written as[1]:

$$FSR(\nu) = \frac{c}{2n(\lambda)L} \tag{3.2}$$

where c is the speed of light in vacuum. Since we do not have a perfect Fabry-Pérot interferometer but the layered structure mentioned above, the refractive index and hence the FSR depend on the frequency/wavelength of the light, i.e. there is no single FSR for our micro-cavity. Therefore, to fit the cavity thickness, we instead use the positions of all minima in the measurement range; this means we include the information about the FSR as well as the absolute position of each minimum.

3.4.2 Finding the Minima in the Reflectance Spectrum

The minima positions (orange circles in Fig. 3.6) are extracted from the transfer matrix simulations using a standard peak finding procedure and the wavelengths are stored for each cavity thickness d as, $(\lambda_1^{\mathrm{Sim}}(d), \lambda_2^{\mathrm{Sim}}(d), \ldots, \lambda_n^{\mathrm{Sim}}(d))$, where n is the number of minima in the spectral range considered.

[7] This range is chosen for Fig. 3.6 to visualise the process for fitting the thickness, and is indeed the range we usually need. We actually simulate our database for thicknesses in the range 3000–15 000 nm as for special applications we may require thinner or thicker micro-cavities.

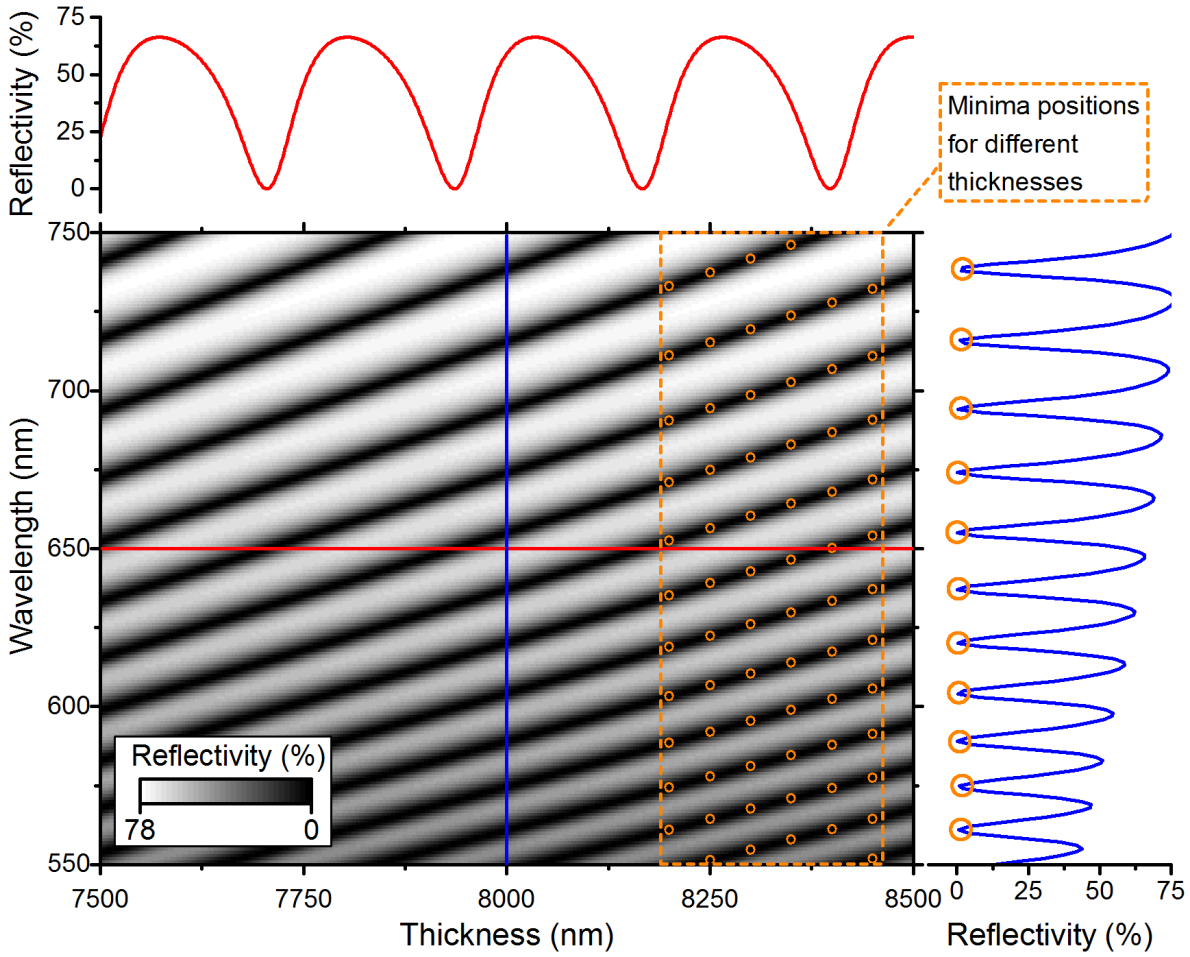

Figure 3.6: Simulated reflectivity for a wavelength range of 550–750 nm and thicknesses range of 7500–8500 nm. The red and blue lines represent profiles for the reflectivity over wavelength and thickness, respectively. The blue profile corresponds to what would be measured in an experiment. The orange circles mark exemplary sets of minima positions corresponding to different thicknesses.

The peak finding procedure used here checks from smaller to larger wavelengths whether the next reflectivity value is larger or smaller than the current one. If it is smaller the algorithm will continue to search for smaller values, if the next value is larger, the program checks whether any smaller values can be found within a predefined range, e.g. in the next 5 nm, to avoid false fits due to noise. If not, a minimum is found and its wavelength stored as $\lambda_i^{\mathrm{Sim}}(d)$. The algorithm continues to search for the next minimum using the procedure above until the end of the wavelength range is reached.

This transfer-matrix calculation and peak finding have to be performed only once for a given layer structure to populate the database linking cavity thicknesses to minima positions (blue box in Fig. 3.5).

3.4.3 Fitting the Micro-Cavity Thickness

A similar procedure is applied to determine the experimental minima positions from the measured data. The set of experimentally measured and fitted minima ($\lambda_1^{\mathrm{Exp}}(d)$, $\lambda_2^{\mathrm{Exp}}(d)$, …, $\lambda_n^{\mathrm{Exp}}(d)$) is then compared to the previously compiled database of cavity thickness d and minima positions ($\lambda_1^{\mathrm{Sim}}(d)$, $\lambda_2^{\mathrm{Sim}}(d)$, …, $\lambda_n^{\mathrm{Sim}}(d)$) (cf. orange circles in Fig. 3.6) by calculating for each thickness d the average error between the experimental minima positions and the simulated ones:

$$AverageError = \frac{1}{n}\sum_{i=1}^{n} |\lambda_i^{\mathrm{Exp}} - \lambda_i^{\mathrm{Sim}}(d)| \tag{3.3}$$

where n is the number of minima found in the experimentally obtained reflectance profile.

Figure 3.7 shows a typical example of how the average error changes with d. There are several local minima which represent cavity thicknesses in intervals of approximately 230 nm and correspond to different cavity modes m (cf. Eq. 3.1). Since ΔL depends on the wavelength, the distance between local minima represents an average value. However, Fig. 3.7 also shows that there is only one global minimum, i.e. one thickness (indicated by red arrow), for which the deviation between the simulated and experimental minima positions is the smallest. (Also note that this minimum is the steepest of the local minima observed.) The thickness associated with this global minimum is taken as the best fit for the local thickness

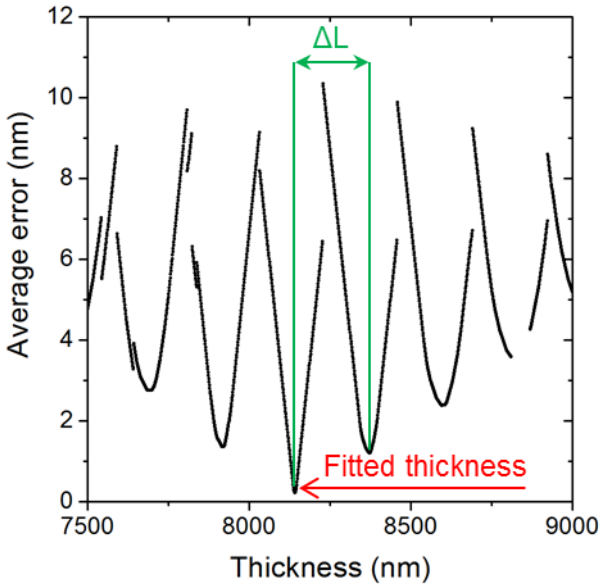

Figure 3.7: Average error as defined in Eq. 3.3 between experimentally obtained minima and simulated minima positions for different micro-cavity thicknesses. ΔL represents the spacing between two minima. The actual thickness of the micro-cavity corresponds to the global thickness where the average error is minimal.

of the cavity at this point. If the signal quality decreases or the cavity thickness changes during one scan —– e.g. due to very fast movement of a cell —– the reflectivity minima positions may change such that the differences in the average error between different cavity modes become smaller. In extreme cases, even a wrong mode number m might be fitted. This issue and ways to mitigate it are discussed later (cf. Fig. 3.12).

3.4.4 Exemplary Thickness Calculation and Background Subtraction

We calculate the thickness of the dataset we showed in Fig. 3.1. The cells in this example are an immortalised 3t3 fibroblast (mouse) cell line .

Most of the time, our micro-cavities are very flat within the field of view and it is often enough to simply subtract a constant value, i.e. absolute thickness, to get the vertical displacement. Here, we show an example with a less flat surface to visualise the process of calculating the displacement by subtracting a background surface.

We plot the thickness map and enhance the contrast such that we plot the thickness values over a range of ±15 nm around the mean thickness to visualise where displacements

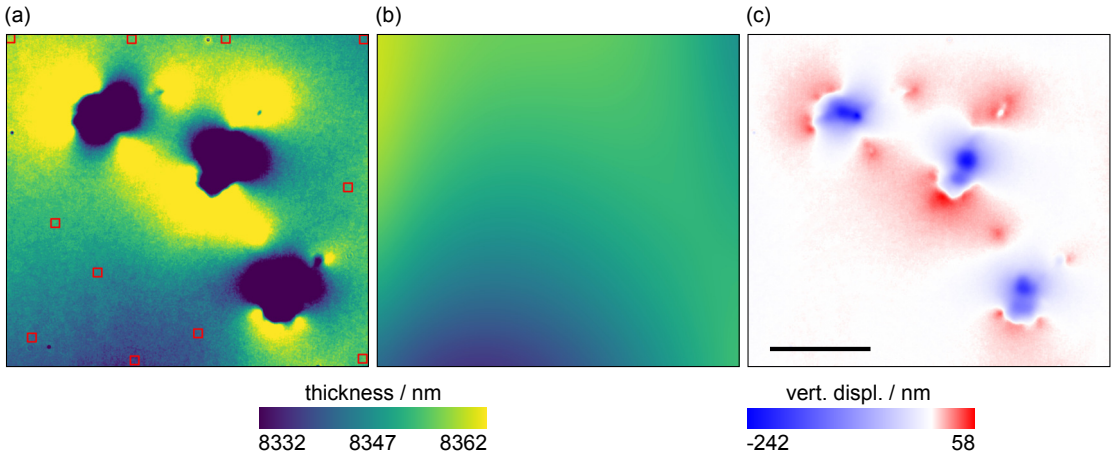

Figure 3.8: Example of background correction. (a) ERISM thickness map obtained for 3t3 cells. The red squares indicate where the values for the calculation of the background were obtained. (b) Background. (c) Vertical displacement obtained by subtracting (b) from (a). Scale bar, 50 µm.

originate from cells (cf. Fig. 3.8a). We select small areas in the thickness map where no displacements of cells are visible (red squares in Fig. 3.8a) and use an *ImageJ* plugin *Nonuniform Background Correction*[82] which takes the mean value of each of these areas to calculate a linear or cubic background (cf. Fig. 3.8b). The background is calculated with subnanometre resolution to avoid that numerical noise of 1 nm steps is added to the result. Finally, the background is subtracted from the thickness map which yields the vertical displacement (cf. Fig. 3.8c).

3.4.5 Precision of the Thickness Calculation

The finite spectral bandwidth of the light used to illuminate the micro-cavity and the desire to perform the measurement quickly limit the smallest possible wavelength step size during acquisition to about 1 nm. However, by interpolating and smoothing, we can localize the position of the reflectance minimum with an accuracy beyond 1 nm. This is analogous to particle localization measurements in super-resolution imaging (e.g. PALM and STORM)[83, 5] and does not represent a violation of Nyquist's theorem.

To investigate the precision of the cavity thickness measurement, we first determine the theoretical limitations by testing our code against simulated test data, i.e. theoretical

reflectance spectra obtained by a transfer-matrix calculation are used for the procedure stated in the red box in Fig. 3.5. This is done using the entire data set from Fig. 3.6, i.e. the full reflectance profiles in a wavelength range for 550–750 nm in 1 nm wavelength steps and for thickness values between 7500–8500 nm in 1 nm thickness steps. These reflectivity profiles are then used to fit the thickness as described above. For this test, the precompiled database of minima positions for each thickness is calculated in 0.01 nm wavelength steps to ensure that the precision of the database is not the limiting factor[8].

The results of these calculations are shown in Fig. 3.9a which plots the difference between the thickness predicted by the algorithm and the nominal thickness. The difference is shown for different interpolation increments which shows that interpolating and smoothing the experimental data indeed improves the precision of the calculation. Without any interpolation the standard deviation and peak to peak deviation of the difference are $\sigma = 1.87\,\text{nm}$ and $\sigma_{\text{ptp}} = 8\,\text{nm}$. Both values decrease significantly when the data is interpolated with increments of $\delta\lambda = 0.2\,\text{nm}$ and smoothed with a 5 nm moving average filter[9]. However, we do not observe a further significant improvement by interpolating the data at $\delta\lambda = 0.1\,\text{nm}$ increments versus $\delta\lambda = 0.2\,\text{nm}$.

Next, we investigated the influence of noise on the precision of the thickness fitting. Gaussian noise with different standard deviations (stated as "Noise =" in Fig. 3.9b) was added to the reflectance spectra before the thickness fitting was performed. The results are summarised in Fig. 3.9b; the blue profiles show the reflectivity spectra for a micro-cavity thickness of 8000 nm with different amounts of noise added; the histograms summarise the deviation between nominal and fitted thickness for the entire 7500–8500 nm thickness range. In Fig. 3.9b the first column (Noise = 0) represents the same data as in Fig. 3.9. The column in the middle (Noise = 500) represents a scenario similar to experimental noise under standard conditions. The results show that interpolating and smoothing the data greatly improves the precision of the thickness fitting: the standard deviation of the deviation

[8] In fact, we also use $\delta\lambda = 0.01\,\text{nm}$ for the precompiled database, which we use to fit our experimental data, to rule out that any artificial numerical noise is created by using larger steps. Although creating the database takes longer for smaller steps, this is not an issue because it only has to be done once.

[9] Note, without applying a moving average filter, but only interpolating the data, the resolution would not increase because we perform a linear interpolation.

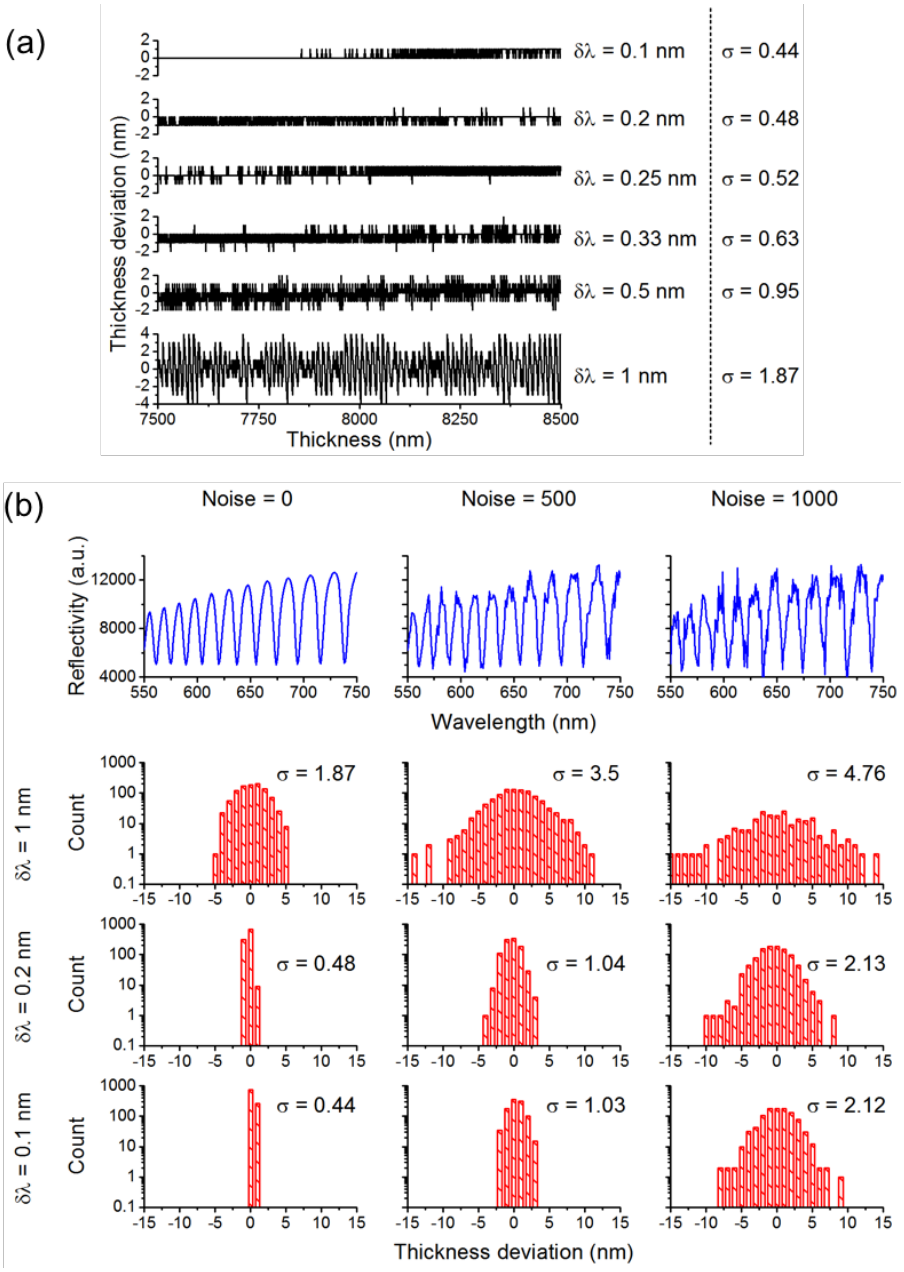

Figure 3.9: Testing the precision of the thickness fitting algorithm with reflectance data produced by transfer matrix calculations, i.e., same data as in Fig. 3.6. Different interpolation conditions and different amounts of Gaussian noise added to the data are compared. (a) Difference between nominal and fitted thickness for different increments of wavelength interpolation $\delta\lambda$. σ is the standard deviation of the difference between nominal cavity thickness and fitted thickness. (b) Difference in thickness for different $\delta\lambda$ and different amounts of Gaussian noise (standard deviation of noise 0, 500, and 1000). The blue profiles (top) illustrate how the added noise affects the reflectance spectra (cavity thickness, 8000 nm). Note that the total amount of fitted pixels is only 20% for noise = 1000, $\delta\lambda = 1$ nm.

between nominal thickness and fitted thickness is reduced from 3.5–1.04 nm (Noise = 500) by interpolating in $\delta\lambda = 0.2$ nm steps. We see this improvement for all three noise levels but see no significant further improvement for any of the noise levels when using $\delta\lambda = 0.1$ nm. Therefore, $\delta\lambda = 0.2$ nm will be used to save computation time. We attribute the fact that we do not see a further improvement in precision to the statistical effect of fitting actually multiple (N) minima positions so that the average error from Eq. 3.3 should be divided by $\sqrt{N}$.

We also test how our approach of interpolating and smoothing the data before fitting the minima positions compares to fitting each minimum with a peak function. (We used a Gaussian here as we find that it describes the broad and partly overlapping minima better than a Lorentzian.) For this we take the simulated reflectivity plot for a cavity thickness of 8000 nm (blue line in Fig. 3.6) and, without performing any initial interpolation or smoothing of the data, fit each minimum position with a Gauss-function. Equation 3.3 is then used to calculate the average error of the determined and simulated (true) minima positions. For comparison, we apply the same method used before, i.e. interpolating with 0.2 nm increments, smoothing with a 5 nm moving average filter, finding the minima with the simple minimum finding algorithm described above and then applying Eq 3.3. We find that the average error is 0.19 nm for the interpolation and smoothing approach and 0.18 nm for fitting the minima positions with a Gauss-function. We therefore conclude that fitting a Gauss-function does not lead to a significantly more accurate fit. However, it is computationally much more demanding than our approach (a least square fit has to be carried out for each minimum separately), and in addition requires an initial guess of the approximate positions of the minima. In light of the large number of reflection spectra that need to be analysed, the interpolation and smoothing approach combined with the simple minima finding algorithm described above is therefore more suitable.

Finally, in order to estimate the thickness resolution of our approach, we derive a relation between changes in the position of minima and changes in cavity thickness. The derivative of Eq. 3.1 is $\frac{d\lambda}{dL} = \frac{4n(\lambda)}{2m+1}$ and provides a measure of how much one reflection minimum shifts per 1 nm change in cavity thickness. Because m is not necessarily know and has to be

calculated, we rearrange the relation:

$$\lambda = \frac{4Ln(\lambda)}{2m+1}$$
$$2m+1 = \frac{4Ln(\lambda)}{\lambda}$$
$$\frac{\boldsymbol{d\lambda}}{\boldsymbol{dL}} = \frac{4n(\lambda)}{2m+1} = \frac{4n(\lambda)\lambda}{4Ln(\lambda)} = \frac{\boldsymbol{\lambda}}{\boldsymbol{L}}$$

For typical values (λ = 650 nm and L = 8000 nm) we find that each minimum shifts by 0.08 nm nm^{-1} (change in wavelength per nm thickness change). The calculations in the previous paragraphs showed that the average error in the spectral position of the reflection minima is between 0.19 nm and 0.24 nm (depending on whether or not noise is considered). This would imply an error in the thickness measurement of $\frac{0.24\,\text{nm}}{0.08\,\text{nm}\,\text{nm}^{-1}} \approx 3\,\text{nm}$. However, as the thickness fitting algorithm considers about ten minima across the investigated wavelength range (typically 550–750 nm), the precision of the thickness measurement improves to $\frac{0.24\,\text{nm}}{0.08\,\text{nm}\,\text{nm}^{-1}\sqrt{10}} \approx 1\,\text{nm}$.

Test Precision with Real Data

In this section, we will investigate the influence of the spectral band-width of the light used to illuminate the micro-cavity, the camera exposure time, and the roughness of the cavity mirrors on the precision of thickness fitting. Measurements were taken on a flat, non-deformed region of the micro-cavity (same micro-cavity as in Fig. 3.1 and Fig. 3.8) using multiple exposure times and different bandwidth[10] The results of this experiment are summarised in Fig. 3.10.

We find that higher exposure times generally lead to less noisy reflectivity profiles (cf. Fig 3.10a) and consequently yield less noisy thickness maps (cf. Fig. 3.10b). For the longest exposure time tested (250 ms), a surface structure, which we attribute to local roughness of the gold mirrors, is resolved. To quantify the quality of our measurement, we calculate the average error (cf. Eq. 3.3) for different combinations of exposure time and band-

[10] Bandwidth was adjusted by changing the slit widths of the monochromator used in the experimental setup for recording ERISM data.

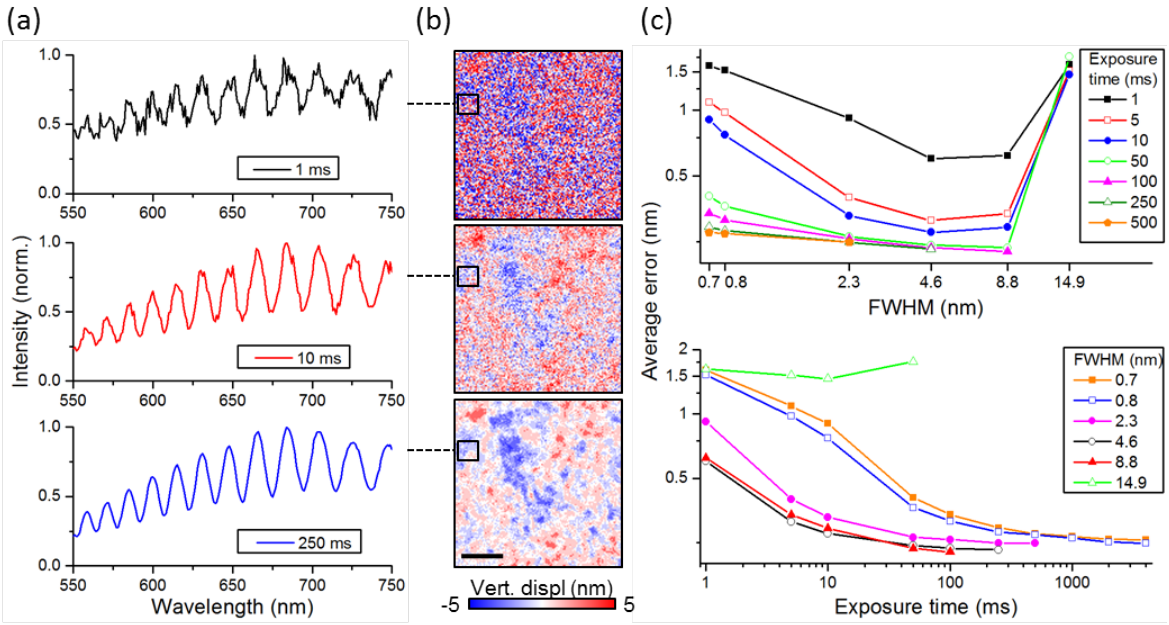

Figure 3.10: Investigation of the influence of the spectral bandwidth of the light source (full width half maximum, FWHM) and camera exposure time on the thickness fitting for a flat micro-cavity. (a) Reflectance spectra for a single pixel within the field of view for different exposure times (spectral bandwidth, 4.6 nm). (b) Thickness of micro-cavity for the same exposure times as in (a); scale bar, 5 µm. Black box indicates pixel (only one pixel in each box) for which spectrum is shown in (a). (c) Average deviation between experimentally determined and simulated sets of minima for the fitted cavity thicknesses versus spectral bandwidth (top) and camera exposure time (bottom).

widths (FWHM), taking in each case the mean over the whole field of view of our system (1024 px × 1280 px corresponding to 166 µm × 207 µm) (cf. Fig. 3.10c).

When the exposure time is kept constant, the average error decreases with increasing bandwidth. This is expected since more light can pass through the monochromator slits improving the signal to noise ratio. However, if the bandwidth is too large (e.g. bandwidth 14.9 nm), the interference contrast reduces drastically which then results in large average errors for all exposure times we applied. Furthermore, we find that increasing exposure time only reduces the average error significantly for exposure times up to 10 ms (when using bandwidth with FWHM >= 2.3 nm), indicating that beyond a certain signal to noise ratio, the thickness fitting does not improve any more.

The slits yielding FWHM bandwidths of 4.6 nm and 8.8 nm perform nearly equally well and our data indicates that a bandwidth below 4.6 nm does not improve the precision of the fit. As we will describe in more detail later, it is often desirable to keep the overall scan time short (to avoid artefacts from cell-induced thickness changes during the scan). We therefore conclude that slits yielding a FWHM bandwidth of 4.6 nm (physical width of the slits, 0.6 nm) and an exposure time of 10 ms are the measurement parameters providing the best thickness precision while maintaining a low overall scan time. The mean average error for these measurement parameters is 0.25 nm; this is comparable to the value estimated with simulated data (0.24 nm cf. Section 3.4.5) and corresponds to 1 nm precision for the thickness fitting. We therefore also conclude that it is sufficient to fit the cavity thickness in 1 nm steps, i.e. to use 1 nm thickness increments in the simulated database. We note that the presently used fabrication process for ERISM micro-cavities have an RMS surface roughness of approx. 3 nm.

Limitations of the Thickness Fitting

For very short exposure times (<10 ms), steep changes in cavity thickness (high gradients), and very dynamic processes that induce considerable thickness changes during the wavelength scan, the thickness fitting can yield inaccurate results. To increase the robustness of our algorithm and to prevent unphysical results, we included a parameter $tolerance$.

The thickness for a certain point in the image is set to Not a Number (NaN) if the average error is above the tolerance. Setting the tolerance to a value of 1 nm in wavelength would correspond to a maximum allowed deviation in thickness of 12.5 nm. Since the average error mainly increases for large deformations (>150 nm) allowing pixels to be fitted with a 12.5 nm inaccuracy is still reasonable as it corresponds to a maximum error in the measured deformation of less than 10%. Note that for small deformations, the precision of the measurement is much higher (as described above) as the tolerance compliance is not reached.

If the fitting algorithm fails to determine the thickness correctly, most frequently the fitted thickness corresponds to a higher or lower mode number (m) compared to the surrounding pixels. Thickness changes by one mode order between adjacent pixels are unphysical in most conductions (1px $\widehat{=}$ 160 nm; the approximated thickness difference between two modes is at $\Delta L = \frac{\lambda}{2n(\lambda)} \approx 230\,\text{nm}$ at $\lambda = 650\,\text{nm}$). We attribute the "jumps" in thickness between mode numbers to a deterioration of the signal for these extreme conditions described above, and hence, less accurate fitting of the minima positions. To understand this better, we compare the minima positions for two adjacent mode numbers m_1 and m_2, with $m_2 = m_1 + 1$ and the central minimum at the same position. The average error between these two sets of minima is 1.33 nm. A measured dataset which "jumps" between these two different thicknesses would therefore have an average error of approx. $1.33\,\text{nm}/2 = 0.67\,\text{nm}$.

As described above the average error between experimentally obtained/fitted and simulated minima positions is approx. 0.25 nm (much smaller than 0.67 nm) — we confirmed this value with different datasets (data not shown). Unphysical jumps between modes and fitting a thickness corresponding to the wrong mode number are therefore usually not an issue.

In rare cases, mode jumps have been observed, we have therefore implemented an optional feature that stops the fitting algorithm from predicting a thickness that differs by more than a certain value from the thickness of the adjacent pixel (typically 50 nm per pixel are used). This feature leads to more consistent data but at present is very rarely required. It might become more important if faster processes are investigated.

For the thickness calculations in Fig. 3.10 we used a $tolerance$ of 2 nm to show how strongly the measurement parameters change the average error. However, when using the two slits with the smallest FWHM at 1 ms and 5 ms exposure time and for all exposure times used with the largest slit, 90%-99% of the values had an average error above 2 nm and were therefore not considered in the statistic. On the other hand, using the standard parameters as stated above, we routinely fit 99.99% of all pixels; with the non-fitted pixels usually being at positions where the micro-cavity has defects (e.g. due to dust captured during the fabrication process).

Increasing Measurement Speed by Measuring One Minimum

If fast processes are monitored with ERISM or if multiple fields of view are to be tracked at the same time, one may want to optimize the time it takes to record the required data. As we described in Section 3.3.3, the time for one measurement is (8.0 ± 0.5) s for a wavelength range of 550–750 nm. One frame every 8 s is potentially too slow to investigate fast moving cells like amoeba[84]. Measuring only every 8 s could first of all lead to events or patterns of interest not being detected simply because the frame rate is too low. Furthermore, if a thickness change occurs during an 8 s measurement, the measured reflectance profile could be distorted which may result in fitting the wrong thickness or in the software not finding any thickness.

Most of the measurement time is spent in taking the images with the camera and moving the monochromator, hence, one could reduce exposure time and increase the speed of wavelengths tuning. However, substantial improvements would require significant increase in the intensity of illumination (which can be problematic) and recording and storing the data could become challenging. (The present implementation uses a conventional solid-state drive and a camera connected via CameraLink.) We therefore suggest an alternative method where the cavity thickness is fitted by tracking the position of only one reflectance minimum which allows a reduction in the scan range (e.g. to 620–660 nm instead the 550–750 nm range required for tracking multiple minima) and results in a four-fold reduction in measurement time.

With this scheme one can only determine the absolute thickness if the mode of interference m or the FSR is already known (cf. Eq. 3.1 and Eq. 3.2). Then, once the absolute thickness is determined, changes of the cavity thickness can be calculated from the position of one single minimum in the reflectance spectra. In addition, only thickness shifts smaller than half the thickness shift between two adjacent modes (approx. 115 nm, cf. section *Limitations of the Thickness Fitting* and Fig. 3.11) can be calculated, otherwise it is not clear whether the thickness increased or decreased. Consequently, one has to perform one measurement over the full 550–750 nm range to obtain the initial absolute thickness map of the micro-cavity. In practice, this is not an issue as this can be done before the actual experiment.

We visualise this concept in Fig. 3.11. The green line in Fig. 3.11 shows how the position of a single minimum in the 620–660 nm would change for different cavity thicknesses (again considering the thickness range between 7500–8500 nm, as before, and always taking the longer wavelength minimum within the investigated range). The minima positions used when fitting the cavity thickness based on data from the 550–750 nm is also shown (cf. orange circles in Fig. 3.11).

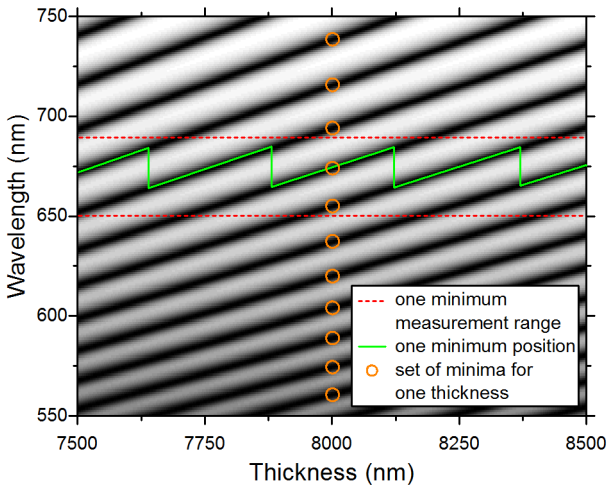

Figure 3.11: Visualisation of the minima positions for the standard algorithm for one thickness (orange circles) and the minimum position for a range of thicknesses for the one minimum fitting algorithm.

To demonstrate the benefit of this approach for measuring a dynamic system, we performed the following experiment (cf. Fig. 3.12). A bead was attached to the cantilever of an atomic force microscope (AFM)[11] and the cantilever indented by ≈ 130 nm into one of our micro-cavities using the piezo-stage of an AFM (Nanosurf). The cantilever was moved at different speeds (200, 500, 1000 nm s^{-1}) across the surface of the cavity with the bead still indented. Measurements were taken at the maximum possible speed (camera exposure time, 10 ms) for both a wavelength range of 201 nm and for a range of 41 nm.

If the cavity thickness changes during a measurement, the reflectance spectra are distorted because the reflectance changes with the cavity thickness (cf. Fig. 3.11). In other words, each point of a reflectance spectrum would correspond to a different thickness. Hence, it is difficult to tell which intensity changes in the reflectance spectra are linked to the change in wavelength during the scan or which are linked to the change in cavity thickness because of the moving object; this is likely to lead to a less accurate thickness fit.

In fact, we observe that with increasing speed the fitted thickness to the left and right of the centre of indentation takes unphysical values. More precisely, the thickness can be fitted but at pixels where the thickness increases during the scan, the minima in the reflectance spectra will have a lager spacing[12], and hence the fitted thickness is for the next lower cavity mode order. For instance, instead of 8000 nm, a thickness of 7770 nm is fitted, which corresponds to the green pixels in Fig. 3.12b. On the other side (right) of the centre of indentation the thickness decreases during the scan. In this case, the spacing between the minima is smaller, resulting in a fitted thickness which is 230 nm thicker than it should. These pixels are coloured magenta in Fig. 3.12b. The observation we describe here is analogue to the Doppler-effect in acoustics.

When we analyse our data using only the smaller range of 620–660 nm the described unphysical values do not occur. Because only one minimum is used to fit the thickness the mode cannot change. Our data thus shows that we not only increase the frame rate by a factor of 4 but that we can also fit the data at cantilever speeds where no good fit is possible

[11] We will give a more detailed introduction into AFM in Section 3.5.1.
[12] Because the minima are red-shifted for increasing thickness.

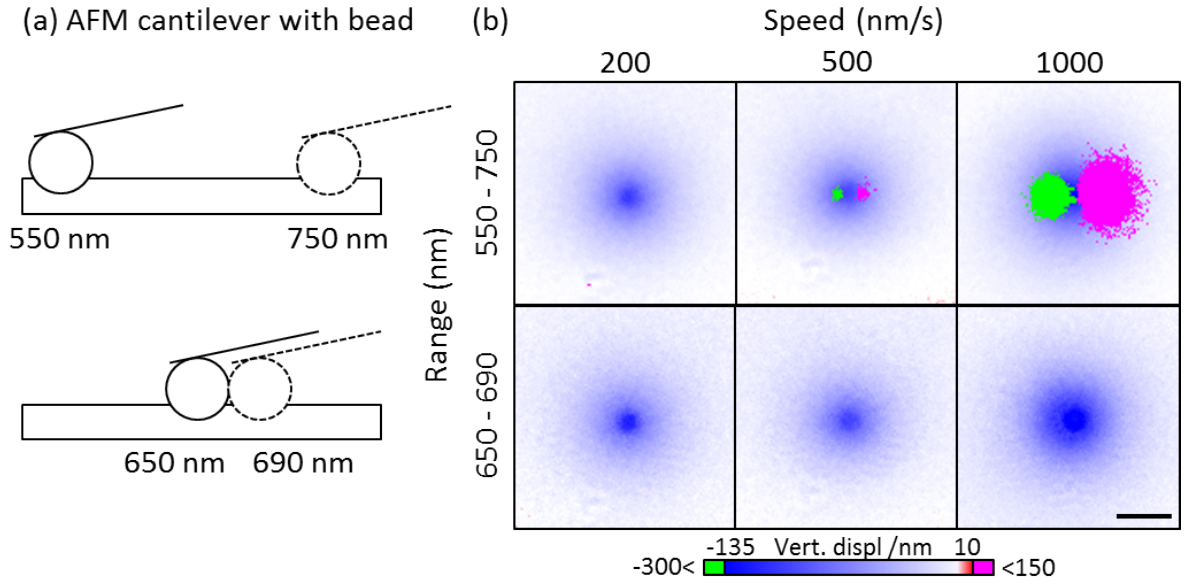

Figure 3.12: Comparison between fitting the cavity thickness with all minima within a range of 550–750 nm and with only one minimum in the 650–690 nm range. (a) Schematic of the AFM cantilever positions at the start and end of one ERISM scan when the cantilever is moved across the sample whilst indenting into the micro-cavity. (b) Fitted vertical displacement for different cantilever speeds and fitting ranges. Green and magenta represent pixels for which unphysical values (< -300 nm,green and > 150 nm, magenta) were fitted. Scale bar, 5 µm. All images are centred on the maximum indentation.

with the full data range. The reduction of the total data size is another advantage of this approach.

A potential drawback could be that we do not achieve the precision in thickness of the multiple minima fit. We investigate this further and apply the one-minimum algorithm to calculate the thickness for the simulated reflectance data with Noise=500 (cf. Fig. 3.9). We then subtract the result from the nominal thickness to get the deviation between nominal thickness and experiment. Similar to our analysis in Fig. 3.9, we are interested in the standard deviation as a measure of how well the fitted thickness values align to the nominal thickness values.

The values are listed in Tab. 3.1 together with the standard deviation for the algorithm which considers all minima in a range of 550–750 nm. Without interpolation and smoothing ($\delta\lambda = 1$ nm) the standard deviation for the one minima algorithm is more than twice as big as for the standard algorithm. For both algorithms it does not make a significant difference if the signal is interpolated in 0.2 nm or 0.1 nm steps. Once the data is interpolated, the standard deviation for both algorithms decreases by a factor of ~3. Although the standard deviation of the one minimum algorithm (2.73 nm) is still more than twice as big as the standard deviation for the multiple minima algorithm (1.04 nm), 2.73 nm is comparable to the surface roughness of the sensor with an RMS of 3 nm. In addition, we expect the precision in our experiments to be even better if we subtract the roughness by taking a reference image and apply a Gaussian filter. We will show in Section 4.4.2 that by adding these steps, we can detect thickness changes down to 0.5 nm. We conclude that using the one minimum algorithm will not decrease the precision of the thickness fit significantly and is therefore beneficial to use in order to achieve a higher frame rate and reduce data size.

Speed of the Thickness Calculation

We choose *Python*[85] as a programming language to write *ERISM-Calc* which receives the raw ERISM measurement data as input and then: 1) performs the interpolation and smoothing, 2) fits the minima positions, 3) fits the set of minima from the experiment to the precompiled database to obtain the cavity thickness. Python has the advantage that many

Table 3.1: Comparison of the expected precision for the thickness calculation between standard fitting algorithm and one minima fitting algorithm. Calculations performed in the same way as for the data with Noise = 500 in Fig. 3.9. Standard deviation of the difference between thickness fit (of simulated reflectance data for cavity thicknesses of 7500–8500 nm) and the nominal thickness values.

Interpolation increment $\delta\lambda$	1 nm	0.2 nm	0.1 nm
Standard deviation [nm] 550–750 nm standard minima fit	3.5	1.05	1.03
Standard deviation [nm] 650–690 nm one minimum fit	7.34	2.73	2.64

libraries are available, e.g. to read or smooth images, and that it is usually faster to develop programs in Python compared to low-level programming languages like *C*.

However, we found that the time we needed to calculate the thickness for 1024 × 1280 pixels was more than 1 h. Although the calculations can be done after the measurement, such long computation times are impractical if thousands of measurements have to be analysed. We addressed this issue by carefully optimising the different algorithms and moving the computation heavy parts of the code into a precompiled *C++* library. The latter was done using *Cython*[86], a Python module, which allows to preserve almost all of the user friendly Python syntax and automatically converts the Python code into compiled C++ code.

After these optimisation steps we achieved computation times of approx. 1 min for 1024 × 1280 pixels when fitting multiple minima of the reflectance spectra, and 20 s when using the one minimum algorithm. Furthermore, we can run multiple instances of *ERISM-Calc* in parallel on a multi-core CPU and thus effectively achieve computation times down to 5 s for the one minimum algorithm[13].

These computation times are fast enough to analyse large data sets (cf. Section 4.2) and ERISM-Calc could even be integrated into ERISM-Read to calculate the cavity thickness parallel to the ERISM measurement.

[13] Calculations are performed on a Windows PC with Intel®Core™ i7 3770K at 3.5 GHz (quad core) and 8 GB of RAM.

3.5 Mechanical Characterisation of ERISM Micro-Cavities with AFM

In the previous section we explained in detail how and to which precision we can measure the local thickness and displacement of an ERISM micro-cavity. Spatially resolved displacement maps are already valuable because it is possible to see were cells exert forces, if these forces change over time, and how displacements (e.g. the maximum displacement) vary between different cells. In addition, it can also be of value to know the actual stresses or forces the cells are exerting. This is important for several reasons including to compare results obtained by different force sensing techniques or to investigate stress dependent processes rather than displacement depend processes, i.e. the same stress leads to different displacements on substrates with different stiffness.

Similar to other force sensing techniques, once displacements are measured with ERISM, stress and forces can be calculated if the material properties of the substrate are known. Therefore, in this chapter we will investigate the mechanical properties of the ERISM micro-cavities. We will use atomic-force-microscopy (AFM) as a tool to exert known forces on the sample and measure the displacements with ERISM.

We will first introduce the basics of AFM to motivate how we can use this technique for ERISM micro-cavity characterisation. We will then perform nano-indentation measurements to apply known forces with the AFM to pristine elastomer samples (no oxide and gold layer on top) and to complete micro-cavities. Combined with a finite element method this will give us the Young's modulus of the elastomer, which is required to calculate the stress and force from displacements. After characterising the response of the micro-cavities to vertical forces, we will use the AFM to apply horizontal forces and observe the micro-cavity response with ERISM. Finally, we will apply what we learned from these measurements and calculate for representative examples the stress exerted by a cell.

3.5.1 Atomic-Force-Microscopy (AFM)

Atomic-Force-Microscopy (AFM) is a widely used high resolution imaging, micro-manipulation, and force-spectroscopy technique. The core concept of AFM is to measure the bending of a cantilever due to changes in the sample height or the force exerted on the cantilever (cf. Fig. 3.13a). This is done by pointing a laser beam at the end of the cantilever and measuring the position of the reflected laser light with a photo-diode based detector. The cantilever position can be changed with piezo ceramics. For imaging, a cantilever with a sharp tip (one or only a few atoms at the end) is moved over the substrate and the deflection of the cantilever is measured. This yields information about the height profile of the sample. An AFM can easily be utilised as a micro-manipulator since it already has the ability for positioning the cantilever in all three dimensions. In addition, different cantilevers are available for different applications, e.g. to electrically characterise or manipulate the sample surface, to move or reposition micro-particles or even atoms on the sample surface, as a micro-pipette (hollow cantilever and/or tip with hole at the end) to remove or inject particles e.g. into cells.

Nano-Indentation with Spherical Indenter – Hertz-Model

For this thesis the force-spectroscopy aspect of AFM is most relevant. We use the displacement maps we obtain with ERISM and ERISM-Calc as input to calculate the stress with a finite-element-method. This requires knowledge about the mechanical properties of the micro-cavity. AFM is widely used to measure the Young's modulus of different kinds of materials. Here, instead of using a sharp tip, usually a sphere is attached to the end of the cantilever (cf. Fig. 3.13b) as the theory of contact mechanics is much simpler for a sphere as compared to a sharp tip and the occurrence of extremely high peak stresses can be avoided. The sphere is then indented into the sample. If the spring constant of the cantilever is known[14], the sphere can be indented with a known force. At the same time, the indentation depth of the sphere can be calculated from the z-position of the piezo and the cantilever bending. Finally, the so acquired *force-distance-curves* can be fitted with an equation given

[14] We are referring here to the spring constant k_z which describes how much force is needed to move the end of the cantilever up or down. In Section 3.5.4 we will discuss the different spring constants and cantilever mechanics in more detail.

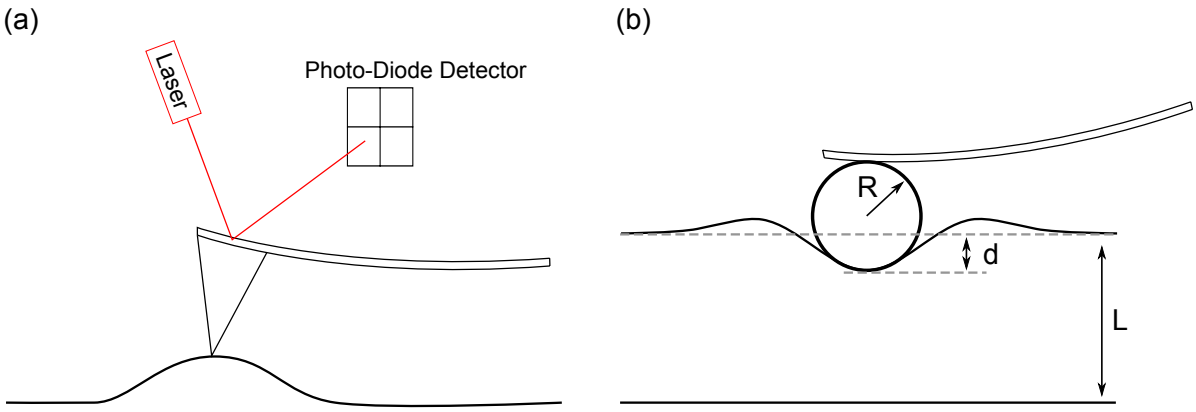

Figure 3.13: (a) AFM cantilever with tip, laser beam is reflected at the top of the cantilever and collected by a photo-diode detector. (b) AFM cantilever with spherical indenter.

by the Hertz-Model with the Young's modulus as a free parameter. For a spherical indenter indenting into a half-space the indentation force F and indentation depth d are related as follows[87]:

$$F = \frac{4}{3} E^* R^{\frac{1}{2}} d^{\frac{3}{2}} \tag{3.4}$$

Here E^* is the effective Young's modulus of indenter and half-space (cf. Eq. 3.5) and R is the radius of the sphere. The Hertz-Model makes the following assumptions[87]: both, indenter and sample are perfectly linear elastic materials, i.e. no hyperelastic, plastic or viscoelastic effects, no inhomogeneities; the contact area is small compared to the radius of the sphere; no other forces between indenter and sample, e.g. adhesion or friction[15]; the indentation depth is small compared to the sample thickness, i.e. the stiff substrate has no influence on the indentation depth at a given force. The effective Young's modulus E^* in Eq. 3.4 combines the Young's modulus E_{Sp}, E_{El} and Poisson's ratio ν_{Sp}, ν_{El} of the sphere and elastomer respectively[87]:

$$\frac{1}{E^*} = \frac{1-\nu_{\mathrm{Sp}}^2}{E_{\mathrm{Sp}}} + \frac{1-\nu_{\mathrm{El}}^2}{E_{\mathrm{El}}}. \tag{3.5}$$

We use glass beads for the indentation measurements which are approximately six orders of magnitude stiffer than the elastomer. Therefore, we can write $E^* = \frac{E_{\mathrm{El}}}{1-\nu_{\mathrm{El}}^2}$.

[15] We perform the indentation measurements in a buffer solution with high salt concentration to avoid electrostatic effects between micro-cavity surface and glass bead.

Equation 3.4 assumes that the sample is infinitely thick compared to the indentation depth. This does not apply to our measurements with a sample thickness of around 8 µm and indentation depths up to 1 µm. We therefore use a corrected Hertz-Model which describes the indentation of a spherical indenter into an isotropic linear elastic layer with finite thickness L on an infinitely stiff substrate[88]:

$$F = \frac{4}{3}\frac{E_{\mathrm{El}}}{1-\nu_{\mathrm{El}}^2} R^{\frac{1}{2}} d^{\frac{3}{2}} \left[1 + 1.133\chi + 1.283\chi^2 + 0.769\chi^3 + 0.0975\chi^4\right]. \tag{3.6}$$

With $\chi = \frac{\sqrt{Rd}}{L}$. We assume a Poisson's ratio of $\nu = 0.49$, a value previously reported for the structurally similar PDMS. With Eq. 3.6 we can now extract the Young's modulus for an 8 µm thin elastomer layer on a glass substrate from AFM indentation measurements.

3.5.2 AFM Indentation Measurements on ERISM Micro-Cavities

We investigate the mechanical difference between pristine elastomer samples and full micro-cavities with bottom and top mirrors[16]. A cantilever with a sphere (r = 5 µm) was indented into the samples to record force distance curves. Force distance curves were taken multiple times in forward (indentation) and backward (retraction) direction at the same sample position without observing significant changes between the measured curves indicating that the sensor fully relaxes into its initial states without taking damage[77]. The curves were fitted with Eq. 3.6 (cf. Fig. 3.14 blue and green lines) to extract the Young's modulus for the two samples. We found that the complete micro-cavity has a stiffness of (3.2 ± 0.7) kPa which is stiffer than to the pristine elastomer sample with (1.4 ± 0.8) kPa but within a similar range. Furthermore, collaborators measured the Young's modulus of a macroscopic elastomer sample with conventional rheology and obtained a value of $E_{\mathrm{EL}} = (460 \pm 10)$ Pa[17]. It is unlikely that the stiffness of the elastomer itself, i.e. of the bulk, has changed in the complete micro-cavity or even in the pristine elastomer. We therefore attribute the difference in

[16] Measurements and fitting of the force distance curves were performed by Dr. Nils. M. Kronenberg.
[17] We thank Giuliano Scarcelli for providing us with this data.

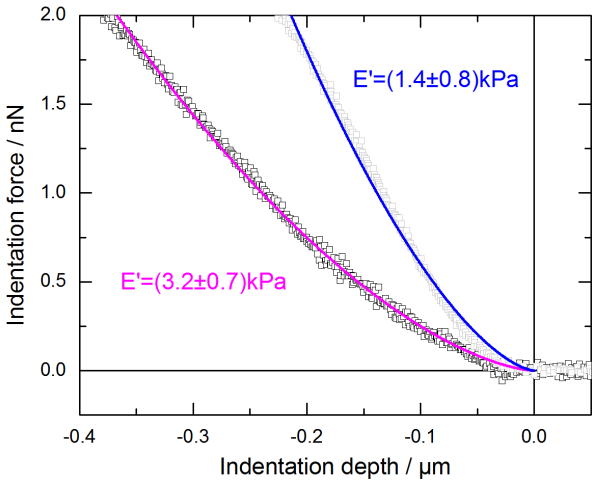

Figure 3.14: Representative force distance curves and corrected Hertz model fits (cf. Eq. 3.6) for pristine elastomer sample (magenta) and full micro-cavity (blue). The apparent Young's Modulus E' was obtained from the Hertz model fit of five independent measurements for each sample. Measurements and data analysis were performed by Dr. Nils M. Kronenberg.

apparent stiffness between the cavity sample and the bulk elastomer to the SiO_2 layer formed on the surface during plasma treatment and to the deposited gold film (cf. Section 3.2).

However, the Young's modulus obtained with AFM measurements for the pristine elastomer sample is also three times higher than the value obtained with rheology. To understand this, we measured untreated elastomer samples at different time points and found that one week old samples show a nearly threefold increase in stiffness. This observation is consistent with the formation of a natural oxide layer on the surface if the elastomer. An increase of the Young's modulus over time was not observed for the full micro-cavities suggesting that the oxide layer from the plasma treatment and the gold film protect the samples from further oxidisation.

We acknowledge that multilayer structures like elastomer/natural oxide or elastomer/oxide/gold are not explicitly covered by the corrected Hertz-Model. However, we find that Eq. 3.6 does describe the data well, therefore, we will refer later in the text to Young's moduli obtained by this method as apparent Young's moduli E'. Moreover, we perform further measurements and data analysis to characterise the micro-cavity multilayer system in order to extract meaningful quantities to calculate the stress from ERISM displacement maps.

ERISM in Combination with AFM

For the following experiments we used a batch of micro-cavities fabricated earlier and thus with less well optimised process parameters compared to the sample we used to acquire the data in Fig.3.14. We expect that the sample discussed in the following had an even thicker SiO_2 layer compared to the sample with $E' = (3.2 \pm 0.7)$ kPa in Fig.3.14. We did not record force-distance curves to extract the apparent Young's modulus of this sample with the corrected Hertz model, however, we will use a finite element method approach (see the coming sections) and get $E' = (12 \pm 1)$ kPa. Furthermore, we will show that our findings for this stiffer sample are valid for the softer sample as well.

We combine AFM measurements with ERISM to obtain the spatially resolved change in cavity thickness of a micro-cavity during AFM indentation. With this combination of AFM and ERISM we can extract the indentation profile at the applied indentation force. This is interesting in itself as the indentation profile provides additional information about the sample but is difficult to assess with other methods.

We applied four different forces (5 nN, 10 nN, 15 nN, 20 nN) and kept the position of the AFM cantilever for 20 s to perform an ERISM measurement. From each displacement map (see example for 10 nN in Fig. 3.17a) we obtained the indentation profile by building the average over 360° around the maximum indention (cf. Fig. 3.17a). All four indentation profiles are shown in Fig. 3.15. In the following sections we discuss how the profiles obtained with ERISM and AFM, obtained profiles compare to finite element simulations for single and multilayer structures. We will first have a brief look at the general concept of finite element simulations and will then apply these simulations to our problem.

Introduction to the Finite Element Method (FEM)

The *finite element method* (FEM) was developed to provide numerical solutions for complex problems. FEM is widely used to solve engineering problems, e.g. to simulate the statics or dynamics (e.g. wind) of a large bridge. Because of the complex geometry of a large bridge, there is no analytical solution available which would describe the forces acting at each point.

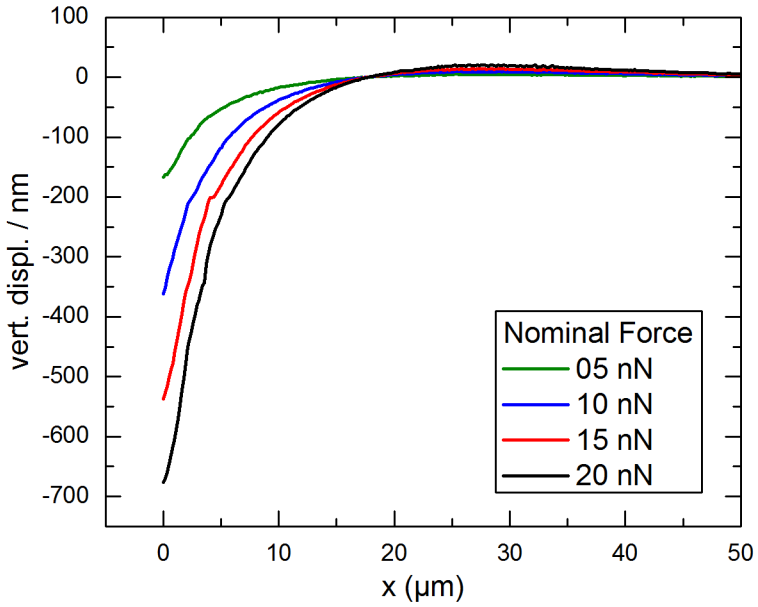

Figure 3.15: Indentation profiles obtained as described in the text for four different forces.

However, this is of course important to know in advance in order to judge which structures and materials are necessary to support a certain load (trains, cars, etc.).

The core concept behind FEM is to divide a complex geometry into smaller *finite elements* and solve the relevant equations (usually partial differential equations) for each element. Then, for given boundary conditions and starting values the whole problem is solved by iteratively solving this large set of equations. Because of FEM being a tool to solve partial differential equations for complex geometries, it is used in different areas of physics like: optics, electrodynamics, structural mechanics, fluid dynamics, etc.

The main steps in a finite element analysis (FEA)[18] usually involves: setting up the geometry, e.g. drawing the 3D shape of a bridge; defining boundary conditions, e.g. where is a structure fixed in space, where is load applied; mesh generation, i.e. defining the finite elements; solving the set of partial differential equations; extracting the quantities of interest. Nowadays, integrated software solutions are available to perform all necessary steps in one

[18]The acronym FEM usually only describes the process of assembling and solving the partial differential equations. FEA describes the whole process of: setting up the geometry, mesh generation, calculation, analysing the results. However, FEM and FEA are often used interchangeable. We will use in the following text FEM.

program. We use *COMSOL Multiphysics 5.0* to perform all the FEM calculation presented in this thesis.

FEM Model of Indentation Experiment

We first build the geometry in COMSOL according to the indentation measurements (cf. Fig. 3.13b). This includes the sphere (r = 5 µm) and the sample (micro-cavity) (cf. Fig. 3.16). We do not need to include the AFM cantilever in the model because we know from the indentation profiles (cf. Fig. 3.15) by how much the sphere was indented into the sample. The sphere is modelled as a rigid material, which can not deform but only change its position as a whole, to simplify the model for faster calculation and better convergence. This is a good approximation since the glass bead we used as indenter has a Young's modulus approximately six orders of magnitudes higher than the samples. The mesh of the sphere has to be fine solely at the contact region to reproduce the curvature of the sphere, but can be coarser in other regions since no deformation or stress is allowed anyway in the rigid sphere (cf. Fig. 3.16c).

Our results in Fig. 3.14 indicate that the micro-cavities have an additional stiff layer on top of the elastomer. We therefore model the micro-cavity as a two layer system with an 8 µm elastomer layer and an additional 50 nm thick layer on top of the elastomer (later referred to as *stiff layer*)[19]. The contact between the stiff layer and the bulk is a tied contact. This means that the adjacent elements in the stiff layer and the bulk will always share one boundary and cannot slide against each other or penetrate the other layer. This is reasonable since we expect a tight bond between elastomer, SiO_2, and gold.

The contact between rigid sphere and stiff layer is set up such that it allows sliding between the two domains, neglects friction, and does not allow penetration of the sphere into the stiff layer[20]. In all simulations we prescribed the displacement of the sphere in negative z-direction (downwards) into the sample rather than assuming a force with which the sphere is indented. This improves convergence of the problem, and hence, speeds up

[19] We will explain why we use this value of 50 nm further down in the text.
[20] In COMSOL the *Augmented Lagrangian* algorithm is used to model the contact.

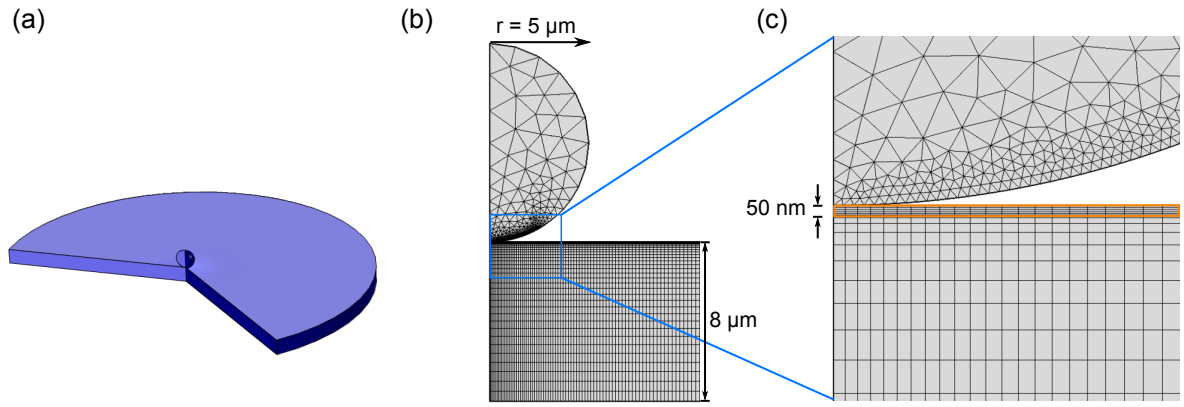

Figure 3.16: COMSOL model to describe indentation measurements. (a) Overview of 3D geometry. (b) Mesh of sphere and micro-cavity. (c) Close-up of contact between sphere and micro-cavity. Thin stiff layer highlighted in orange.

the calculation. The bottom surface of the elastomer is fixed in space, this is needed to constrain the problem and is similar to the experiment. We did not apply any constrains to the top boundary, and the right hand side boundary (where the edge is) of the elastomer and stiff layer. We assume a length of 100 µm from the point of maximum indentation to either side. This is sufficient since the indentation profile is close to 0 nm at a distance of 100 µm.

The geometry in the experiment has a rotational symmetry (cf. Fig. 3.16a). This can be utilised by COMSOL with additional boundary conditions to reduce memory cost and computation time. Figure 3.16b shows the geometry and mesh we use for the elastomer and the stiff layer in the COMSOL model for one plane of symmetry. We chose a mesh with increasing element sizes from the contact region to the boundaries of the elastomer. This ensures that the elements are small enough (<50 nm) at the region of large indentation gradients and we do not see significant changes in our results for element densities with a factor of ten higher or lower (data not shown).

Simulation with the same Young's Modulus for Stiff Layer and Bulk ($E_{El} = E_{SL}$)

First, we run the simulation with no stiff layer on top of the elastomer to compare the expected indentation profile for unoxidised elastomer with the indentation profile we measured for the micro-cavity. Note, we did not measure the indentation profile for the pristine elastomer sample because the refractive index contrast between elastomer and air is too

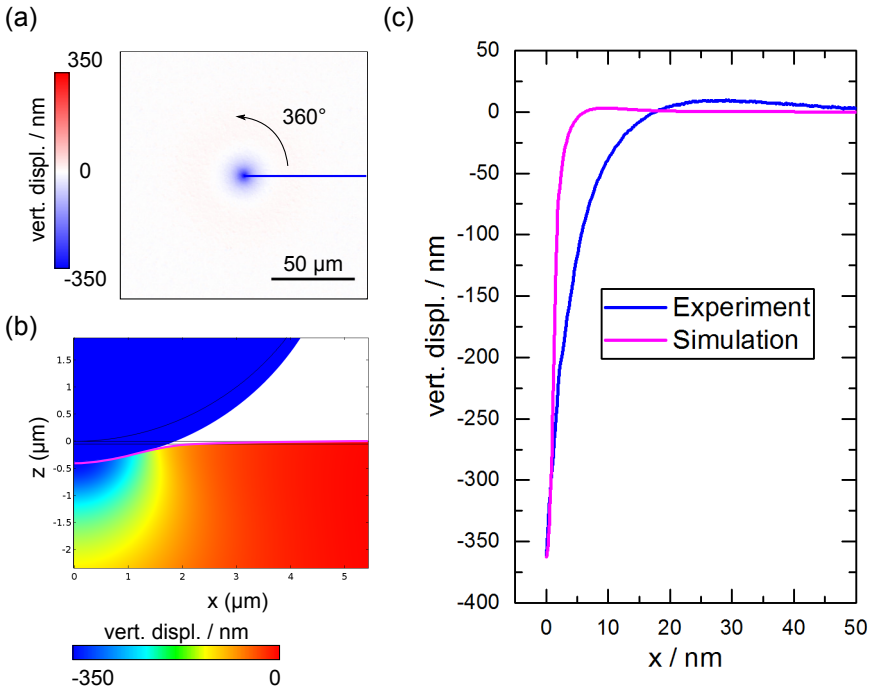

Figure 3.17: Comparison of simulated and experimentally obtained indentation profiles. (a) Displacement map with indicated indentation profile (blue line). Profile was obtained by taking the average over 360° around the maximum indentation. (b) Vertical displacement obtained by COMOSL simulation. Peak indentation depth (362 nm) was taken from the experimentally obtained indentation profile. Indentation profile at elastomer surface is highlighted in magenta. The black lines indicate the starting position of sphere and sample. (c) Experimentally obtained indentation profile for full micro-cavity (blue) and simulated indentation profile (magenta, as in (b)).

low to yield a meaningful ERISM signal. We keep the stiff layer in the simulation but assume the same Young's modulus as for the bulk ($E_{\mathrm{El}} = E_{\mathrm{SL}}$), i.e. the elastomer thickness is now 8.005 µm. We assume $E_{\mathrm{El}} = 450$ Pa and a Poisson's ratio of 0.49. Then, we prescribe the position of the sphere with the maximum indentation depths d_{max} (cf. Fig. 3.15 and Tab. 3.2) for each applied force in the AFM measurements, e.g. 362 nm for 10 nN. From the simulation we can then extract the simulated indentation profile of the top boundary (surface) (cf. Fig. 3.17b). Both profiles, measured with ERISM and simulated with COMSOL, are compared in Fig. 3.17c. It is apparent that the profiles are extremely different. The simulated profile (magenta line) is much narrower and does not describe the experimental data (blue line).

Changing the Young's modulus of the bulk material can not lead to an improvement of the fit. Although this would increase or decrease the force required to deform the substrate, it

does not change the indentation profile itself[21]. This is expected since the coupling strength between each element in the elastomer is still the same. Therefore, although the force required to achieve the same indentation depth changes for different Young's moduli, the indentation profile does not.

Although in the COMSOL model we move the sphere by a given value (e.g. d_{max} = 362 nm) into the sample, we can evaluate the force needed to achieve this translation from the simulation results. (Once COMSOL finds a solution for a certain indentation depth, the system is in equilibrium. This means, the sum of the force with which the elastomer pushes against to bottom boundary, which is fixed, and the force with which the sphere has to be indented into the multilayer structure has to be zero.) We will call the reaction force at the sphere RF_z in the following. Because the simulated indentation profile does not change by changing E_{El}, we can easily fit E_{El} in COMSOL such that the reaction force at the sphere equals the nominal value of 10 nN. This approach (performing FEM simulations) is equal or even superior to fitting a corrected the Hertz model to AFM force-distance curves. FEM simulations are often used as a reference to verify new analytical or numerical solutions which offer lower computational cost than FEM. Following this method, we get E_{El} = 12 kPa. As we expected, this sample was stiffer than the sample we investigated previously (cf. Fig. 3.14).

Figure 3.17c shows clearly that we overestimate the Young's modulus of the elastomer because the indentation profile for which we got E_{El} = 12 kPa is much narrower (magenta line) than what we measure in the experiment (blue line). We hypothesise therefore that a stiff layer on top of the elastomer broadens the indentation profile when the sample is under load. We therefore expect the actual E_{El} to be significantly smaller than 12 kPa. In the next sections we will test this hypothesis and vary the Young's modulus of the stiff layer E_{SL} to fit the simulated indentation profile to the experimentally obtained profile, whilst changing E_{El} such that RF_z equals the nominal forces we applied in the AFM experiment.

[21] We checked this in COMSOL by changing the Young's modulus and obtain identical indentation profiles.

COMSOL Simulation with $E_{El} \ll E_{SL}$

In the next step we added in our model the stiff layer on top of the elastomer and ran the simulation for different Young's moduli of the stiff layer. From now on we assume $E_{EL} = 350\,\text{Pa}$[22]. Figure 3.18 shows how the indentation profile changes for different E_{SL}. Although the indentation profile is broadened and therefore agrees somewhat better with the experimentally observed profile than the simulation without the stiff layer, none of the profiles has a shape that matches the experimental data. One can distinguish two main regions in the profiles. First, the initial slope of the profile from the centre of indentation, e.g. approximately $x = 0\,\mu\text{m}$ to $x = 10\,\mu\text{m}$ in Fig. 3.18. Second, the rest of the profile range where the slope decreases and the profile approaches 0 nm. It appears that one could potentially fit individual regions with one E_{SL} but not both regions with the same E_{SL}.

In addition, we vary the thickness of the stiff layer in the simulation and find that the same indentation profile (simulated) can be reproduced with multiple combinations of stiff layer thickness and E_{SL} (data not shown). This means that for the shape of the indentation profile mainly the difference in effective stiffness between elastomer and stiff layer is important. If we choose the stiff layer to be thinner, we can compensate this by increasing E_{SL}. Therefore, we chose 50 nm as thickness for the stiff layer because it has to be more than the 15 nm of deposited gold, but is likely not to be much thicker because the Young's modulus is expected to be in the gigapascal range (Young's Modulus for gold is 79 GPa and approximately 70 GPa for SiO_2). Consequently, even by changing the thickness of the stiff layer in our simulation we cannot fit the measured indentation profiles.

In summary, we conclude that the stiff layer can not be modelled as an isotropic linear elastic material but changes its Young's modulus depending on the strain. In other words, we will have to assume a nonlinear material. The difference between linear and non-linear materials is illustrated schematically in Fig. 3.19: An isotropic linear elastic material does not change its Young's modulus when the strain increases. However, the characteristic of a nonlinear elastic material is that the Young's modulus changes for different strains.

[22] This value for E_{EL} will be the correct one as we will see further down in the text. Using this value already here will make it easier to visualise the differences between the indentation profile for E_{SL} = constant (this section) and a strain dependent Young's modulus (next section).

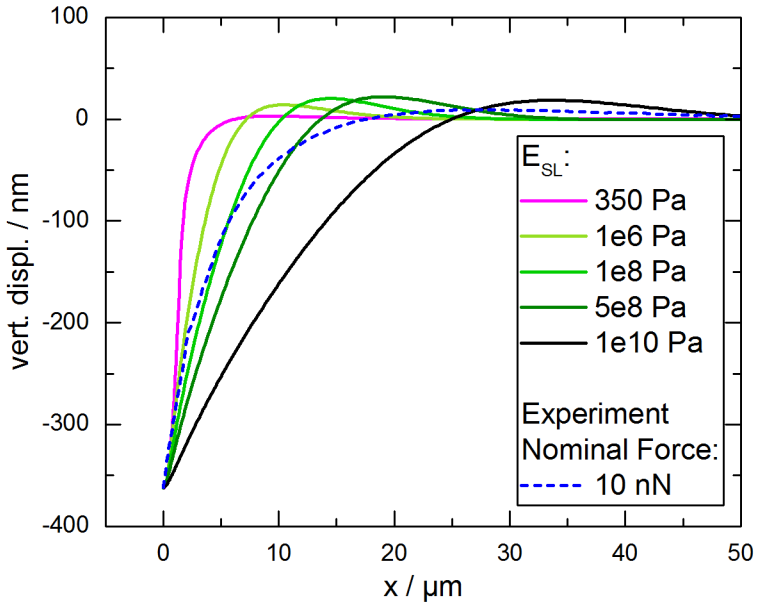

Figure 3.18: COMSOL simulation of indentation profiles for different Young's moduli E_{SL} of the stiff layer . For comparison the experimentally obtained profile (dashed blue line) and the simulated profile without stiff layer (magenta line) are shown as well.

Examples are for instance: strain hardening (increasing E for increasing ε) or the reverse, strain softening materials (decreasing E for increasing ε). The rupture of a material for higher strains could (depending on the material) be visible in the stress-strain-curve as a negative gradient.

COMSOL Model with Strain Dependent Young's Modulus $E_{SL}(\varepsilon)$

It is possible to implement isotropic nonlinear elastic materials (e.g. hyperelastic materials) in COMSOL. However, the required additional software package was not available at the time of performing this study and finding the right material properties is challenging. Furthermore, modelling the contact between sphere and the stiff layer becomes even more complicated if the strain and the strain dependent Young's modulus have to be evaluated in the same simulation (too many free parameters). To circumvent this problem, we developed an approach to estimate the strain dependent Young's modulus of the stiff layer from the experimentally obtained indentation profiles prior to the FEM simulation.

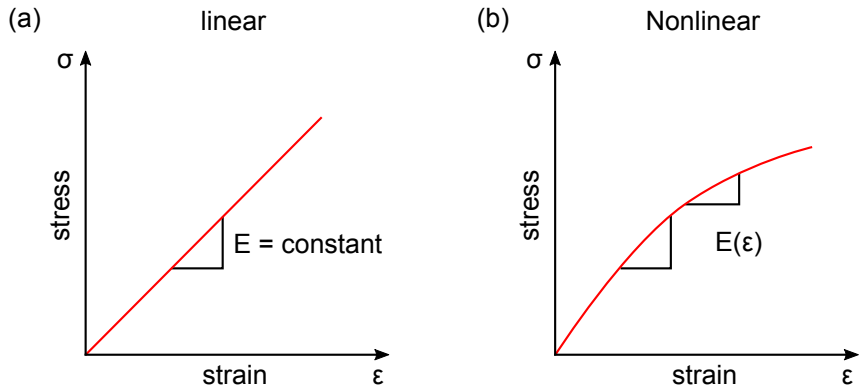

Figure 3.19: Schematic stress-strain curves for (a) an isotropic linear elastic material and (b) an isotropic nonlinear elastic material.

In order to develop a strain dependent model for the stiff layer we need to find a quantity which describes the strain in the stiff layer. We can not use the displacement measured with ERISM because this only describes the strain of the elastomer in vertical direction, but not the strain of the stiff layer in lateral direction[23]. However, the path length between two points on the micro-cavity surface is longer if the material is deformed by an indenter, i.e. any curved line connecting two points is longer than a straight line. Therefore, the surface is stretched in lateral direction whilst under load. The gradient of the indentation profile is thus an indicator for how much the surface is curved (stretched) at each point. We use the gradient $G(x) = \frac{d(\text{vert. displ.})}{dx}$ as a starting point for finding a function which describes how E_{SL} changes in dependence of the distance (i.e. in dependence of the gradient or strain) from the indentation centre . The indentation profiles and corresponding gradients are shown in Fig. 3.15 and Fig. 3.20a.

Judging from the difference between the experimental indentation profiles and the simulated profiles (E_{SL} = constant) in Fig. 3.18, we can make a guess that E_{SL} needs to be smallest at the centre of indentation and has to increase with distance from the centre. Except at the very centre, the gradients in Fig. 3.20a decrease with distance from the centre. We therefore search for a function which inverses this behaviour. A simple function which

[23] We assume that there will be nearly no compression of the stiff layer in vertical direction because it is likely to be more than five orders of magnitude stiffer then the elastomer.

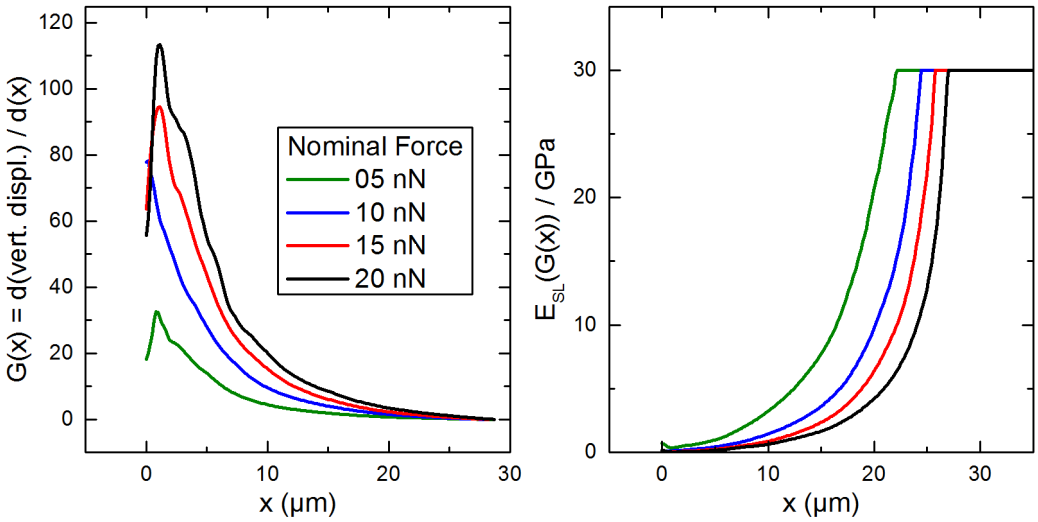

Figure 3.20: (a) Gradients derived from the experimentally obtained indentation profiles in Fig. 3.15. (b) Strain dependent Young's moduli derived from gradients using Eq. 3.7 with $A = 1.5 \times 10^9$ Pa, $B = -1 \times 10^8$ Pa, and $E_{\mathrm{El}} = 350$ Pa.

does this is:

$$E_{\mathrm{SL}}(x) = \frac{A}{G(x)} + B. \tag{3.7}$$

Here, $G(x)$ is the gradient and A and B are parameters which have to be determined by comparing simulation and experiment.

We manually fit A and B by comparing simulation and experiment for the 10 nN dataset (corresponding to $d_{\mathrm{max}} = 362$ nm). Whilst adjusting A and B, we monitor the reaction force RF_{z} at the sphere and vary E_{El} such that $RF_{\mathrm{z}} = 10$ nN. We find that we can describe the experimental data well with $A = 1.5 \times 10^9$ Pa, $B = -1 \times 10^8$ Pa, and $E_{\mathrm{El}} = 350$ Pa. We then use the same values for A and B to calculate $E_{\mathrm{SL}}(G(x))$ from the experimentally obtained indentation profiles for 5 nN, 15 nN, and 20 nN (cf. Fig. 3.20b) to simulate the profiles for each force (cf. Fig. 3.21). Our results show that we can describe all indentation profiles relatively well using the same parameters A and B for the gradient dependent Young's modulus $E_{\mathrm{SL}}(G(x))$. Simultaneously, all four reaction forces are in good agreement with the nominal force values (cf. Tab.3.2). By contrast, simulations with a constant E_{SL} describe all datasets less well than simulations assuming $E_{\mathrm{SL}}(G(x))$ with the deviation being largest for the larger forces (green lines versus blue dashed lines in Fig. 3.21).

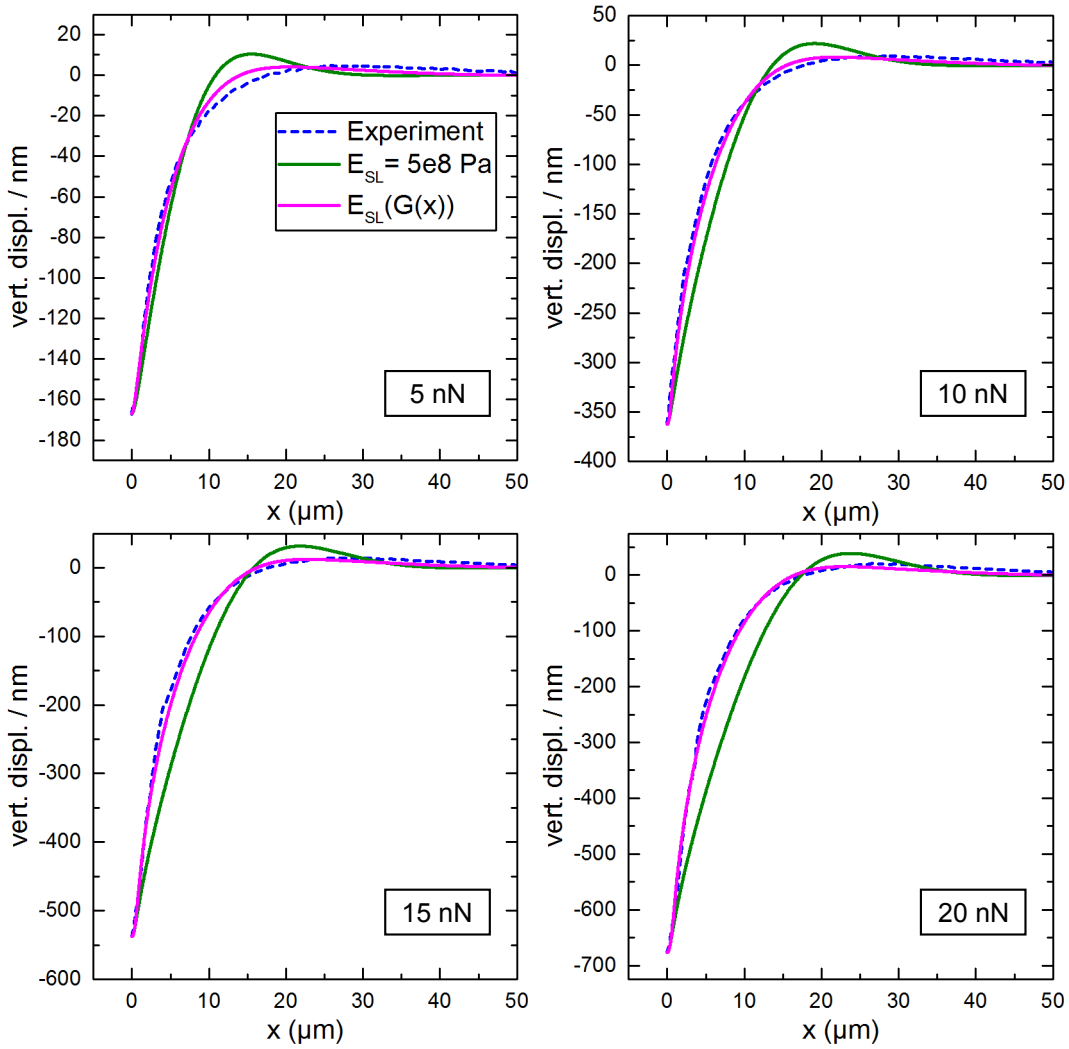

Figure 3.21: Comparison of indentation profiles: experimentally obtained (blue, dashed), simulation with constant Young's modulus 0.5 GPa (green), and simulation with strain dependent Young's modulus (cf. Fig. 3.20 magenta).

When using $E_{SL}(G(x))$ instead of a constant E_{SL} the remaining deviation between simulation and experiment for the 5 nN indentation force are largest. This is apparent in the shape of the profiles (cf. Fig.3.21a) but also in the reaction forces (cf. Tab.3.2) which differ by over 30%. This might be an indication for the limits of our approach to fit the Young's modulus of the stiff layer with a gradient dependent function as opposed to fitting an established hyperelastic material model, e.g. Neo-Hookean or Mooney-Rivlin.

In conclusion, we showed that the micro-cavities we use as substrates for ERISM measurements can be modelled as a two layer system comprised of a isotropic linear elastic bulk material (elastomer) and an isotropic hyperelastic thin and stiff layer. Although not done in this thesis, it should be possible to describe the stiff layer with established hyperelastic material models. Next, we will investigate if we can calculate the applied (nominal) forces from the indentation profiles (experiment), and which role the stiff layer plays in these calculations.

Force Calculation by Evaluating the Stress

So far we only evaluated the reaction forces at the indenting sphere. However, this procedure is only possible for these particular simulations, i.e. when a sphere is part of the model. If we want to calculate forces from ERISM displacement maps, we need to calculate the stress and then evaluate the forces by integrating the stress over an area.

First, we perform this analysis for the COMSOL simulation of the indentation profile, using the $E_{SL}(G(x))$ approach developed in the previous section. The integral of the vertical component of the *Cauchy Stress Tensor* σ_z over any plane parallel to the surface of the elastomer should yield the total force exerted on the elastomer, i.e. the reaction force at the sphere. We test this and integrate σ_z at a plane A_1 which is 100 nm below the surface, to calculate the situation in the elastomer and not the stiff layer. The plane extends from $x = 0\,\mu m$ to $x = 100\,\mu m$[24] as illustrated in Fig. 3.22. The values for $\int \sigma_z dA_1$ are summarised in Tab. 3.2 and are in very good agreement with RF_z.

[24] Note, this is with respect to the COMSOL model which has a rotational symmetry around $x = 0\,\mu m$, i.e. the area is covered by a circle with a radius of 100 µm.

Although this approach yields the right results, the integration area is rather large compared to what is feasible in an experiment. This has two reasons. First, experimentally obtained data will have some noise and even nanometre deviations could add up to a significant error in force if integrated over a large area. Second, for such a large integration area the lateral force resolution (meaning two point forces next to each other) would decrease dramatically since point forces which are even 50 µm apart would be in the same integration area. We therefore perform the same integration but for a smaller integration area A_2 which covers the area until the indentation profiles pass zero (cf. Fig.3.22), this is at $x = 18\,\mu m$ for all four profile. While this yields to approximately 10% smaller forces (cf. Tab. 3.2) compared to results with integration area A_1, the values still give a good indication of the applied force.

Finally, following the same approach (and using integration area A_2), we calculate the forces from the experimentally obtained profiles (cf. Tab. 3.2). The calculated values are almost in perfect agreement with the nominal values. It should be pointed out that these final calculations do not involve any simulations with a sphere, but are solely obtained by applying the indentation profiles measured with ERISM (cf. Fig. 3.15) to the COMSOL model without stiff layer and with $E_{EL} = 350\,Pa$. This shows that, although it was important to fit $E_{SL}(G(x))$ to understand the mechanical difference between pristine elastomer samples and full micro-cavities and to fit $E_{EL} = 350\,Pa$[25], we do not need to include the stiff layer (and the associated strain dependent Young's modulus) in the FEM model when we analyse experimental data of cells, i.e., a simple FEM model of the bulk material (elastomer) is sufficient to calculate the force from the measured data (cf. right column in Tab. 3.2). This analysis gives us direct access to the vertical stress cells exert to the substrate and the possibility to integrate the stress in order to calculate the applied forces.

[25] We appreciate that there is a difference of approximately 30% between the fitted value of $E_{El} = 350\,Pa$ and $E_{El} = 460\,Pa$, a value stated earlier in this chapter and which was measured with rheology by collaborators. However, these rheology measurements were performed in a different lab at another university, therefore, this deviation might be a result of slightly different sample preparation, e.g. maybe in one of the experiments the two elastomer components were less well mixed than in the other.

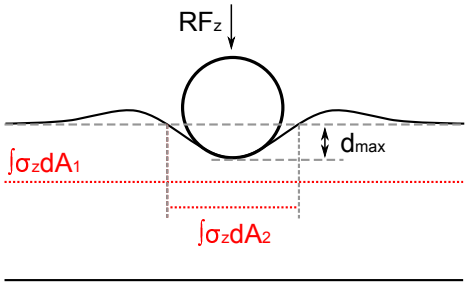

Figure 3.22: Schematic which shows where reaction forces and stress were evaluated in the COMSOL model. The red dotted lines are at the same height in COMSOL and only vertically shifted in this schematic for better illustration.

Table 3.2: Summary of FEM force calculation of AFM data. From left to right: Nominal force applied to the AFM cantilever and corresponding maximum indentation. Simulation of reaction force for a sphere indenting with the maximum indentation (second column) into substrates with $E_{SL} = 0.5\,\text{GPa}$ and $E_{SL} = E_{SL}(G(x))$. Force calculation by integrating σ_z over A_1 or A_2 when simulated indentation profiles are applied to the structure (as described in text). Similar calculation for the experimentally obtained indentation profiles.

Nominal Force	Maximum Indentation d_{max}	Indentation of sphere by d_{max} into sample				Exp. Profiles
		$E_{SL} = 0.5$ GPa	$E_{SL} = E_{SL}(G(x))$			$E_{SL} = 350$ Pa
		RFz	RFz	$\int \sigma_z dA_1$	$\int \sigma_z dA_2$	$\int \sigma_z dA_2$
[nN]	[nm]	[nN]				
5	167	2.3	3.6	3.6	3.4	4.3
10	362	9.7	10.0	10.0	9.3	9.6
15	537	21.3	16.5	16.6	14.7	14.9
20	676	33.9	20.1	20.2	18.3	19.7

3.5.3 Exemplary Stress Calculation for an ERISM Measurement

We now calculate the vertical stress for the 3t3 cells for which we calculated the vertical displacement in Section 3.4.4 (cf. Fig. 3.23a).

We cannot use the same rotationally symmetric geometry in COMSOL as we described in the previous section, by contrast, we need a 3D representation of the field of view which we investigated on the micro-cavity. We showed in the previous sections that we do not need to consider a stiff layer on top of the elastomer, hence, the geometry here is a single cuboid of elastomer (cf. Fig. 3.23b) with $E = 350\,\mathrm{Pa}$ and $\nu = 0.49$. The average thickness in this example is 8350 nm (cf. Fig 3.8) and we use this value as the thickness for our model. The lateral dimensions are chosen according to the image size, i.e. $181\,\mu\mathrm{m} \times 166\,\mu\mathrm{m}$.

We use a regular mesh of hexahedral elements. The element size in lateral direction is 0.9 µm. In vertical direction, the geometry is meshed such that there are two planes of elements (cf. Fig. 3.23b). In the plane close to the top surface, the elements are 1.67 µm long and in the plane below they are 6.68 µm (cf. Fig. 3.23). This distribution allows us to divide the geometry into only two slices in vertical direction which saves computation time. We tested the COMSOL model with smaller element sizes, lateral and vertical, at positions where the largest vertical displacements occur and found that the stress does not change by more than 5% when we reduce the element size by a factor of two. This is a good indicator that the solution has converged and does not depend on the mesh size any more[89]. We could choose larger element sizes at areas where the cells do not apply stress to increase calculation speed, however, the advantage of a regular mesh is that we can use the same mesh for different displacement maps. This allows the automatised computation of the stress field for multiple frames as opposed to manually adjusting the mesh for each time frame. In addition, to investigate cells which exert higher local stress and show smaller features, one could possibly change the local element size either depending on the vertical displacement or the gradient of the local displacement field.

Similar to our previous COMSOL model, the geometry is fixed at the bottom (boundary condition). We then use the map of the vertical displacement values and apply these values

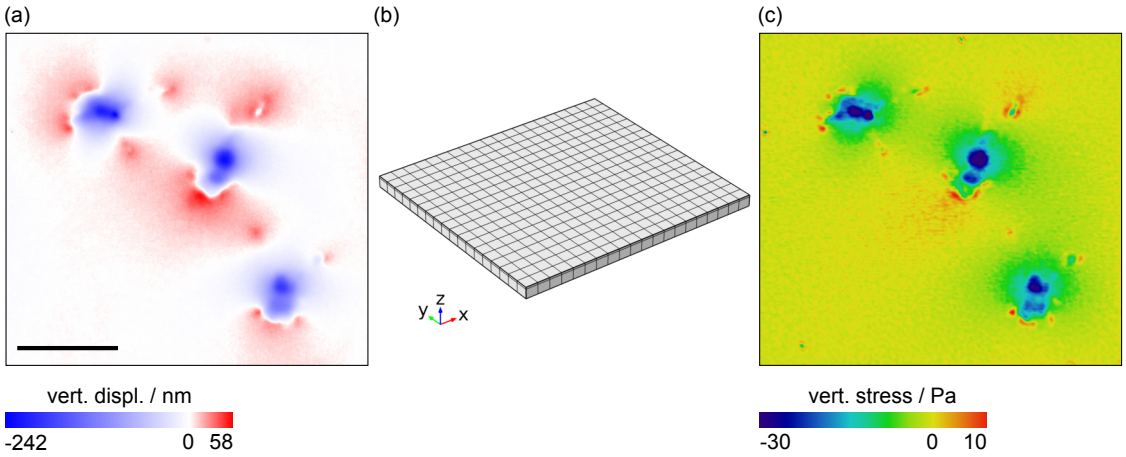

Figure 3.23: COMSOL calculation of vertical stress from vertical displacement. (a) Vertical displacement exerted by 3t3 cells as described in Section 3.4.4. Scale bar, 50 µm. (b) Mesh which was used in the COMSOL simulations, in this figure, the element size is increased for clarity, the real element size in lateral direction is below 1 µm. (c) Result of the COMSOL simulation, vertical stress.

to the top surface of the geometry. In the simulation, COMSOL calculates how the rest of the geometry is deformed and the value of the stress at each pixel.

We find that the 3t3 cells apply vertical stress in the range of 12 Pa to −60 Pa. It is difficult to compare our values for the vertical stress 3t3 cells exert to the results of other groups because often the conditions for each experiment are different, e.g. substrate coating, cell medium, and substrate stiffness. However, in collaboration with the group of Kristian Franze (Cambridge), we compared the vertical stress 3t3 cells apply to an ERISM micro-cavity with the lateral stress the same type of cells (same batch of 3t3 cells) apply to a hydrogel with similar stiffness (4 kPa). The lateral stress was measured using standard 2D TFM which is routinely used in this lab. We found that vertical and lateral stress are similar in both experiments[77].

Force Balance

The total force applied by one cell in vertical direction should be zero, otherwise the system would not be in equilibrium and the cell would either move into the substrate or detach from it. Therefore, investigating whether pushing and pulling balances out in the results obtained with ERISM is an important step to ensure the validity of ERISM results.

This calculation should be done on a dataset with a single cell (as opposed to the previous example) to avoid that forces applied by other cells influence the force balance. We use a dataset from a single microglia cell (cf. Section 4.3.4), a phase-contrast image of this cell is shown in Fig. 3.24a. The vertical stress is calculated as described in the previous paragraphs. To calculate the force we integrate the stress over the whole image area. We perform the integration for the stress map as calculated with COMSOL (cf. Fig.3.24b) and for positive and negative stress values (cf. Fig.3.24 (c) and (d)). We find that the cell pushes with approximately 3.5 nN and pulls with approximately 3.1 nN. In this example the pushing force is estimated to be 12% higher than the pulling force. We find a similar deviation consistently in different examples (data not shown) and attribute this effect to the difficulty of integrating the pulling over the full area. The larger the integration area the more the calculation of the force is affected by small errors e.g. caused by the background correction. For example, even an offset below 1 nm will result in a large force if the integration area is very large. Thus, we restricted the integration area for the calculation of the force balance, however, this is likely to be the cause of the deviation between the pushing and pulling forces because the pushing is completely considered by this approach whereas the pulling is not. As described earlier we observed a similar effect when we calculated the values in Tab. 3.2.

In addition, to show that gravity can be neglected we estimate the force with which the cell would push into the substrate because of its weight. We make the following assumptions: cell volume estimated by a cube with 15 µm one side; cell density, 1060 $\mathrm{kg\,m^{-3}}$ (density of a HeLa cell [90]). Therefore, the weight of one cell is approximately 0.035 nN. In addition, we have to consider buoyancy because the cells are surrounded by cell medium. We assume the surrounding medium to be water which has a lower density than cell medium and subtract the buoyancy from the cell weight. This yields a total force (weight minus buoyancy)

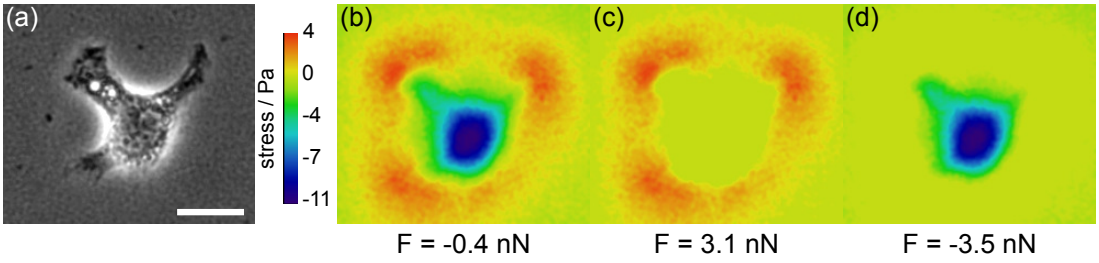

Figure 3.24: Evaluation of the force balance between pushing and pulling forces. (a) Phase-contrast image of the investigate microglia cell. (b) Vertical stress, pushing and pulling. (c) Vertical stress, only pulling. (d) Vertical stress, only pushing. Scale bar 20 µm. Force values below (b), (c), (d) were calculated by integrating the stress over the full image area.

of 0.002 nN which the cell applies to the substrate. We conclude that we do not need to consider the weight of the cell in the force balance as it is three orders of magnitude lower than what we estimate for the applied vertical forces.

3.5.4 Measurement of Lateral Forces with ERISM

We have successfully shown that we can apply vertical forces to an ERISM micro-cavity with an AFM and then measure these forces with ERISM. Cells also apply forces in lateral direction and we wondered if we can measure lateral forces with ERISM as well. We do not pattern the ERISM micro-cavities or introduce fluorescent beads like in TFM, although this combination might be possible in the future. Therefore, for now, we cannot track lateral deformations of the surface of the micro-cavity. Surprisingly, we observe substantial vertical displacements generated by biological structures which are very flat and therefore would not be expected to apply vertical forces. One example are axon growth cones which we observed when we were seeding primary neurons from mice on an ERISM micro-cavity (see Section 4.4). Growth cones are known to exert forces in the nanonewton regime, but they usually have a height below 1 µm which favours exertion of lateral forces over vertical forces[91, 92, 16, 93]. We therefore hypothesise that because ERISM can detect nanometre changes in cavity thickness, we possibly see twisting of the gold/SiO_2 top surface of the cavity. This motivated the following measurements on the mechanical response of ERISM micro-cavities to lateral forces.

For these experiments we fix the tip of an AFM cantilever (not with bead but with sharp tip) to the surface of a micro-cavity. Then, we move the cantilever in lateral direction using the piezo in the AFM scan head (to which the cantilever is attached). If the cantilever tip is fixed to the micro-cavity surface, a lateral force should be applied and we would see the response of the micro-cavity to this force with ERISM. In order to translate the applied lateral displacement to a lateral force we need to perform calibration measurements.

Introduction to Lateral Atomic-Force-Microscopy

In the previous chapter we described how one can apply or measure vertical forces with an AFM. The cantilever is bend up or down and the laser beam reflected at the end of the cantilever will be sent to another point on the detector. The change in detector voltage can then be converted into the displacement of the cantilever, and if the spring constant k_z of the cantilever is known, it is possible to calculate the force.

Measuring lateral forces works in a similar manner but comes with three main difficulties. First, the cantilever (rectangular) is stiffer in lateral direction (i.e. against torsion) compared to normal bending. This means the sensitivity is inherently lower for lateral forces. Second, a change in lateral direction of the tip might lead to an actual lateral displacement and a torsion of the cantilever at the same time. However, only the torsion will change the angle of the laser beam, therefore, only the torsional component of the force will be detected. Third, the lateral force distance calibration is much more difficult than for the vertical case: For the vertical calibration the cantilever is moved against a hard substrate with the z-piezo by a known distance. Then, the deflection of the cantilever has to be equal to the displacement with the z-piezo. Thus, the measured change in detector voltage can be correlated to a known cantilever deflection. However, inducing a twisting of the cantilever is much more challenging. There are various methods to measure the lateral sensitivity[94]. We follow an approach where the cantilever tip is moved against a hard edge to apply a known lateral displacement[95]. In addition to the general challenge of performing lateral force measurements, it is difficult to establish a tight contact between the ERISM micro-cavities and the cantilever tip. Given this challenges, the following section should be seen as a prove

of concept to exert lateral forces on an ERISM micro-cavity and as a way to investigate how sensitive these micro-cavities are to lateral forces.

Lateral and Torsional Spring Constant

A square shaped cantilever with a tip at the and can be deformed in three principle directions if a force is applied at its end. Following the coordinate system in Fig. 3.25a they are as follows. A force in z-direction leads to a bending up or downwards (cf. Fig. 3.13). This is what is used to image the height profile of a sample or measure/apply forces orthogonal to the sample plane. A similar deformation would occur if a force is applied at the tip in y-direction. This is usually not used because the deformation happens in the same direction as for forces in z-direction. A force in x-direction will lead to two different deformation patterns. First, the cantilever will bend in the xy-plane (cf. Fig. 3.25a). This would be the only lateral response if the force would be applied directly at the cantilever and not at the tip. However, if the force is applied at the tip, the tip acts as a lever and in addition to the lateral bending the cantilever experiences a torque around its long axis (cf. Fig. 3.25b), which induces a twist.

The reflected laser beam will only change its angle of reflection if the cantilever is deformed outside of the xy-plane. This means pure lateral bending (cf. Fig. 3.25a) does not lead to a change in detector signal. By contrast, a twisting of the cantilever around its long axis (cf. Fig. 3.25b) will change the position of the reflected beam perpendicular to what is observed for bending under a load in z-direction (normal deformation). Therefore, normal deformation and twisting can be distinguished if a photo-diode detector with four quadrants is used.

As mentioned above, a force acting in x-direction at the cantilever tip will induce a displacement Δx of the middle of the cantilever which is the sum of two components from pure lateral bending Δx_x and twisting Δx_ϕ (cf. Fig. 3.25a and (b)). We can replace the displacements with the product of the lateral acting force F_x and the spring constants for lateral bending k_x and for twisting k_ϕ:

$$\Delta x_x + \Delta x_\phi = \frac{1}{k_x} F_x + \frac{1}{k_\phi} F_x = (\frac{1}{k_\phi} + \frac{1}{k_x}) F_x = \frac{1}{k_{\text{lat}}} F_x. \tag{3.8}$$

If the dimensions of the cantilever and the material properties are known we can calculate the spring constants k_z (not needed here, but stated for comparison to the other two spring constants), k_x, k_ϕ and therefore the combined lateral spring constant k_{lat} [94]:

$$k_z = \frac{Ewt^3}{4L^3}, k_x = \frac{Ew^3t}{4L^3}, k_\phi = \frac{Gwt^3}{3H^2L}, k_{\text{lat}} = \frac{GEw^3t^3}{3LEH^2w^2 + 4GL^3t^2} \tag{3.9}$$

Here, L, w, and t are the length, width, and thickness of the cantilever, respectively (cf. Fig. 3.25a and b). H is the distance between the end of the cantilever tip and half the thickness of the cantilever (cf. Fig 3.25b and c). E and ν are the Young's modulus and Poisson's ratio of the cantilever material respectively. These two quantities can be expressed as the shear modulus $G = \frac{E}{2(1+\nu)}$.

In order to calculate the lateral displacement and force from a change in lateral detector voltage ΔV_ϕ we need to measure the sensitivity for twisting S_ϕ:

$$\Delta x_\phi = \frac{\Delta V_\phi}{S_\phi}, \Delta x_x = \frac{\Delta V_x}{S_x} \tag{3.10}$$

However, since the purely lateral bending does not lead to a change in angle of reflection we have $\Delta V_x = 0$. We can now write Eq. 3.8 with the sensitivities and the detector voltages:

$$\Delta x = \Delta x_x + \Delta x_\phi = \frac{\Delta V_x}{S_s} + \frac{\Delta V_\phi}{S_\phi}, \Delta V_x = 0 \tag{3.11}$$

$$\Delta x = \frac{\Delta V_\phi}{S_\phi} = \frac{F_x}{k_{\text{lat}}} \tag{3.12}$$

$$F_x = \frac{k_{\text{lat}} \Delta V_\phi}{S_\phi} \tag{3.13}$$

This means, that from a change in ΔV_ϕ we can calculate the force acting on the cantilever and sample surface if we know the sensitivity S_ϕ. Note, that we have to consider k_{lat} and not just k_ϕ.

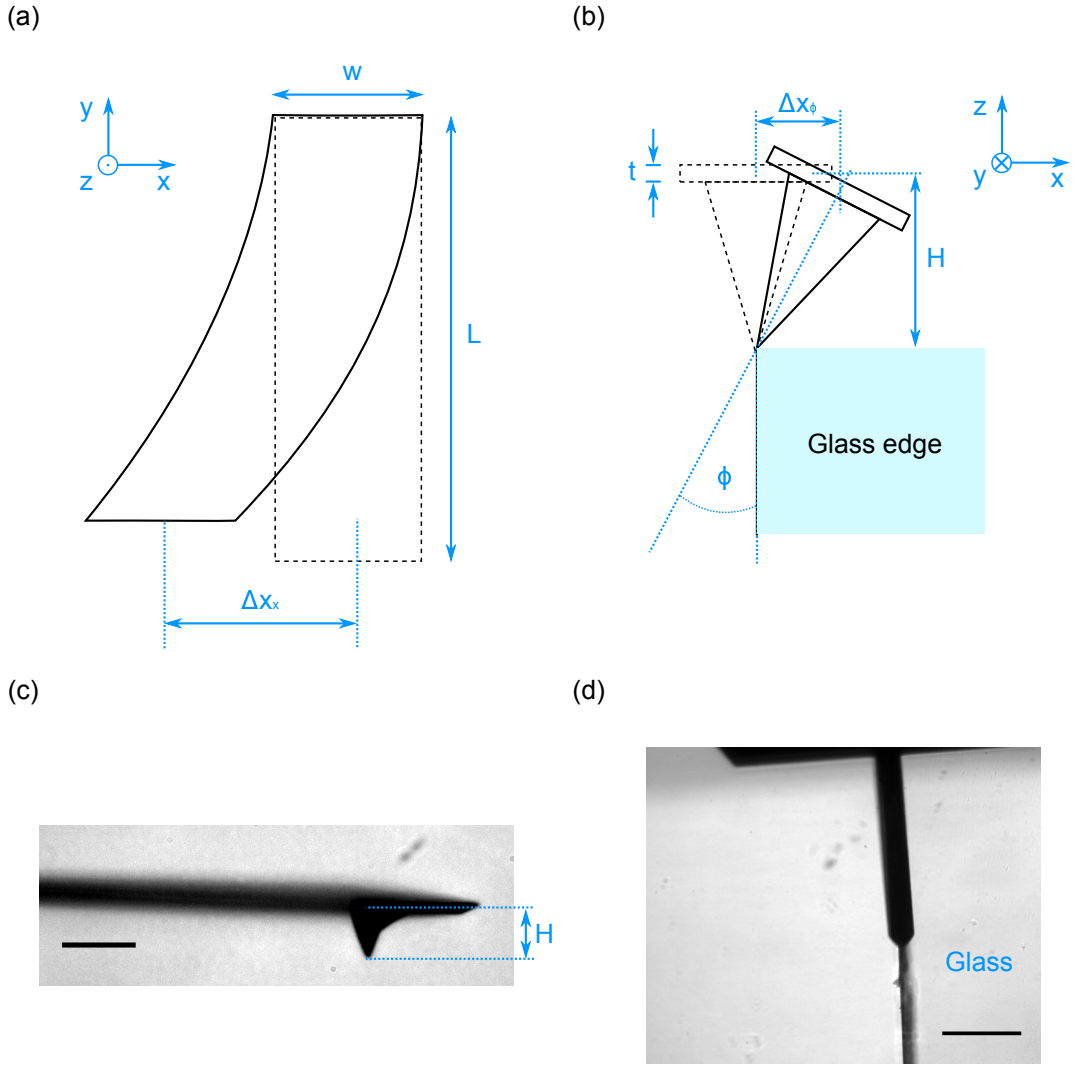

Figure 3.25: Dimensions and quantities of AFM cantilever for: (a) lateral bending in xy-plane; (b) torsion when moving against a glass edge. (c) Cantilever with tip. Scale bar 20 µm. (d) Cantilever at glass edge. Scale bar 200 µm.

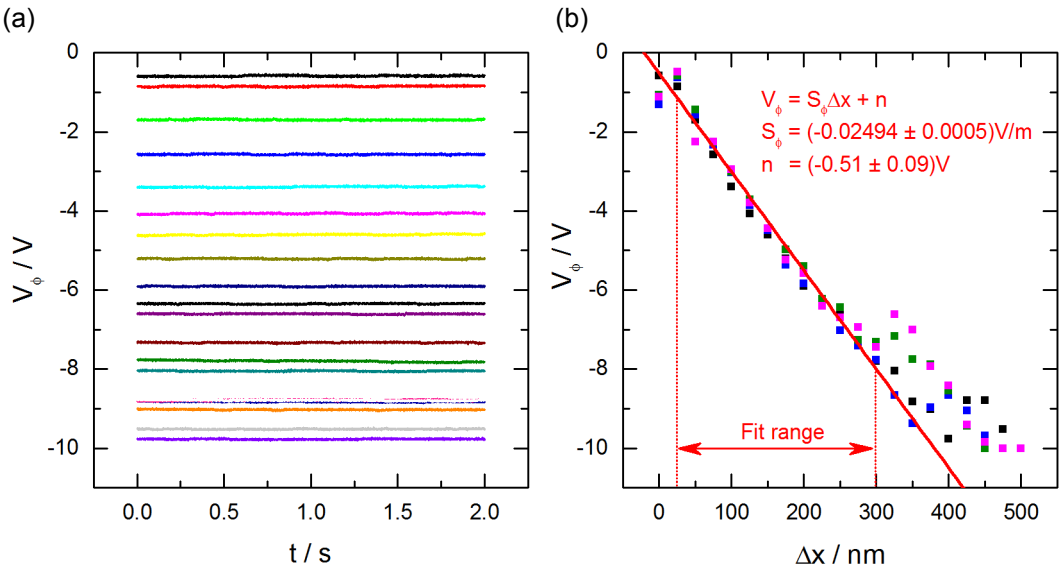

Figure 3.26: Datasets obtained as pictured in Fig. 3.25. (a) Lateral detector voltage V_ϕ over the 2 s pause at Δx intervals of 25 nm. The mean value of each line corresponds to one data point of the black dataset in (b). (b) Mean values of V_ϕ for different Δx for four repeated measurements. Red line represents linear fit over all four datasets to extract S_ϕ.

Calibration of the Lateral Sensitivity S_ϕ

We measure S_ϕ by applying different lateral displacements Δx to the cantilever tip and record V_ϕ for each step. We apply the lateral displacements by moving the cantilever tip with the AFM scan head piezo in 25 nm steps against a glass edge. The glass edge was created by breaking a 0.5 mm cover slip and fixing it on a glass slide. To ensure that the tip will in fact move against an edge and not against and upward a gradient, we brought the tip in contact with the cover slip and moved towards the edge. We essentially operated the AFM in imaging mode and searched for a position were the tip would fall down if at an edge. Once we found this position we moved the cantilever over the edge, moved it 100 nm down and moved it then in 25 nm steps against the edge. Each position was hold for 2 s to make sure the cantilever was in a stable twisted position. We performed this measurement four times to prove reproducibility of our results.

In Fig. 3.26a we show for one dataset (the black dots in Fig. 3.26b) V_ϕ for each lateral position over the course of the 2 s pause time. Apparently V_ϕ is very stable during the course of each measurements, we therefore calculate the mean value of each trace and plot the

resulting lateral detector voltage against the applied lateral displacement (cf. Fig. 3.26b). We can clearly observe a very reproducible and linear dependency between V_ϕ and Δx in the range 25–300 nm. For values smaller than 25 nm the tip might not yet be in contact with the glass edge. After 300 nm the tip probably starts slipping over the edge since the tip is a cone, which leads to less reproducible behaviour between V_ϕ and Δx. With this procedure we obtain the lateral sensitivity of the AFM and cantilever $S_\phi = (0.024\,94 \pm 0.000\,05)\,\mathrm{V\,nm^{-1}}$.

Applying Lateral Forces to ERISM Micro-Cavity

We now have all the quantities to bring the cantilever tip in contact with an ERISM micro-cavity, apply a lateral displacement, and calculate how big the lateral force was that acted on the micro-cavity to induce this displacement. At the same time we can measure the displacement of the micro-cavity surface in vertical direction with ERISM.

The main difficulty of this experiment is to fix the position of the cantilever tip on the micro-cavity surface. For the indentation measurements with glass beads we used a high salt concentration buffer to avoid electro static effects between bead and micro-cavity surface. The electrostatic attraction between tip and sample surface is what we utilise in this experiment to maintain a contact between sample and tip and to apply lateral displacements/forces without changing the lateral position of the tip on the sample. Although we did not see signs of the cantilever slipping for the data used in the following, this is not a well-controlled effect and in addition we observe that the micro-cavity surface is pulled upwards (towards the tip) by the electrostatic attraction. We balance the height of the tip such that we do not have any vertical deflection of the cantilever. Therefore, the shape of the indentation profile without any lateral displacements has the shape of a volcano, indentation in the middle of the tip, but going up at the outside (cf. Fig. 3.27 left images). Nevertheless, once we move the cantilever to the left, we indeed observe a change in the thickness maps (cf. Fig. 3.27). In addition to the displacement maps, we also plotted the interference images at 650 nm in Fig. 3.27 (top) to visualise how the interference pattern looks close to the tip and how the pattern changes with increasing lateral displacement.

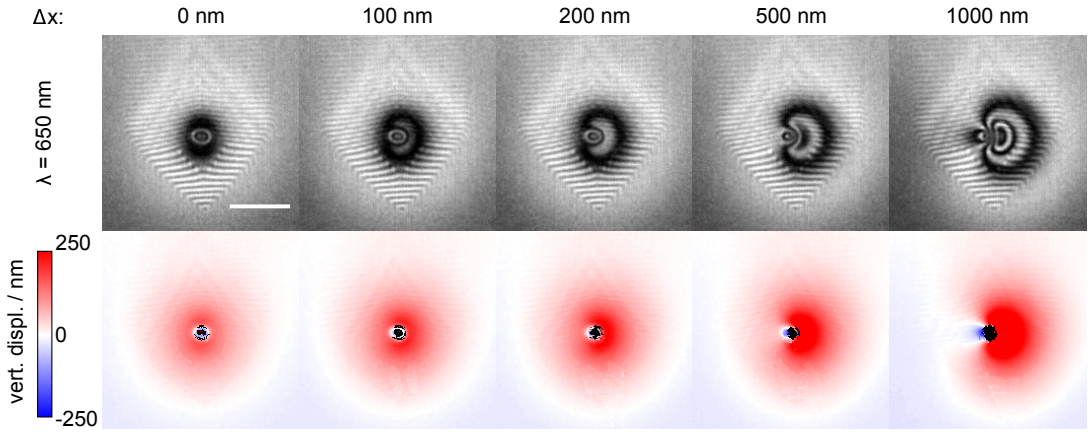

Figure 3.27: AFM tip in contact with ERISM micro-cavity. ERISM interference images at 650 nm (top) and vertical displacement maps (bottom) for different lateral displacements, ranging from 0–1000 nm.

We extracted the indentation profiles for each Δx along the axis of lateral displacement through the centre of indentation. We could not fit the micro-cavity thickness at the contact area of the tip, which we attribute to the very strong sample deformation in this region.

We observe that with increasing lateral displacement the right hand side of the indentation profiles gets higher and the left hand side lower. We then extract the vertical displacements at the position where the indentation profile has its maxima for $\Delta x = 0\,\text{nm}$. We also recorded V_ϕ for each Δx and then plotted the vertical displacements for right and left side of the profiles over V_ϕ (cf. Fig. 3.28b). We can fit this linear relation and extract the slopes. The slopes are a measure for how much the micro-cavity deforms (vert. displ.) for a certain change in detector voltage. The slope obtained by fitting the maxima of the indentation profiles is significantly higher (in absolute value) than the slope obtained when fitting the minima. In the following we consider the maxima tracking the minimum indentation accurately proved more difficult because of non-fitted pixels at the side of the minimum.

With these slopes and S_ϕ we can now correlate the forces we applied by moving the cantilever in lateral direction and how this translates into vertical displacements. We define the sensitivity of vertical displacements detected with ERISM to lateral forces as:

$$S_x^{\text{ERISM}} = \frac{\text{vert. displ.}}{F_x} = \frac{\text{vert. displ.}\, S_\phi}{k_{\text{lat}} \Delta V} = 4.7\,\text{nm}\,\text{nN}^{-1} \tag{3.14}$$

Here we used the following values to calculate k_{lat}: $t = 2\,\mu\text{m}$, $H = 13\,\mu\text{m} + \frac{t}{2} = 14\,\mu\text{m}$, $L = 450\,\mu\text{m}$, $w = 50\,\mu\text{m}$, $E = 170\,\text{GPa}$[96], $\nu = 0.27$[96]. The values for the cantilever dimensions L, w, t are the nominal values for this cantilever provided by the manufacturer[26]. H was measured from the image in Fig. 3.25c, E and ν are the Young's modulus and Poisson's ratio for silicone.

We will see in Section 4.4 that we can indeed observe the lateral force exerted by growth cones from neurons of dorsal root ganglia (on a micro-cavity with comparable stiffness). We observe deformations of around 10 nm. Considering our results in this chapter, this would correlate to a lateral force of approximately 2 nN. This is comparable to what Koch et al. measured with TFM for growth cones of dorsal root ganglia (the authors report values between 0.5–1.5 nN).

We conclude that we can in fact measure lateral forces with ERISM and we demonstrated how to perform the calibration to link vertical displacement measured with ERISM to lateral force. However, it should be noted that the value for the lateral force sensitivity of ERISM ($S_{\text{ERISM}} = 4.7\,\text{nm}\,\text{N}^{-1}$) we estimated here is likely to have a large uncertainty due to the challenges involved in measuring lateral forces with an AFM as described in the beginning of this section. We appreciate that the calibration of the micro-cavities should be repeated with a more controlled contact between surface and tip. This problem could be addressed by different methods. The electro-static attraction could be controlled by performing the measurements in water with the ability to control the salt concentration. It is also possible to use special cantilevers to directly apply a voltage to the tip. If a high enough salt concentration is used, the electro-static attraction can be diminished completely, and then the tip and micro-cavity surface could be functionalised such that a tight contact is established. Furthermore, we suggest to use a different cantilever which is more sensitive to twisting. The thickness t has a major influence on this and cantilevers with thicknesses below 2 µm are available.

[26] The cantilever used for this measurement is a ContAl-G from Budgetsensors.

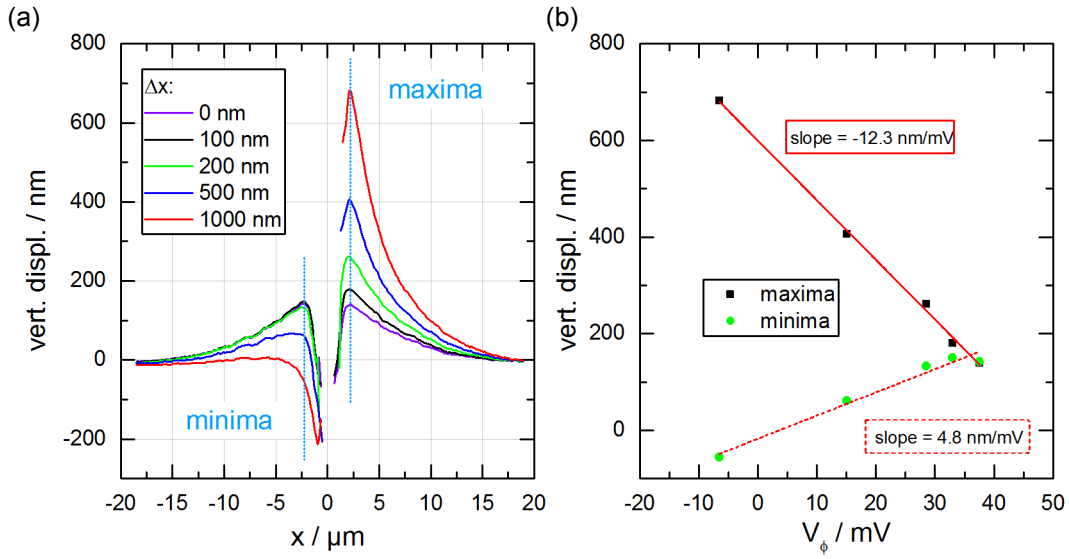

Figure 3.28: (a) Indentation profiles extracted from the displacement maps in Fig. 3.27. (b) Vertical displacement at maxima and minima position of the profiles against lateral detector voltage for each lateral position. Both datasets were fitted with a linear function.

Chapter 4

Application of ERISM to Neural Cells

4.1 Neural Cells

The following description of the cells of the nervous system is based on the book "Neuroscience" by Purves et al.[97].

The nervous system of the human is divided into the central nervous system (CNS) formed by the brain and the spinal cord, and the peripheral nervous system (PNS) which connects limbs and organs to the CNS (cf. Fig.4.1a). The cells of the central nervous system in the human body can be classified in two main groups: neurons and glial cells. Whereas the neurons are considered to be the cells which actually do the "thinking" — meaning that they transmit and receive electrical and chemical signals — the glial cells have a more supporting role in providing structural support, nutritions, and digestion of cell debris[97].

4.1.1 Neurons

Neurons are cells with the capability to send and receive electrical and chemical signals in order to control muscle contraction, receive and interpret external stimuli, and are the key-player in complex decision making. Neurons have a cell body, usually short processes called *dendrites* which receive signals and one or two longer processes called *axons* (cf. Fig. 4.2). Axons and dendrites of different cells are connected via *synapses* — formations which

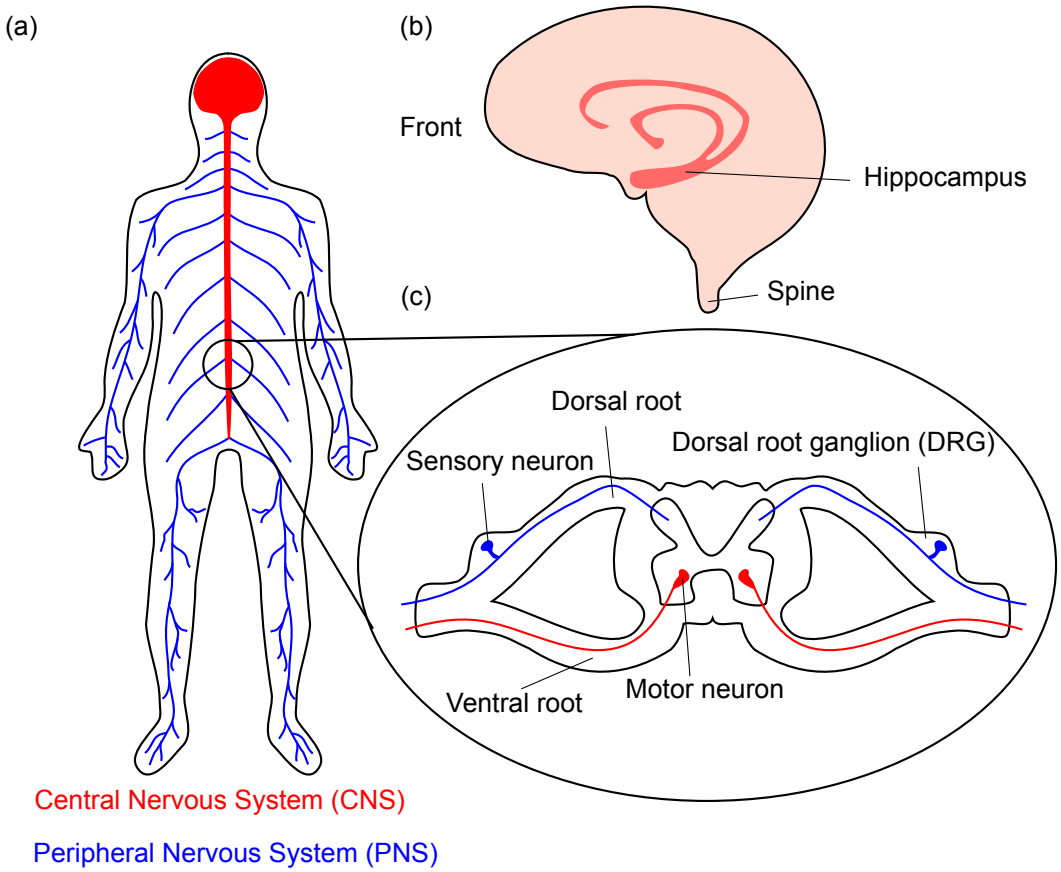

Figure 4.1: (a) Overview of CNS and PNS. (b) Side-view of the human brain with hippocampus. (c) Top-view of part of the spinal cord and the attached dorsal root ganglia (DRG).

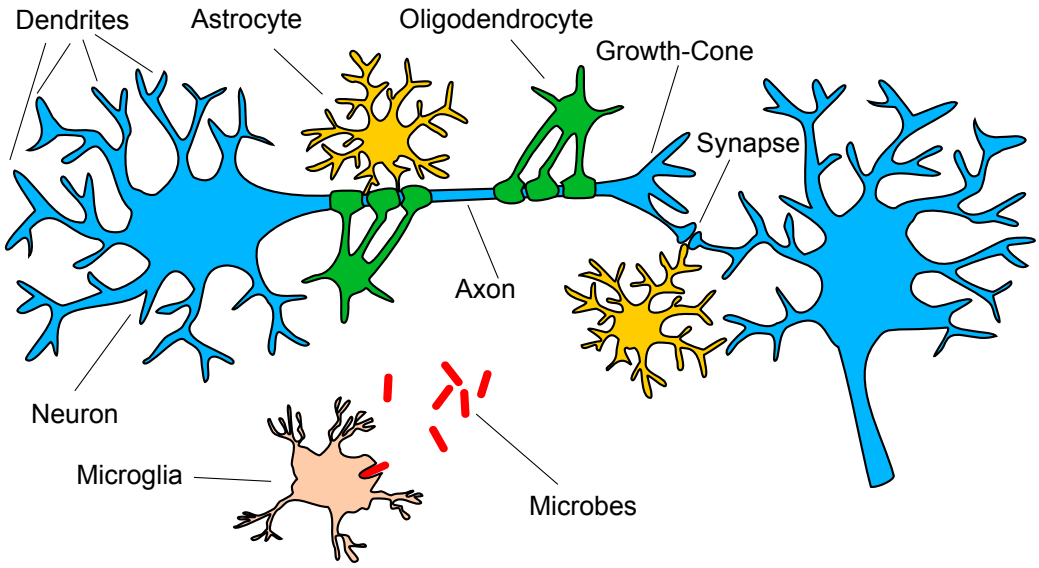

Figure 4.2: Overview of the different cells in the human brain.

convert electrical signals to a chemical reaction and vice versa to allow fast intercellular communication. In humans axons can become longer than 1 m to form for instance the connection between our big toe and the spinal cord. These direct connections are important as electrical signals can be transmitted much faster than chemical signals which is what would happen at the synapses if the path would consist of multiple cells. The axons are insulated with *myelin* to allow more efficient charge transport. In the brain the myelin sheets are formed by *oligodendrocytes* and outside of the brain by specialised cells called *Schwann cells*.

There are numerous kinds of different neurons in the human body to accommodate various functions; most literature uses the following classification based on the direction of the signal transmission: *Sensory neurons* or *afferent neurons* are the receptors which convey external stimuli to the CNS. *Motor neurons* or *efferent neurons* which transmit signals from the CNS to the muscles to cause a reaction. The third kind are *interneurons* which either form connection between interneurons or between motor neurons and sensory neurons. Each of those groups can again be divided in other subgroups, however, further detail is not crucial for this thesis.

In this work we will not use primary human cells but a model system (mice) to study the force generation of neurons. More specifically, neurons from the *dorsal root ganglia* (cf. Fig.4.1c) will be obtained to investigate the strength of axon growth cones (see below). The dorsal root ganglia are located close to the spinal cord and contain the cell bodies of sensory neurons.

Axon Growth

An outgrowing axon can be divided into two distinct regions (cf. Fig.4.3). First, the central zone which is the tube like structure rich in microtubules. Second, at the opposite site to the cell body is the axon growth cone, an actin rich region. Whilst the main function of the central region — when a connection with one or more other neurons has been established— is the electrical connection to transmit information; during axon outgrowth it also serves as a pipeline for transport of components needed in the growth cone. The microtubules

are aligned with their plus end to the growth cone to facilitate efficient high throughput transport which mainly occurs via kinesin motor proteins. In addition, Xu et al. found that structural support of the axon is enhanced by rings of actin linked with *aducin* and *spectrin*[98].

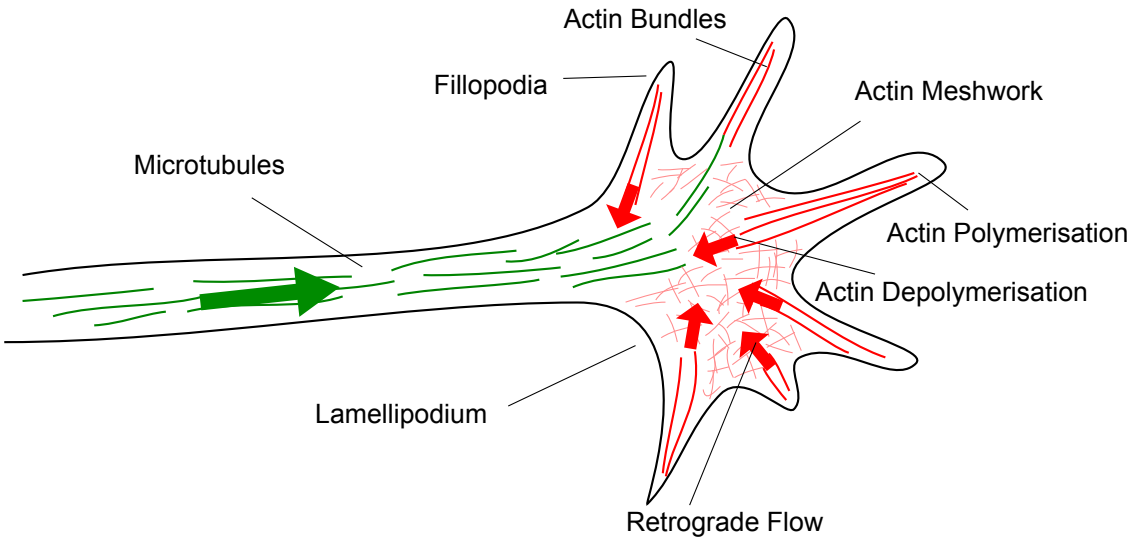

Figure 4.3: Schematic of growth cone with outgrowth model.

The growth cone itself is a lamellipodium with outgrowing filopodia probing the environment. The current model for growth cone dynamics suggests that actin filaments extend via polymerisation at their plus end which is located at the leading edge of the growth cone. However, the actin polymers also depolymerise at their minus end which is close to the microtubule. The whole actin filaments are constantly pulled back into the lamellipodia by motor proteins which results in no or only little net advancement of the actin filaments. This retrograde flow of actin also prevents the microtubule from advancing further into the growth cone. The described mechanism is often compared to an unengaged clutch. The clutch is engaged if a filopodia can establish a stable connection with the ECM. Then, the forces of the molecular motors are not sufficient to pull the actin filaments back and the growth cone will experience a growth in the direction of to ECM attached filopodia. The lag of retrograde flow may then allow microtubule to advance further, resulting in an overall extension of the axon.[99–101, 29, 16]

The above model suggests that axon outgrowth is highly dependent on the proteins present in the ECM as adhesion sites will favour specific proteins. In fact, this has been demonstrated by Nichol et al. by comparing the change in retrograde flow using laminin or poly-d-lysine (PDL) as substrate coating[101]. Beside electrical [102–106] and chemical[107–110] stimuli, mechanical cues like ECM stiffness or forces exerted by surrounding cells provide an additional pathway of growth cone guidance[111, 67, 16, 69, 112].

Because of their interesting growth mechanics and their importance in neural development and neuroregeneration growth cones are an interesting system to study. However, at the same time, their small structure and weak force generation make it technically very challenging to quantify the mechanical forces.

4.1.2 Glial Cells

The group of glial cells is comprised of[1] *astrocytes*, *oligodendrocytes*, and *microglia*[97]. Only astrocytes and microglia will be discussed in more detail on the next pages as no measurements have been done on oligodendrocytes for this thesis.

Astrocytes

Astrocytes are the most abundant type of glia cells in the brain and got their name from their usually star shaped structure which is caused by the many processes they extend to connect with different neurons (cf. Fig. 4.2)[113]. They provide structural support to neurons and their synapses and they maintain the appropriate chemical environment for neural signalling. As apparent from the name "glia" (which is Greek for "glue"), researches thought of glia cells only as supporting cells with the neurons being the sole contributor to cognitive function.

This picture has started to change in the last years as an increasing amount of data showed evidence for the active role of glia cells on the brain functions[114]. In fact, human astrocytes are much more complex in morphology and function compared to their

[1] We follow here the definition of Purves et al. in reference [97]. However, in other definitions *ependyma cells* are part of the glia cells in the central nervous system, and *Schwann cells* and *satellite glia cells* of the peripheral nervous system.

counterparts from rodents which serve as the main model system for studies on the brain [115]. Han et al. have shown that chimeric mice — their CNS was comprised of neurons and oligodendrocytes from mice but astrocytes originating from human progenitor cells — performed significantly better in all tested learning and memory tasks compared to control mice[116]. Furthermore astrocytes are known to communicate via calcium waves which cause expression of neurotransmitters like glutamate. Therefore, astrocytes have a pathway not only to exchange information between each other but also to affect signalling at synapses, indicating that astrocytes can actively influence inter-neuron communication[117–119].

Upon injury of the CNS, astrocytes move to the lesion and proliferate in order to fill the gap[120]. It has been found that this newly formed scar tissue influences axon regeneration negatively and positively. In itself the glia scar forms partially a physical barrier against regenerating axons, however, the astrocytes in the scar are in an activated state promoting the secretion of ECM molecules which can inhibit but also promote axon regeneration[120–122]. In addition, the scar tissue is likely to be stiffer than the surrounding tissue forming a different mechanical environment. Moshayedi et al. showed that astrocytes grown on substrates with different stiffness will show a different morphology, possibly affecting the physiological function of the cells[123–125].

This data indicates that the development and function of the brain is influenced by a well functioning and possibly more complex system of astrocytes. In conclusion, astrocytes are currently of great scientific interest in particular with respect to their role in brain function. Their investigation with respect to mechanical cues is likely to give significant insight into the development of the CNS as well as into astrocyte behaviour in glia scars and in the presence of implants.

Microglia

Microglia are very different cells compared to the other cells found in the brain. They have more in common with macrophages, cells which clean the body from cell debris and pathogens via phagocytosis (cf. Fig.4.2). Microglia mainly originate from hematopoietic precursor cells in the bone marrow and migrate to the brain prenatally . Only in exceptional

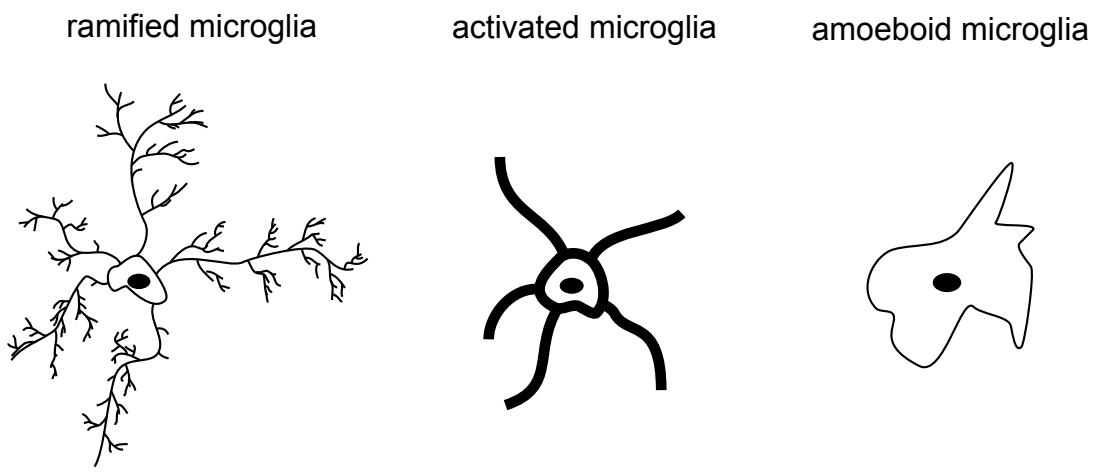

Figure 4.4: Overview of the different states of microglia. Figure inspired by Fig. 7.5 in reference[133].

circumstances macrophages are able to pass the blood brain barrier[126]. The total population of microglia is maintained through proliferation and increased when needed, e.g. during inflammation. They regulate cell survival and cell death during inflammation by secreting a variety of signalling molecules like cytokines[97]. Sieger et al. demonstrated that microglia will migrate to an injury guided by the calcium concentration[127]. However, since microglia are supposed to induce cell death if needed (e.g. during neuroinflammation) an overproduction of microglia combined with continuous activation is associated with Alzheimer's disease due to an increase in neuronal death[128–132].

In the literature the morphology of microglia is mainly described by three states[133] which we show in Fig. 4.4: 1) Ramified microglia extend multiple branched processes (cf. Fig. 4.4, left) and are highly sensitive to external biochemical or biomechanical stimuli; 2) activated microglia, cells which show fewer but thicker processes (cf. Fig. 4.4, middle) than cells in state 1); 3) phagocytotic or amoeboid microglia, cells which move around and can take up cell debris or pathogens (cf. Fig. 4.4, right).

Microglia generally do not exist in their ramified state in culture although this is the most common state in the healthy brain[133] and we did not observe the morphology characteristic of the ramified state in our experiment. Microglia switch to the "activated" or "amoeboid" state when they detect pathogens or injured cells[133–135]. There are many

sub-states to accommodate different situations, e.g. for cell proliferation or expression of cytokines[136, 137]. Microglia in their amoeboid state might be set to clean regions of the brain from cell debris or to exhibit phagocytotic behaviour to fight pathogens.

4.2 KIAA0319 - a Gene Associated with Dyslexia and Its Role in Neuronal Migration

The work presented in the following section is a collaboration between Rebeca Diaz Vazquez (School of Medicine) and Philipp Liehm. The biochemistry and genomics part of the the project is led by Rebeca Diaz Vazquez as part of her PhD (in progress) under supervision of Dr. Silvia Paracchini. Philipp Liehm performed the ERISM measurement, analysis of the cell speed (on the ERISM micro-cavity), and analysis of the vertical displacement maps including interpretation of the results.

4.2.1 Motivation

In this section we want to investigate the role of the protein *KIAA0319* in cell migration. The protein is coded by the gene KIAA0319 (same name as the protein); genetic variants of this gene have been linked to dyslexia[2] in numerous studies[138–143]. Paracchini et al. demonstrated that in rats the protein is involved in guiding neurons along radial glial cells[144], a process crucial in the development of the brain cortex. KIAA0319 is a transmembrane protein and its structure suggests a role as receptor and signal transducer which communicates extracellular cues to the cell. However, the exact function of KIAA0319 remains elusive.

To illuminate the function of KIAA0319 during cell migration, we use RPE1 cells, a cell line derived from human retina pigmented epithelium, as a model system. Rebeca Diaz Vazquez created a KIAA0319 knock-out in RPE1 cells to investigate whether cell speed and cell forces differ in the presence and absence of KIAA0319. We demonstrate that the capability of ERISM to measure a high number of cells over an extended period of time is crucial for comparing populations of knock-out cells and wild-type cells.

[2] Dyslexia is a reading disorder despite normal intelligence.

4.2.2 Experiment

A KIAA0319 knock-out cell line was created using the gene editing tool *CRISP-Cas9*[145]. Martinez-Garay et al. showed that in KIAA0319 knock-out mice a complete loss of KIAA0319 does not lead to a clear disturbance of neural migration[146] as was observed by Paracchini et al. in rats[144]. This suggests that the absence of KIAA0319 might be compensated by other proteins. Therefore, we created a knock-out where the protein is still expressed but its ability to localise to the cell membrane disabled and thus the function of KIAA0319 as a transmembrane protein inhibited. Knock-out cells and wild-type cells were stained for KIAA0319 and we observed a clear expression of KIAA0319 at the cell membrane in the wild-type cells but not in the knock-out cells (data not shown).

To measure cell speed and cell forces we seeded wild-type and knock-out RPE1 cells at a density of 2000 cells per square centimetre on an ERISM micro-cavity with apparent stiffness of 15 kPa[3]. No coating was applied to the micro-cavities, which have a gold surface, because the RPE1 cells even adhere to uncoated glass substrates. The cell populations were separated by a silicone wall preventing mixing of the populations. The cell medium was comprised of DMEM with 10 vol% Fetal Bovine Serum (FBS) and 1 vol% Penicillin Streptomycin (P/S). After we seeded the cells on the ERISM substrate, we waited for 24 h before we started the measurement to allow the cells to attach to the substrate in order to observe pure cell migration and not artefacts from seeding the cells, i.e. initial cell attachment.

To obtain statistically significant results, we aimed to measure more than 50 cells for each population. Therefore, we performed ERISM measurements of wild-type and knock-out cells at 27 different positions/ fields of view using a 20x objective and taking frames of each position every 5 min over 17 h.

[3]We chose to make the samples used in this experiment significantly stiffer than the stiffness of the brain which is two orders of magnitudes lower. This was necessary to avoid too large deformations of the micro-cavities as the RPE1 cells are much stronger than neurons.

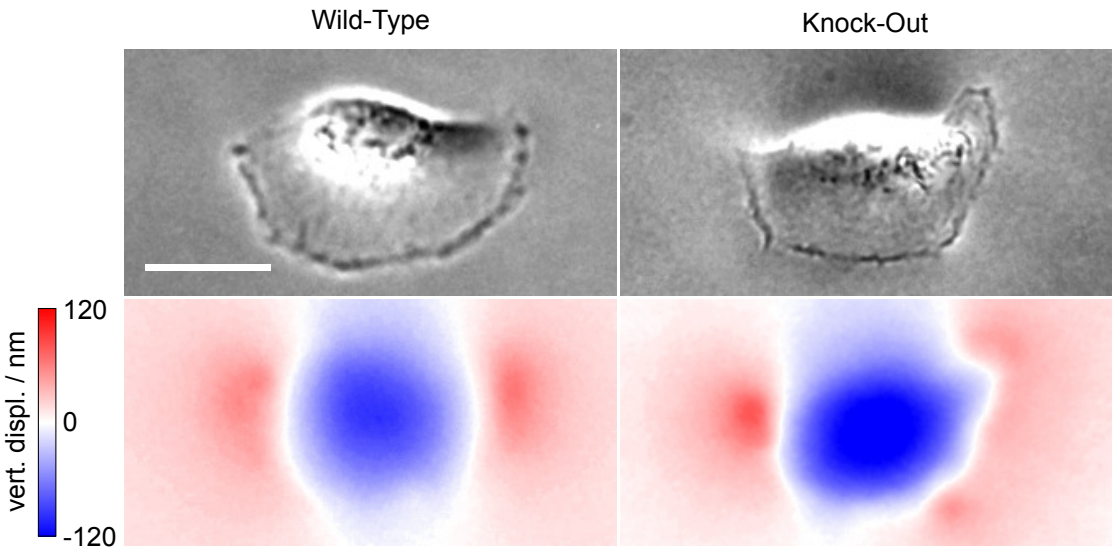

Figure 4.5: Phase-contrast and ERISM vertical displacement map for one wild-type and one knock-out cell. Scale bar, 25 µm

4.2.3 Data-Analysis and Results

In Fig. 4.5 we show phase-contrast images and ERISM displacement maps for one wild-type and one knock-out cell. We do not see any obvious differences in cell morphology between the two cell populations.

We measured the speed of all cells over the 17 h measurement time. This was done using the *ImageJ* plugin *MTrackJ*[147]. The plugin requires the user to click on the position for each frame. We always took the position where we believed the centre of the nucleus to be as an estimate of the position of the cell. Most of the time this was straightforward and unambiguous as the nucleus is well visible in the phase-contrast images (cf. Fig. 4.5). The relatively low speed of the cells did not require tracking the cells in each frame, therefore, we only tracked every 5th frame, i.e. every 25 min. Every time a cell was dividing into two daughter cells, we stopped the tracking before the cell started to divide and tracked each individual daughter cell after the cell division.

Figure 4.6a shows the distributions of the mean of the cell speed for 109 wild-type and 154 knock-out cells. We find that the median of the cell speed of the wild-type cells and the knock-out cells is 1.55 µm min^{-1} and 0.95 µm min^{-1}, respectively. The distribution of the wild-type cells does not have a clear maximum; in fact, we can find two separated peaks at

around 1 µm min^{-1} and 1.7 µm min^{-1}. By contrast, the distribution for the knock-out cells has only one peak at around 0.8 µm min^{-1}. We performed a Mann-Whitney U test on both populations and find that they are significantly different with a p value below 0.001.

This result matches with what we observed by performing a standard scratch test. Here, part of a confluent cell layer (on glass) is scratched away to create a gap. In this test, the wild-type cells would close the gap much faster than the knock-out cells[4].

In the next step we analysed the ERISM displacement maps to investigate whether wild-type and knock-out cells apply different forces to the substrate. The maximum and minimum displacement was measured for each cell in the first frame of the time-lapse data set. We used the image synchronisation function in *ImageJ* to synchronise the mouse cursor between phase-contrast images and ERISM displacement maps. Whilst looking at both images, we selected an area around each cell, the area would be automatically drawn in both images, which would include maximum and minimum vertical displacement for the cell of interest but not any other cell. A side-by-side comparison of displacement maps and phase-contrast images is especially important to ensure that small vertical displacements of weaker cells are not missed. With this approach we obtained the maximum and minimum displacement induced by 73 wild-type and 79 knock-out cells at one time point.

The results for this measurement are summarised in Fig. 4.6c (left and middle). We find that the knock-out cells pull and indent the ERISM micro-cavity by a factor of approx. 1.5 more than the wild-type cells do. The Mann-Whitney U test yields a p value smaller than 0.001 for maximum pulling and maximum indentation.

We measured the maximum indentation of multiple cells over 17 h (this time considering every frame) and found that the vertical displacement under each cell can change by more than 200 nm during the 17 h (cf. example in Fig. 4.6b). In addition to cell-to-cell variations, which are caused by the individual properties of each cell, variations over time can be compensated by measuring many cells at the same time point. This is why the measurement over 73 and 79 cells is likely to show differences of the cell populations and not just cell-to-cell variations. However, to improve the quality of our results even further, we measured the

[4]Scratch test was performed and analysed by Rebeca Diaz Vazquez. Data not shown.

maximum indentation[5] for each cell at every 10th frame following a similar procedure as for the cell speed measurement. *MTrackJ* can automatically snap the tracking point to the lowest or highest value in a region (e.g 50 px × 50 px) around the mouse cursor which makes the manual tracking of maximum indentation very time efficient. Following this approach, we were able to measure the maximum indentation for each cell in the image for every time frame we investigated.

Although we did not measure substantially more cells than in the previous measurement[6], we took on average 20 measurements for each cell over time. This increases the number of data points for each cell population from 73/79 to 1860/2249 for wild-type/knock-out cells. The distributions are presented in Fig. 4.6c (right). The median values of the two distributions differ slightly more than for the smaller data set. More importantly, the larger dataset reveals a striking difference in the shape of the distribution for wild-type and knock-out cells. The maximum indentation of the knock-out cells follows an approximately Gaussian shaped distribution with a peak at −80 nm whereas the distribution of the wild-type cells is not only shifted but skewed towards smaller indentations and peaks at −35 nm.

4.2.4 Discussion

Our results clearly show a difference in cellular forces between RPE1 cells which have the KIAA0319 protein at the cell membrane (wild-type) and which do not. The scratch test and the speed analysis suggest that mechanisms behind cell movement and/or cell-substrate adhesion are altered by the lack of KIAA0319. This finding is supported by the measurements we performed with ERISM. Interestingly, we do not only find that the knock-out cells apply on average higher forces than the wild-type cells but we also find a significant difference in the shape of the distribution curves for the two populations. The Gaussian shape for the knock-out cells suggests that here, the difference in force between individual cells is randomly distributed. By contrast, the skewed distribution curve of the wild-type cells

[5] We did not measure the maximum pulling because each cell has multiple pulling sites and it is therefore much more time consuming to find the maximum pulling for each cell. Moreover, there should be a balance between pushing and pulling and Fig.4.6c (left and middle) confirms that the difference in cell strength leads to a difference in maximum pulling as well as maximum indentation.

[6] The number of cells increased approximately by a factor of 0.5 because of proliferation.

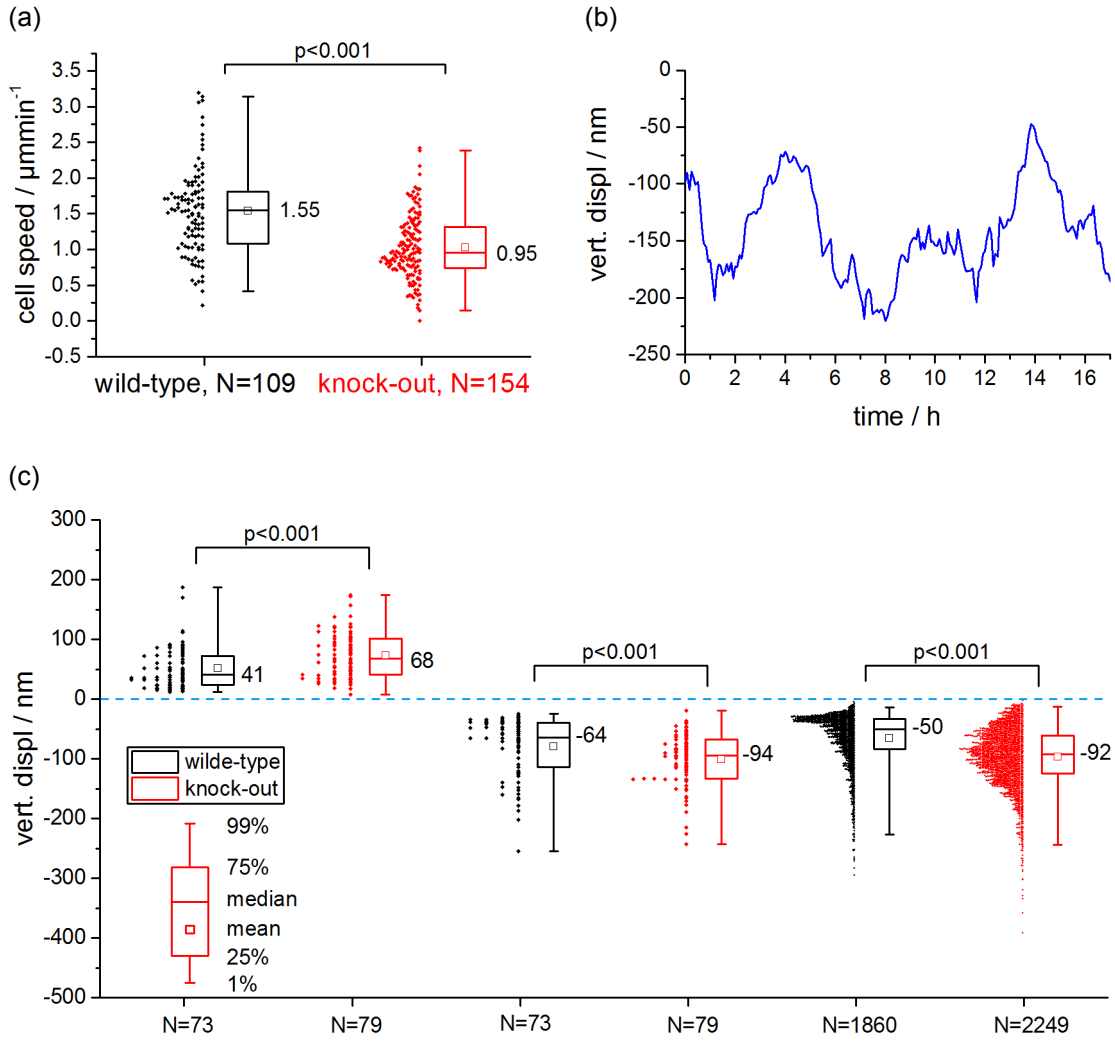

Figure 4.6: Comparison between wild-type and knock-out cells. (a) Cell speed, data points represent the mean value for each cell. (b) Maximum indentation over time for one cell. (c) Maximum pulling (left) and maximum indentation (middle) for all cells of the first frame of each field of view. Right, same as in the middle, but every 10th frame of the data set (17 h every 5 min), i.e. the same cells were measured at different time points. Statistical tests: non-parametric Mann-Whitney U test.

suggests that theses cells have a control mechanism in place which favours lower forces or smaller deformations[7] of the ECM and limits the applied forces to a narrower range. Although the shapes of the distributions of the cell speed are also different for the two populations, the cell speed data does not indicate the presence of a control mechanism in the wild-type cells. Only a measurement of cellular force on a large cell population as provided by ERISM allowed to identify this mechanism.

At this stage we cannot tell how exactly KIAA0319 regulates cell forces.

It is suggested that KIAA0319 fulfils a sensory function at the cell membrane, hence, the transmembrane protein might report on ECM proteins or biochemical cues secreted by other cells. Further studies should investigate whether the same results are obtained if the substrate is coated with different ECM proteins (here, no coating was applied). In addition, staining of the cytoskeleton and focal adhesions might provide further information on how KIAA0319 interacts with other transmembrane proteins like integrins or if actin and microtubule arrangement changes if KIAA0319 is not present at the cell membrane. It is worth noting that the knock-out of KIAA0319 was performed such that the protein can still be found in the cells, but is prevented from reaching the cell membrane. Therefore, it might be interesting to perform a complete knock-out of the gene to test whether the function of KIAA0319 is compensated by other proteins. Ultimately, a KIAA0319 knock-out of human neurons, possibly derived from stem cells, should be created to investigate if the difference in cell speed and cell force we observed for the RPE1 cells persists in neurons.

In summary, our results indicate that KIAA0319 is a dominant factor in controlling stress generation and/or cell adhesion in RPE1 cells and therefore possibly also in neurons. We demonstrated that ERISM can be used as a tool to test whether specific proteins are associated with cell mechanical functions. We think that it would be very difficult to perform similar measurements on such high numbers of cells and time frames with other force sensing techniques.

[7] We cannot tell if the mechanism is force/stress driven or determined by the absolute displacement.

4.3 Astrocytes and Microglia - Who Is Stronger?

In the previous section we introduced astrocytes and microglia as vital parts of the CNS. Although morphological changes of both cell types have been observed in response to substrates with different compliance[123, 124, 148], the stress these cells exert on substrates has only been measured for microglia[148]. In this section we will test whether both cell types grow on our ERISM micro-cavities, if we can observe the forces these cells exert on the substrates, and how these forces differ between astrocytes and microglia.

4.3.1 Experiment

To obtain primary astrocytes and microglia from mice, we followed the protocol of Mecha et al. [149]. Briefly: Cortical tissue was obtained from 1–3 days old mouse pubs. The tissue was dissociated according to the protocol. Then, the cell suspension was seeded on poly-D-lysine (PDL, 5 $\mu g\,mL^{-1}$ in H_2O) coated cell culture flasks. In this step the medium contains DMEM, 10% Fetal Bovine Serum (FBS), 10% Horse Serum (HS), and 1% Penicillin/Streptomycin (P/S) (DMEM:10:10:1). After 9 d the cell culture flasks contained a confluent layer of astrocytes on the bottom and microglia and oligodendrocytes (or oligodendrocyte precursor cells, OPCs) on top of the astrocyte layer. Then, the flasks were put on an orbital shaker (Boeco OS 20) for 3 h at 230 rpm. The cell medium, containing mainly microglia cells, was removed, centrifuged and seeded in another PDL coated flask in similar cell medium but with only 5% FBS and 5% HS (DMEM:5:5:1).

Because we wanted an astrocyte culture without oligodendrocytes and OPCs, we added medium (DMEM:10:10:1) to the flasks with the remaining cells and placed the flasks for another 15 h on the orbital shaker. We then removed the medium which would now contain most of the oligodendrocytes and OPCs, and added medium (DMEM:10:10:1) to the flask with the astrocytes.

From here on we performed independent experiments with astrocytes and microglia from the separated cell populations unless stated otherwise.

4.3.2 Astrocytes

First, we seeded astrocytes on an ERISM micro-cavity with apparent Young's modulus of $E' = 4\,\mathrm{kPa}$[8] coated with PDL. We aimed to measure the forces shortly after the cells attach to the sensor. Therefore, 1h after seeding we transferred the cells on the micro-cavity to the on-stage incubator of the ERISM setup. Then, we took an ERISM measurement every 5 min over 15 h[9]. After the measurement, we calculated the displacement maps according to Section 3.4.

Results

Figure 4.7 shows a series of phase-contrast and ERISM images with a frame every 1.5 h. In the beginning, the cell induces two broad extrusions of surface at its edge, counterbalanced by a broad indentation in the centre. The pulling sites, where the cell is attached, do not seem to have fixed positions but are rotating around the cell (cf. the first two frames in Fig. 4.7). This might be an indication that the cell is actively probing the surface for the most favourable points to attach, or to decide if it should attach at all. After 3 h the cell forms more distinct adhesion sites (sharper pulling features appear on the substrate). The adhesion sites which are well visible at 6 h seem to be stable as they are still present at 13.5 h, even though they are shifted outwards as the cell area has increased.

The forces during cell spreading of mouse embryonic fibroblasts have been investigated by the group of M. Sheetz[150–152]. In their publications they show that the process of cell adhesion and spreading can be described by three phases: phase 0, creation of initial contact; phase 1, fast increase in contact area; phase 2, slower protrusion and eventually polarisation. Dubin-Thaler et al. found that the fastest increase in cell area happens during

[8] We chose a stiffness of 4 kPa (as opposed to 15 kPa which we used in the previous section for the RPE1 cells) as it was not possible at the time of this experiment to fabricate stiffer samples which would have been, as we will see further down in the text, more suitable for the relatively strong astrocytes. Moreover, using softer substrates allows us to compare the results for the astrocytes with the results for a weaker cell type, microglia, see below.

[9] At the time this experiment was done we did not have a motorised stage, therefore we could only observe one field of view.

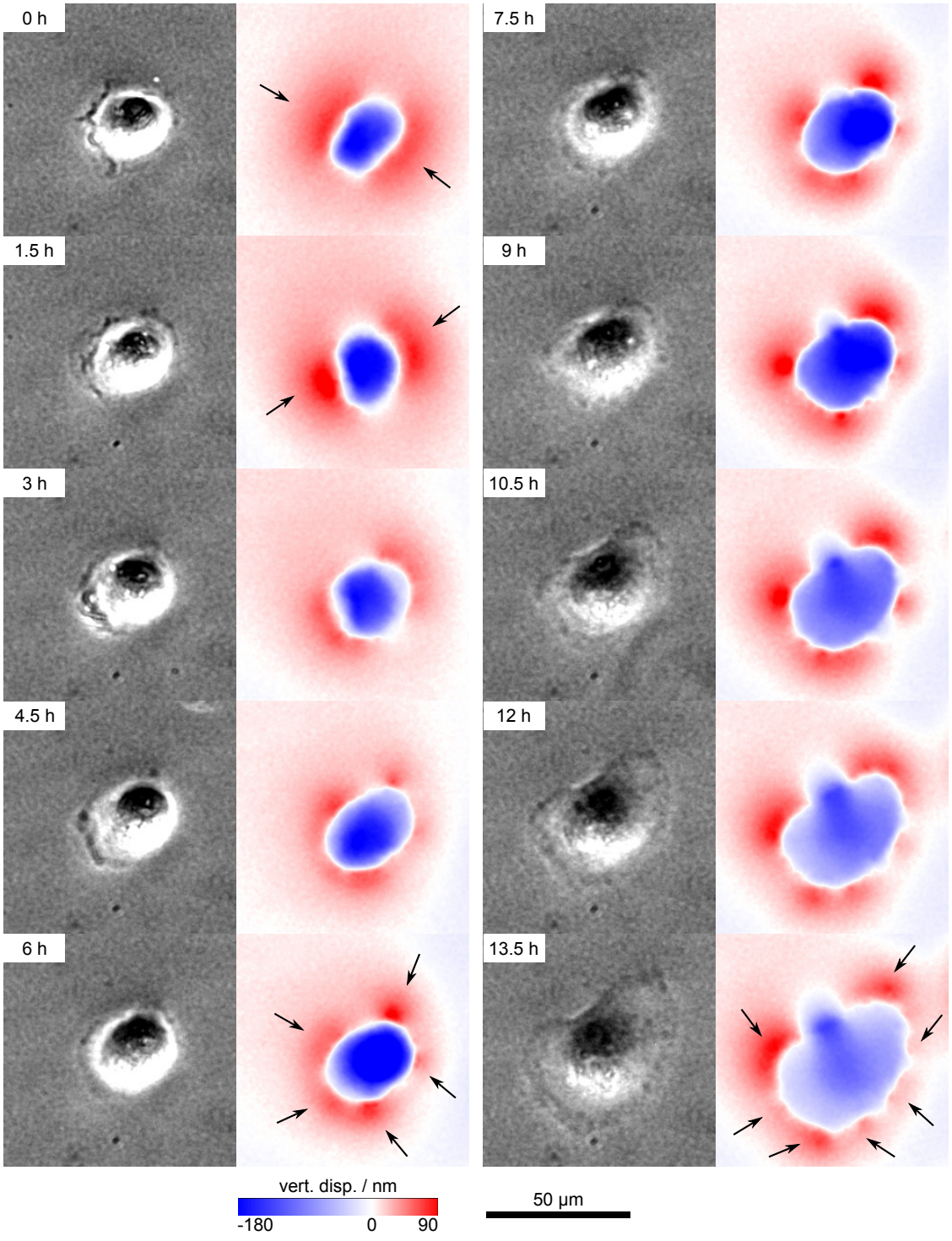

Figure 4.7: Time-lapse of astrocyte attaching to an ERISM micro-cavity surface.

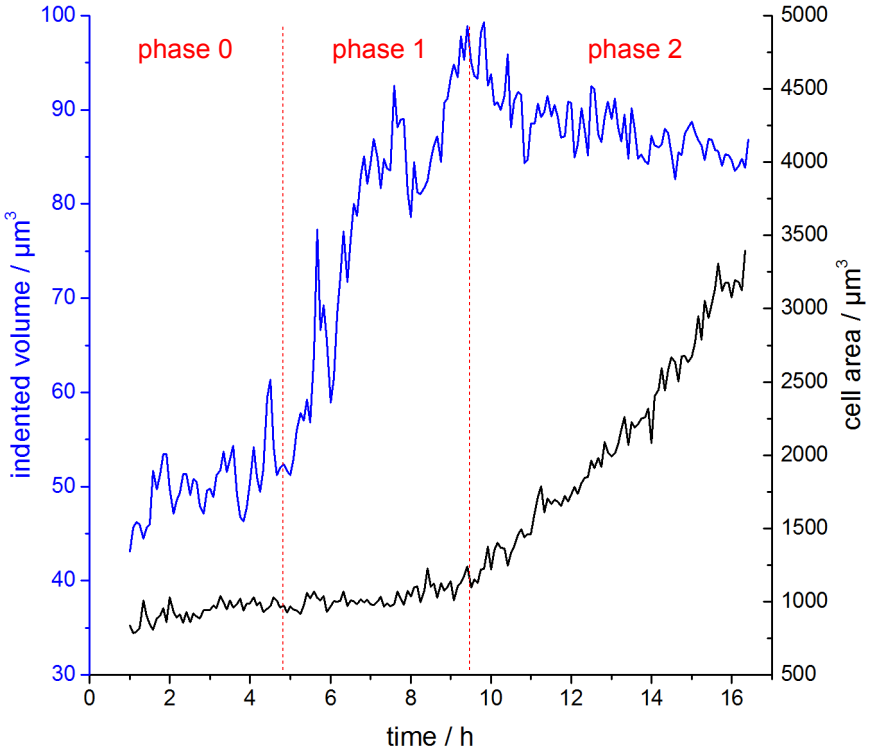

Figure 4.8: Total indented volume (blue) and cell area (black) over time. Same data set as in Fig. 4.7.Indented volume is proportional to total force applied by cell (see text).

phase 1. The total force the cells applied to a micro-pillar array increased significantly at the transition from phase 1 to phase 2 (cf. Fig. 6 in reference [151]).

Here, we use ERISM to measure the total indented volume, which is proportional to the applied force, and estimate the cell area from the phase-contrast images[10] (cf. Fig. 4.8). Whilst Dubin-Thaler et al. find that fibroblasts enter phase 2 already after 20 min, i.e. after significantly increasing their cell area, we find that the astrocytes need much longer to attach to the substrate and to increase the cell area. In contrast to Dubin-Thaler et al., we find that the force increases significantly *before* the cell area increases. In fact, the force stabilises once the cell starts spreading on the surface. Interestingly, although we observe a similar shape in the force-time curve as Dubin-Thaler et al. astrocytes possibly differ in how the applied force is linked to the cell area compared to fibroblasts. It is also possible that we did

[10] Cell outline is drawn by hand in Imagej.

not measure the astrocytes for long enough, i.e. , we maybe would have observed a further increase in force after the cell stopped increasing in area; but at this point this is speculation.

Staining - Astrocytes

A comprehensive understanding of mechanical cell processes may only be obtained if in addition to measuring cell forces, biochemical parameters are investigated as well. This might be important to link a certain state of a cell, for instance in the cell cycle, to the associated mechanical forces. Staining proteins either in living or fixed cells are important tools to link forces and proteins during specific cell processes.

ERISM force measurements do not require detaching the cells from the substrate surface. Therefore, we want to show that we can fix cells on the micro-cavity surface and apply antibody staining to visualise cell specific proteins. Following the same protocol as in the previous experiment, we acquired astrocytes and seeded them on an ERISM micro-cavity. After one day on the micro-cavity, we measured ERISM displacement maps before we fixed the cells and followed a standard antibody staining protocol[11] (cf. Appendix C). The cells were stained for *glial-fibrillary-acidic-protein* (GFAP) (primary antibody, rabbit anti-GFAP, Dako; secondary antibody, Alexa Fluor 488® goat anti-rabbit, Life Technologies) an intermediate filament protein which is found in most astrocytes and which is one of the standard proteins researchers use to distinguish astrocytes from other cells in culture [115, 153, 149]. In addition, the nucleus was stained with Hoechst 33342 (Sigma Aldrich).

We used the translation stage and *ERISM-Read* to save the stage position before removing the sample from the setup for staining. This allowed us to easily find the cell for which we took the ERISM measurement after staining. In Fig. 4.9 we summarise this measurement and show (for the same cell) a phase-contrast image, ERISM displacement map, fluorescence image[12], and overlay of the fluorescence image and the ERISM displacement map. The

[11] We thank Dr. Hélèn O. B. Gautier (Cambridge University) for providing the protocol and advice on the choice of the antibodies.

[12] All fluorescent images in this section were acquired with a 40x objective and the standard fluorescent lamp of the microscope.

cells which we investigated stained positive for GFAP so we conclude that this is indeed an astrocyte.

We noticed that the cell in Fig. 4.9 showed less then half the intensity in the fluorescence image compared to other cells on the micro-cavity. This is not unusual as different cells may show different concentrations of GFAP, which is why staining for GFAP can be used as quantitative staining to assess cell activity[154, 155].

However, although we did not measure the ERISM displacement maps for other cells on this micro-cavity, we recorded fluorescent images at other positions of the micro-cavity to show that we can acquire high quality images even though part of the excitation and emission light is absorbed or reflected at the gold interfaces. Fig. 4.10 shows a comparison between fluorescent images acquired for the same ERISM micro-cavity as above and fluorescent images for astrocytes in a standard cell culture Petri dish. Both images have been recorded with the same intensity of the excitation light-source. The exposure time was 1 s and 5 s for the cells in the Petri dish and the cells on the micro-cavity, respectively. Because the micro-cavity comprises in total 25 nm of gold, excitation and emission light is reflected and absorbed at both gold interfaces. Therefore, we expected that the intensity would decrease by a factor of 4-5 between the cells in the Petri dish and the cells on the ERISM micro-cavity. This was confirmed as we observe similar brightness for both samples when increasing the exposure time from 1 s to 5 s.

4.3.3 Microglia

Moshayedi et al. and Bollmann et al. showed that microglia have different morphologies on substrates of different stiffness[124, 148]. Moreover, Bollmann et al. measured the traction forces of microglia on substrates with different compliance and found that the average traction forces increase with increasing substrate stiffness (starting at 0.1 kPa) until it reaches a plateau at 5 kPa. The authors also show that microglia react to stiffness gradients and move towards higher stiffness. The results of these publications show that microglia are highly receptive to mechanical stimuli which makes microglia an interesting target to investigate cell mechanical processes.

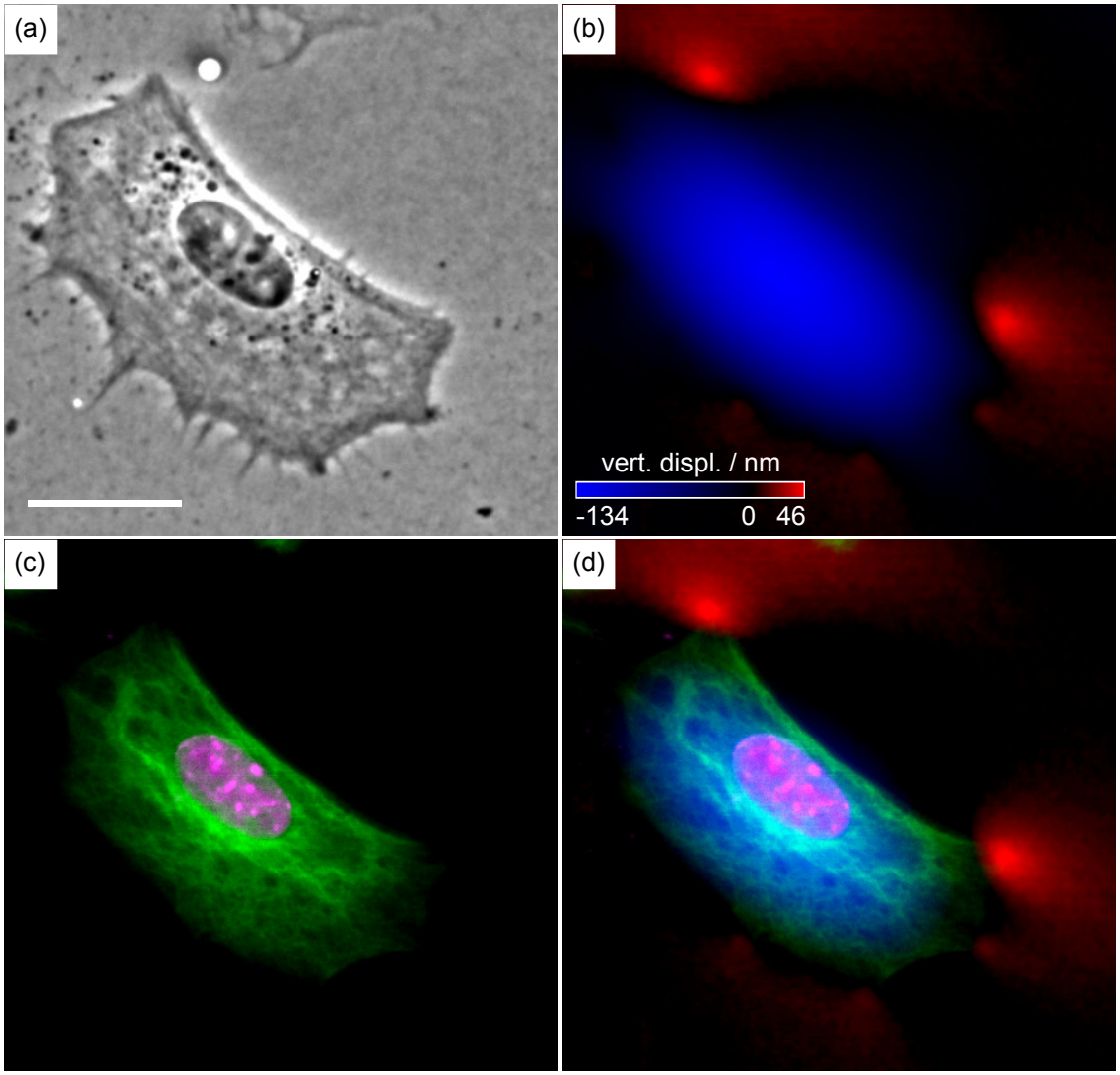

Figure 4.9: ERISM measurement and GFAP staining of astrocyte on ERISM micro-cavity. (a) Phase-contrast image. Scale bar, 25 µm. (b) ERISM displacement map. (c) Antibody staining for GFAP (green) and counter staining with Hoechst 33342 (magenta). (c) Overlay of (b) and (c).

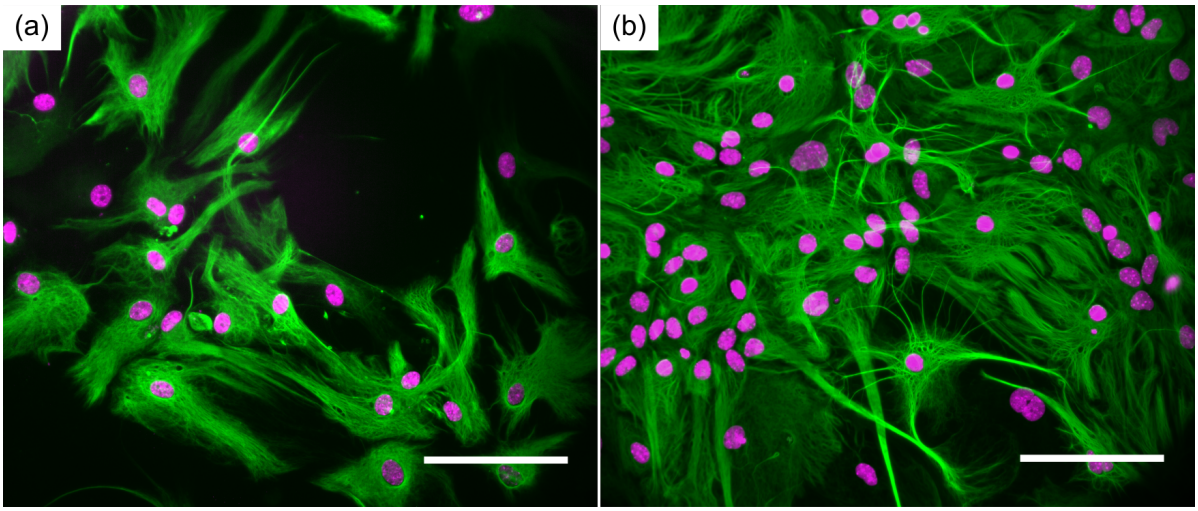

Figure 4.10: Antibody staining for GFAP (green) in astrocytes. Counter staining with Hoechst 33342 (magenta). (a) On ERISM micro-cavity with 5 s exposure time. (b) On plastic cell culture dish with 1 s exposure time.

Motivated by these results we tested whether ERISM can be used to measure the forces exerted by microglia. We seeded microglia on an ERISM micro-cavity with similar apparent Young's modulus as we used for the measurements of the astrocytes ($E' = 4$ kPa, PDL coating). The cells have been on the micro-cavity for 12 h before we started to measure the cells for one hour every two minutes on the ERISM setup.

Results

In culture and during the measurement we observed mainly two different morphologies: 1) Microglia which showed thick processes but were not moving. 2) Migrating microglia which exhibited an amoeboid morphology. These morphologies agree well with what we discussed earlier in the background section about microglia (cf. Section 4.1.2 and Fig. 4.4, middle and right). Figure 4.11 and 4.12 show examples for the two cases.

In Fig. 4.11 we can see how the cell undergoes significant morphological changes within one hour. First the cell does not have any sizeable processes, then it elongates and extends a process rectangular to the current long axis of the cell. Finally, at 60 min the cell shows 5 thicker process of varying length. During the whole time of the measurement the cell shows similar levels of vertical displacement under the cell body. The push/pull pattern develops

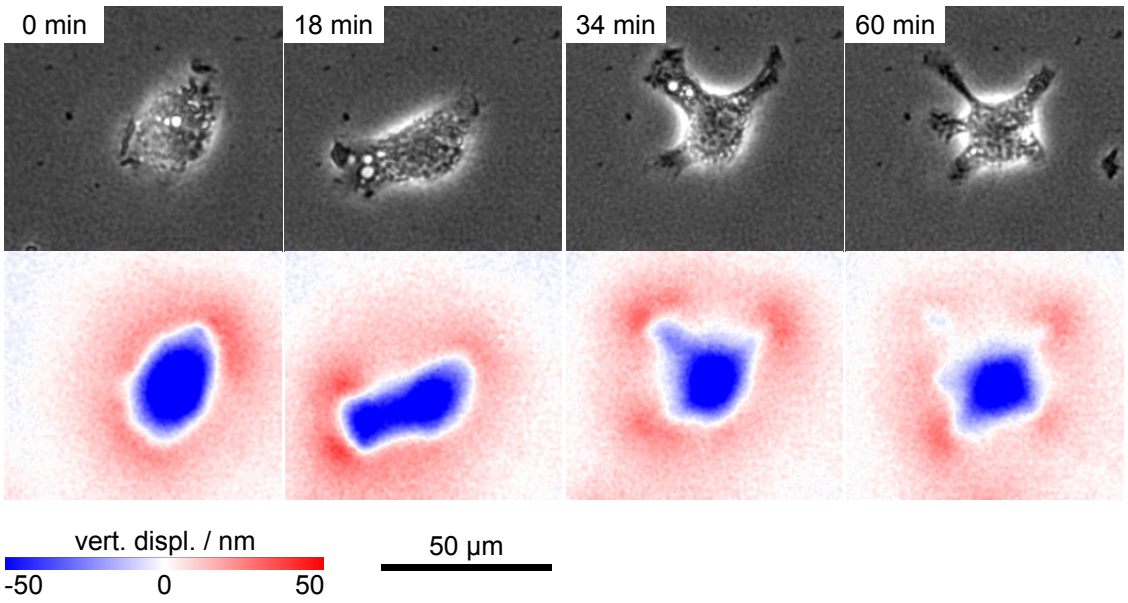

Figure 4.11: Activated microglia undergoing substantial morphological changes over 1 h.

from a very round symmetric pattern to a localised pattern of pulling corresponding to the individual processes. Possibly these forces are applied to sense the mechanical environment in addition to attaching the processes to the substrate surface. The cell does not change its position over the course of one hour.

In Fig. 4.12 we show an example for an amoeboid shaped microglia. This cell deforms the micro-cavity by a factor of 5 less then in the previous example. However, in contrast to the previous microglia, this cell is actively moving over the substrate presumably looking for cell debris or pathogens. Furthermore, the cell is retracting and extending processes while it moves over the surface.

We wondered whether activated and amoeboid cells show a systematic difference in how much they deform the substrate. Therefore, we grouped all cells in the field-of-view in two categories, amoeboid and activated, according to cell morphology. We then extracted the maximum indentation from the ERISM displacement map for each cell over time (1 h). In Fig. 4.13 we plot the mean indentation and the maximum indentation (over 1 h) for each cell. We cannot see an obvious difference between the cells with different morphologies, the population of the amoeboid cells could be part of the population of the activated cells in Fig. 4.13. More subtle differences might emerge for a higher number of cells, however,

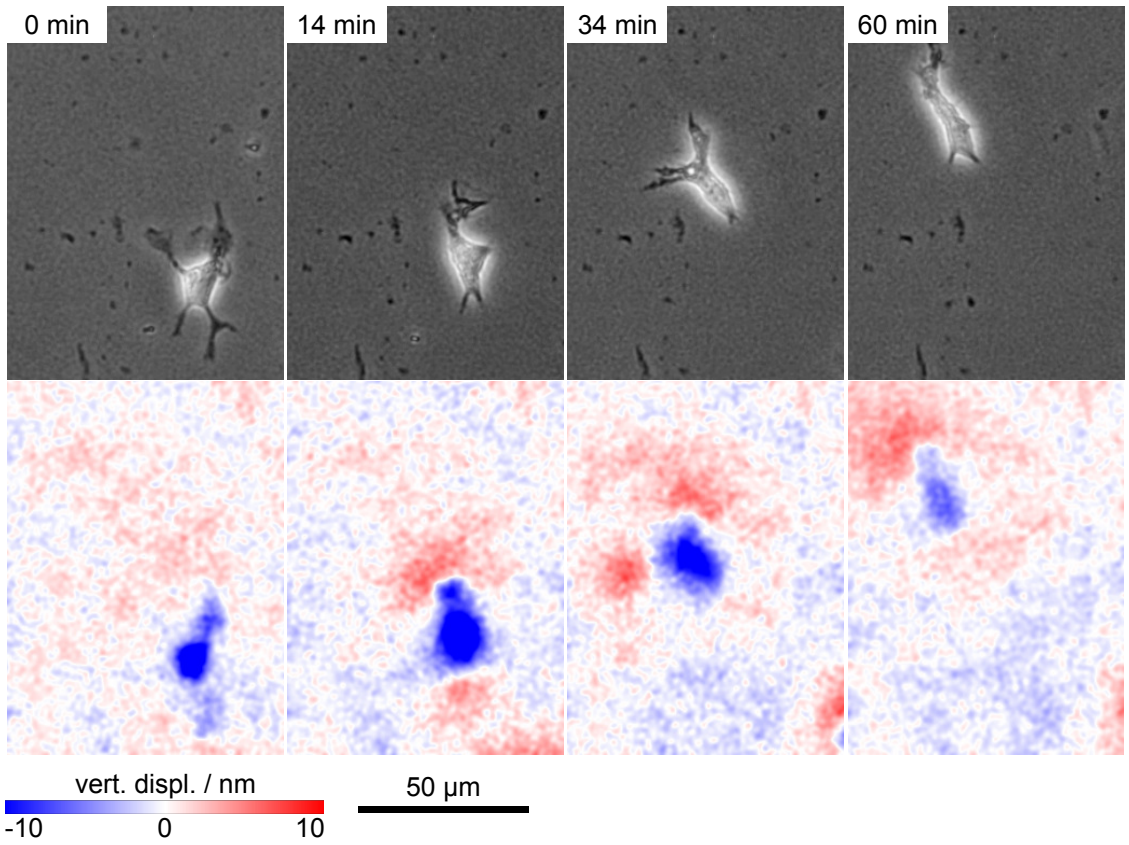

Figure 4.12: Amoeboid microglia migrating over the ERISM micro-cavity and changing from a complex branched morphology to an elongated morphology.

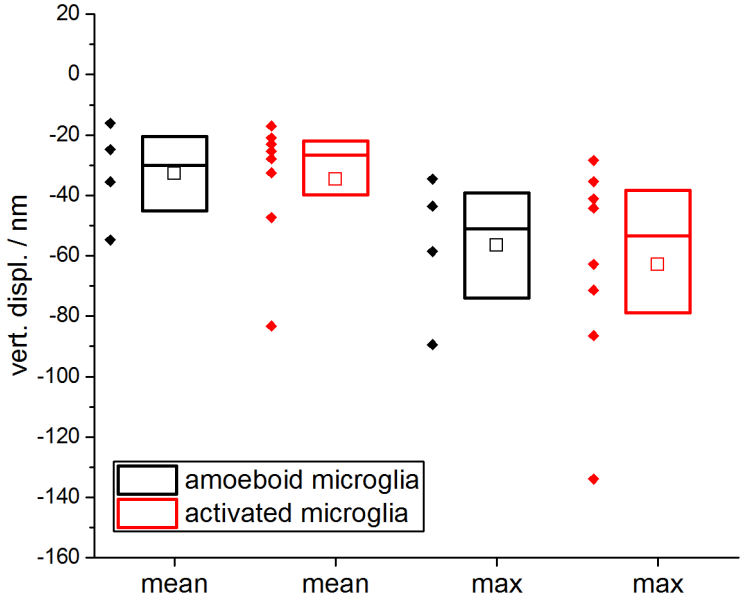

Figure 4.13: Comparison of the strength between activated and amoeboid microglia. Mean values are calculated from the time-lapse data (1 h, one frame every 2 min). In addition, "max" indicates the maximum indentation for each cell during the indentation. Open squares, mean value of the data set; boxes, indicate median value and 10–90 % of the data range. Number of measured cells: amoeboid, N=4; activated, N=8.

we only investigated a small number of cells (4 amoeboid cells, 8 activated cells) in this experiment.

Staining - Microglia

At a later stage of the ERISM project we seeded again microglia on an ERISM sensor (E'=3 kPa) to test if they would stain positive for the microglia specific marker CD11b (rat anti-CD11b, AbD Serotec; Alexa Fluor 594® goat anti-rat, Life Technologies). Figure 4.14 shows four microglia which all stained positive for CD11b. The cell morphology however was very different from what we saw in previous experiments. We did not take a long-term measurement of these cells, but hypothesise that the cells were potentially in a state where they proliferate as

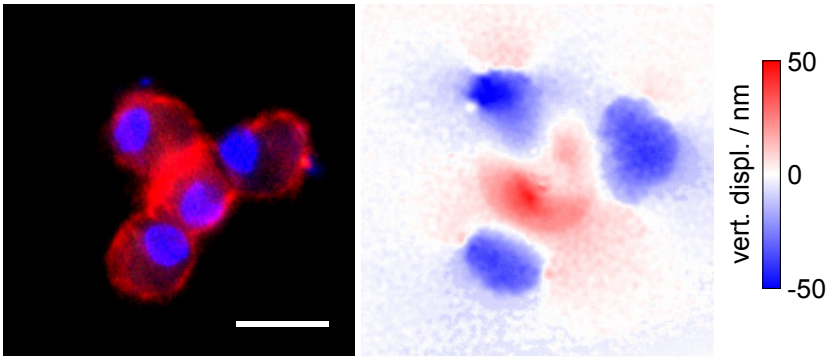

Figure 4.14: Microglia on ERISM micro-cavity. Left, fluorescence image showing the staining for CD11b (red) and nucleus (blue). Scale bar 20 µm. Right, corresponding ERISM displacement map.

we can see four cells with a round shape very closely together. The vertical displacements are in a similar range than for the cells in Fig. 4.13.

4.3.4 Astrocytes and Microglia

We showed that we can measure both, astrocytes and microglia on the ERISM micro-cavities. In the following, we compare the strength of both cell types side-by-side. To increase the statistical significance of our results, we seeded again astrocytes and microglia on ERISM micro-cavities with $E' = 4\,\text{kPa}$ and a PDL coating. The data presented in the following is comprised of the data sets we showed in the previous sections and of an additional measurement.

Surprisingly, although astrocytes are cells from a soft environment (brain) we observed that the cells applied very large displacements to the micro-cavity. In fact, the cells deformed the micro-cavity so much that for many cells *ERISM-Calc* could not calculate the vertical displacements[13]. This has two reasons: 1) We recorded the images with a 20x objective and applied binning during the image acquisition to reduce data size[14], hence, for regions in the field of view with steep gradients in thickness, adjacent fringes are so close together that they are only separated by a few pixels. 2) The contrast between bright and dark areas

[13] The example in Fig. 4.7 represents one of the weaker cells.

[14] This experiment was done at an early stage of the ERISM project when data size and bandwidth was an issue when long-term measurements with many frames were performed.

is lower in regions of steep gradients. We attribute this effect to the reduced quality of the cavity as the two mirrors are not parallel to each other any more. If the contrast is reduced, the algorithm to fit the interference minima in *ERISM-Calc* sometimes fails and no thickness is fitted for a substantial number of pixels.

Although we may not be able to fit the cavity thickness underneath all astrocytes with *ERISM-Calc*, we can follow an alternative approach based on counting interference fringes to calculate the cavity thickness. We discussed in Section 3.4.1 that the thickness change between two dark fringes is approx. 230 nm. Therefore, we can estimate the cavity thickness by counting the number of fringes between a non-indented region and the point of interest. We show an example of this in Fig. 4.15a. In principle, we do not know whether the cavity thickness is increasing or decreasing from one interference image alone. However, by looking at multiple of these images taken at different wavelengths of illumination, one can see in which direction the fringes are moving. If the wavelength is increased, the dark fringes will move towards areas with higher cavity thickness. We think that the measurement uncertainty of this approach is approx. 115 nm (half of 230 nm) because we can look at interference images at different wavelengths and estimate if another interference fringe would form when changing the wavelength. Although 115 nm measurement uncertainty is very high compared to the 3 nm uncertainty which we estimated in Section 3.4.5, this high uncertainty only applies to very high displacements and steep gradients in thickness, so that the relative error is in the range of 20%.

At present, estimating the cavity thickness directly from the interference images by counting fringes has to be done manually. However, in our lab we are currently working on an automatised algorithm which detects the fringes at one wavelength and uses this information to calculate the cavity thickness with a measurement uncertainty well below 115 nm[15]. A striking benefit of this approach is that much fewer interference images are required, probably only 2-3, to estimate the cavity thickness. This drastically improves the frame rate to below 10 Hz. Therefore, this approach is suitable for measuring moving organ-

[15] Code developed by Dr. Jan Murawski.

isms, e.g. larvae of a fruit fly, where instead of nanometre precision fast image acquisition is most important.

Following the manual approach, i.e. counting fringes by hand, we estimated the maximum indentation of 64 different astrocytes. Using *ERISM-Calc* we also calculated the maximum indentation for 43 microglia. We compare the distributions of the maximum indentation of both cell populations in Fig. 4.15b. It is obvious that the astrocytes are significantly stronger. The median value of the maximum indentation is approx. 16 times higher for the astrocyte population compared to the microglia population.

We note that all the astrocytes we investigated show an epithelial like morphology, i.e. the cell area is very big and the cells look very flat (cf. Fig. 4.10a). We do not observe star shaped astrocytes with many processes. This is consistent with what has been found by Moshayedi et al. who observed that primary astrocytes change their morphology according to substrate stiffness, with cells on stiffer substrates, (> 100 Pa), showing an increase in cell area[123]. Although the results of the authors suggest that the mechanical environment and therefore probably also the applied forces are tightly linked to processes in the cell, up to our knowledge, there are no publications on the forces astrocytes exert on substrates.

Our results indicate that astrocytes are surprisingly strong, at least when they show a fibrous morphology. By contrast, microglia are 16 times weaker.

We visualise this difference by seeding astrocytes and microglia on the same microcavity. Figure 4.16 shows astrocytes and microglia side-by-side. Although we choose a slightly weaker astrocyte for which we could calculate the vertical displacement with *ERISM-Calc*, we still observe a pronounced difference between the two different cell types. This is interesting as it shows that different cell populations can be distinguished by the forces they apply. In this case, the two different cells also show a different morphology in the phase-contrast image, however, there might be examples where this is not the case, possibly when tumour cells and healthy cells are compared. Because large differences in vertical displacements are already visible in one single interference image, ERISM could prove to be an effective tool for online screening of cells.

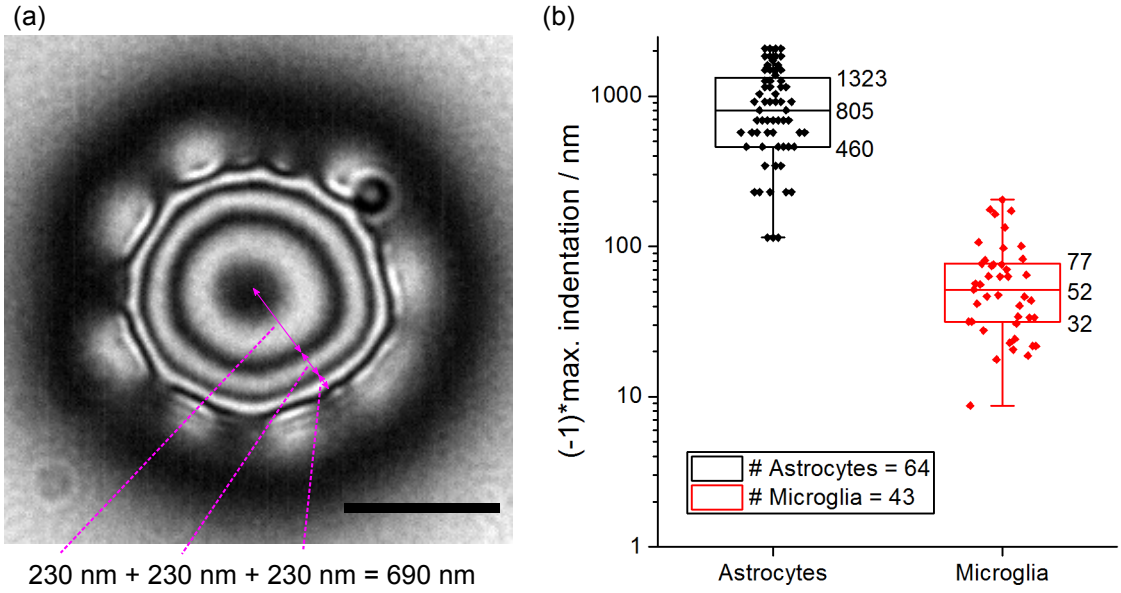

Figure 4.15: (a) Interference image of an astrocyte recorded at 650 nm wavelength of illumination. For each gap between two dark fringes the cavity thickness changes by 230 nm. Scale bar, 50 µm. (b) Comparison of the maximum indentation between astrocytes and microglia. Maximum indentation values for the astrocytes were obtained by counting interference fringes as indicated in (a). Values for the microglia were calculated with *ERISM-Calc*.

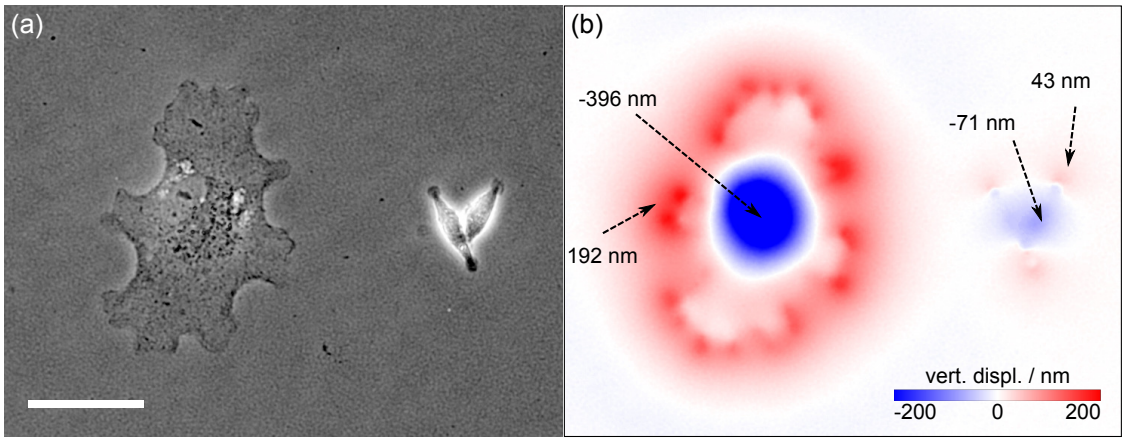

Figure 4.16: Astrocyte and microglia side-by-side. (a) Phase-contrast image. (b) Corresponding ERISM displacement map. The values for maximum and minimum vertical displacement for each cell type are highlighted in the image.

In summary, in this section we showed that we can detect forces applied by astrocytes and microglia on an ERISM micro-cavity. We found that astrocytes strongly deform the micro-cavity indicating a strong reaction to a different mechanical environment compared to in vivo cells. We did not record sufficient data to show significant differences in the forces microglia exert when they are present in different states, and, whether or not there is a difference is speculation at this stage. Nevertheless, ERISM proved to be able to easily measure by how much microglia deform the ERISM substrates. In fact, we also successfully performed more detailed studies on human macrophages which are similar to microglia[77].

4.4 Axon Growth of Neurons from Dorsal-Root-Ganglia

4.4.1 Motivation

Sensory neurons from DRG are a widely used model system to study neuron degeneration and the influence of chemical cues on axon growth to facilitate regeneration[156]. DRG are very well defined areas of tissue which are relatively easy to access in embryonic, postnatal, and adult animals[97].

Many groups have investigated the regeneration of axons after axotomy[16][157–159]. It is well known that neurons of the CNS will usually not show axon regeneration but undergo cell death after axotomy[160–162]. By contrast, neurons of the PNS show a high rate of regeneration supported by the increase in metabolism in the cell body[159]. Hence, investigating why neurons in the PNS show a superior regeneration after axotomy over neurons of the CNS could lead to new insights in how we can support the regeneration process of axons which were damaged by injury or neurodegenerative diseases. Many groups have investigated the influence of electrical[163] and biochemical cues[164, 161] on axon regeneration in the CNS and PNS. It is known that in DRG neurons, axotomy triggers, e.g. by the sudden ion influx, a specific gene expression response to facilitate regeneration of the axon[165].

In addition, different groups have observed morphological differences between healthy DRG neurons and neurons after axotomy[91, 166]. Whilst healthy neurons showed extensive branching of the axon, injured neurons grew mostly only a single thicker branch with a larger growth cone. These observations suggest that regeneration of axons might be adapted to the different mechanical environment, as a single growth cone might be stronger and therefore more capable of growing through the stiffer tissue of an adult animal than what is required in morphogenesis. However, to our knowledge, so far only one group has published results on the mechanical forces growth cones of DRG neurons exert during neurite outgrowth[67, 68]. The authors performed TFM measurements on individual growth cones of DRG neurons and neurons from the hippocampus of postnatal rats. Although Polackwich et al. were able

[16] Cutting off of the axon e.g. with laser light.

to measure multiple growth cones of DRG neurons with a time resolution of 2 s over 30 min, the authors report that many growth cones retracted because of the photo-toxic effect on the cells due to the almost continuous illumination with the fluorescence light source[68].

The work in this chapter shows that ERISM could be an alternative for more detailed mechanical investigations of neurite outgrowth over extended periods of time. We investigated two very different processes: first, the outgrowth of a highly branched axon from the cell body, and second, the movement of a single but larger growth cone. In both experiments we measured over hours with a time resolution well below 1 min.

4.4.2 Axon Branching

Experiment

Multiple DRG were extracted from 2 days old mouse pups[17]. After preparing a cell suspension from the DRG, cells were seeded at a density of 5,000 cells per square centimetre on an ERISM micro-cavity with apparent stiffness of $E' = 3\,\mathrm{kPa}$. Before cell seeding the micro-cavity was coated with poly-D-lysine ($5\,\mu\mathrm{g\,mL^{-1}}$, in H_2O) for 2 h and then with laminin ($10\,\mu\mathrm{g\,mL^{-1}}$, in PBS) for 2 h. The cell culture medium contained:

Component	Final concentration
Neurobasal medium	1X
GlutaMAX^{TM}-I Supplement	2 mmol
B-27$^{®}$ supplement	2vol%

The cells were allowed to attach for two hours in the incubator before transfer to the ERISM setup. We took measurements every 36 s over 18 hours. This was necessary to investigate the neurite outgrowth from the very start until the processes start to show branching, as we could not tell in advance when cells would start to grow neurites and which cells would show neurite growth rather than migration or potentially cell death. The cell we show in the following started with neurite outgrowth approximately four hours after we started the measurement.

[17] Dissection and preparation of the cell suspension was performed by Dr Andrew Morton who is a member of the Gatherlab.

Data-Analysis

We applied an image stabiliser algorithm[167] to the phase-contrast images to correct for lateral drift. We saved the transformation for each time frame and applied the same transformation to the corresponding ERISM maps.

We will see later that the growth cones we investigated only generated vertical displacements up to 4 nm. However, the roughness of the sensor was about 2 nm. In order to detect the small deformations more clearly, we applied a different background correction scheme than described in Section 3.4.4. As a reminder, usually, we construct a background plane from areas where no cells exert forces. This works well to remove the absolute thickness of the sensor. However, the sensor surface roughness is not taken into account by this approach. Since we wanted to observe neurite outgrowth into an area were no cells are, we used the undeformed area from an early frame as a reference image and subtracted this from the following time-lapse data. To reduce noise in the background plane, we built the average over 50 images taken before the neurites grew into this area. This is comparable to taking a zero-force image in TFM but for the present experiment does not represent a limitation or require extra work as the undeformed ERISM map is recorded anyway. In addition, this form of background correction is only needed if the noise needs to be reduced below 2 nm.

For comparison, we applied both types of background corrections to an area without displacements from cells, i.e. only the surface roughness should be the cause of measured vertical displacements (cf. Fig. 4.17). We find that for this sensor the surface roughness is around ±2 nm. By subtracting the average over 50 images of previous time frames we can decrease this value by a factor of four to ±0.5 nm.

Finally, we applied a Gaussian smoothing filter with a standard deviation of two pixels in all three dimensions to the vertical displacement. This did not appear to smooth out any features but significantly improved the signal to noise ratio.

We test how well we can investigate the forces different growth cones apply on the substrate by tracking the indentation for 12 growth cones over time. We only investigate the pushing as the maximum pulling is smaller because it spreads more over the substrate (cf. Fig. 4.18). We measure the indentation each growth cone applies in the following semi-

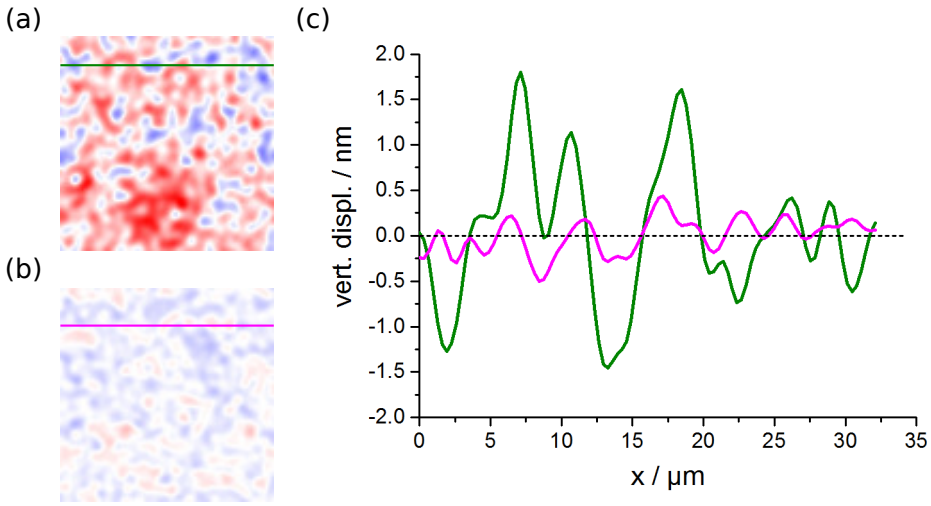

Figure 4.17: Comparison between vertical displacement obtained by (a) subtracting a background plane and (b) by subtracting a zero-force image for a region of the image with no growth cone present. Image size is 32 x 32 µm. Colour scale as in Fig. 4.18. (c) Profiles as indicated in (a) and (b).

manual way: Having the time-lapse phase-contrast and vertical displacement data side-by-side we manually track the position of each growth cone in reverse time order. We define the position of the growth cone as the point where we see the maximum indentation.[18] We then measured the mean value of indentation across a circle with a diameter of 3 µm at the selected point for each time frame. The spatial averaging is done to reduce the noise further and to compensate for small variations caused by the manual tracking. We follow each growth cone back to the cell soma which means that we collect the same data for growth cones before branching multiple times. This confirmed that our method works well as the traces are very well reproduced for these sections.

Results

Following the above procedure we obtained the time-lapse data for a cell which started growing an axon which then split into multiple branches. In Fig. 4.18 we picture different time points of this process. We can see that the cell starts to grow very thick processes. These processes branch multiple times and we can see that different branches apply different

[18] In case there is no indentation visible, we chose the position to be just behind the edge of the growth cone (inside the growth cone), which is where we observe the maximum indentation to be when it is visible.

vertical displacements. It seems that branches that appear thicker in the phase-contrast images also exert stronger forces. This is for instance visible for the image at 163 min in Fig. 4.18 where the middle branch is thicker than the the branches to the left and to the right and where this branch is also the strongest. In addition, we observe that the entire middle branch and not just the growth cone indent into the substrate. This could be a result of a potentially higher stiffness of the branch due to possibly more microtubule and actin filaments. Once it is getting thinner, also the indentation decreases (compare the images at 163 min, 216 min, and 317 min in Fig. 4.18).

We did not apply staining to prove that the neuron we were investigating was indeed a sensory neuron, however, the morphology of the branches leads us to believe that it was, because the morphology is very similar to what was observed by other groups[168, 91, 166].

In Fig. 4.19a we show the last phase-contrast image of the series and highlight the branches we traced. We only traced growth cones which continued growing after we stopped the ERISM measurement; some growth cones stop growing, e.g. because they are blocked by other neurites. Fig. 4.19b shows the actual positions we marked at each time-step. This results in a picture similar to the branches in Fig. 4.19a, but not exactly the same, because growth cones might grow and retract in different directions before extending to the branch which is visible in the end in Fig. 4.19a. Furthermore, we labelled each branch with a number according to the following convention: Every time a process branches we add another digit. Branches which are most left get a ”1” added, the next branch to the right gets a number ”2” and so on. This means for instance the branch ”122” originates from the main branch ”1” (like all other) and then from the second branch ”12”. It also means that ”12” only reaches from the knot where ”1” separates into ”11”,”12”, and ”13” until ”12” branches further.

Following this convention we show the vertical displacement of each branch over time (cf. Fig. 4.20). For the traces which we measured multiple times (e.g. trace ”1”), we built the average of the corresponding measurements. In addition, we show the mean value of the values in a circle with a diameter of 2 µm at a position where no forces are exerted (similar to how we measured the traces of the growth cones). This shows that the noise over time is around ±0.5 nm and comparable to the lateral noise. We can see from the displacement

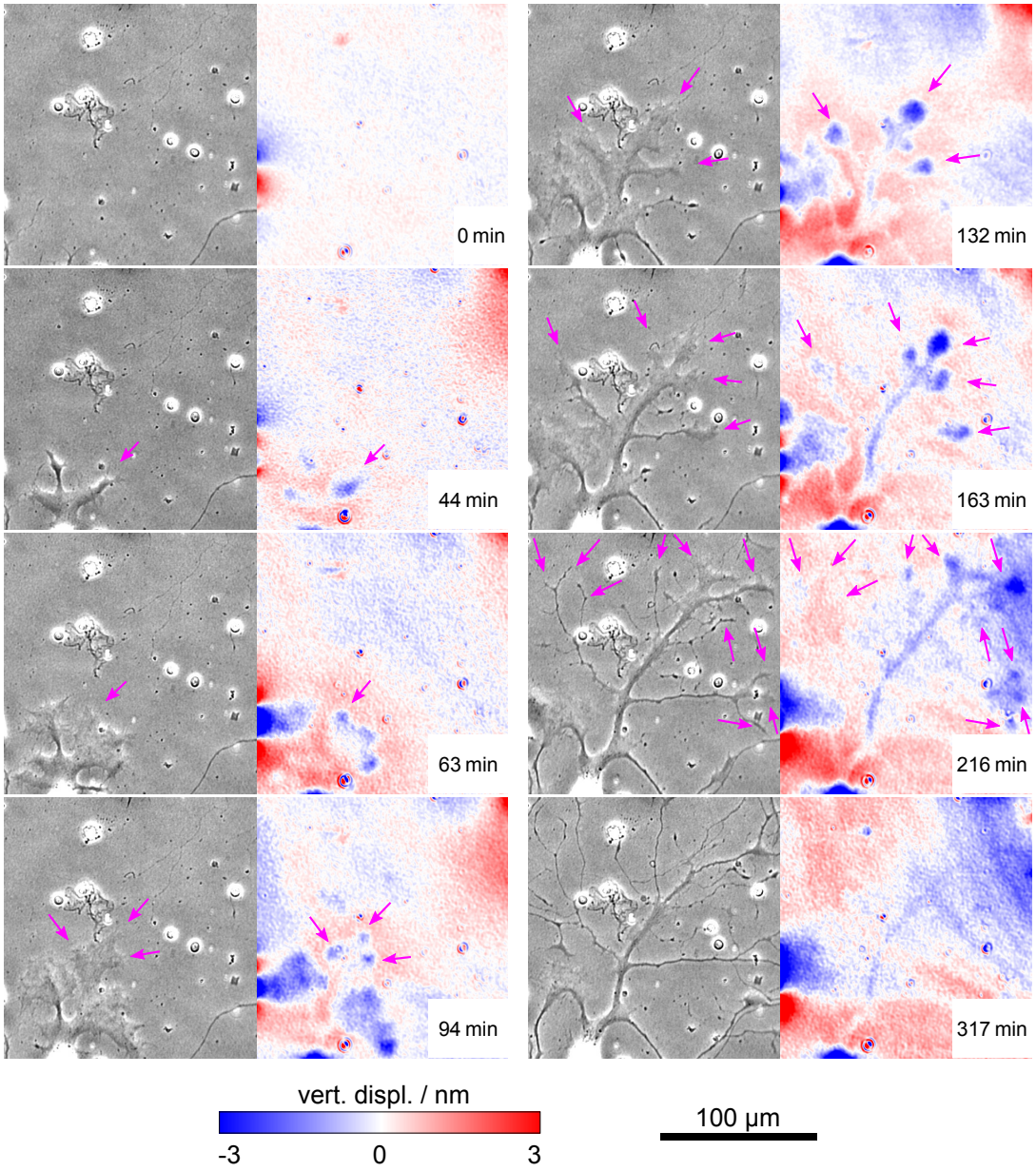

Figure 4.18: Phase-contrast and vertical displacement images at different time points of the experiment. The Magenta arrows highlight the branches we investigated and help to associate branches in the phase-contrast images with displacements in the vertical displacement maps.

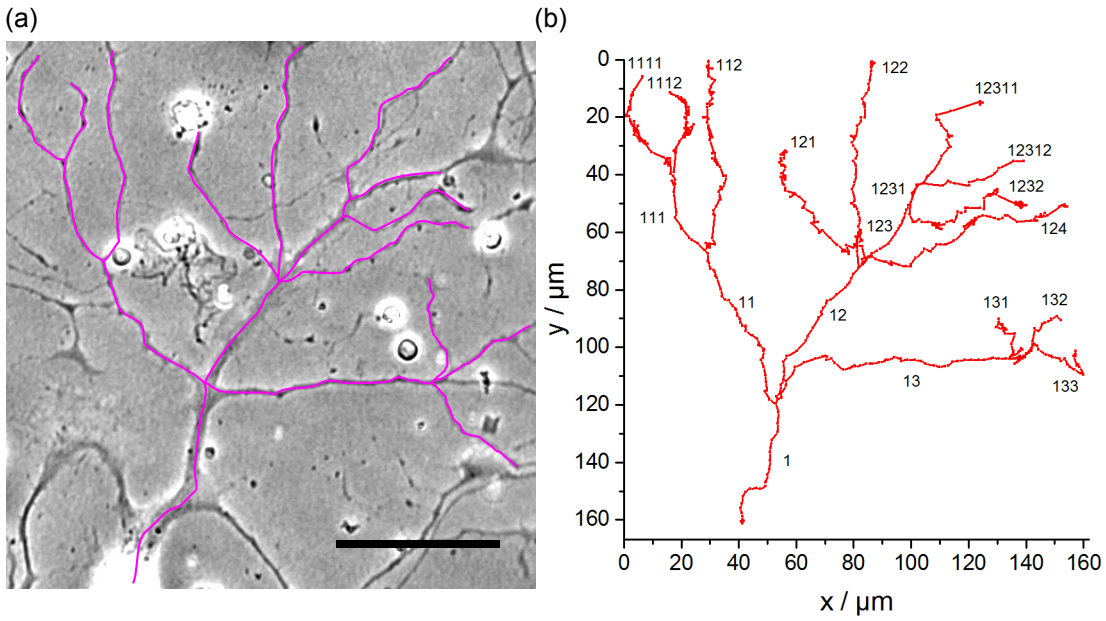

Figure 4.19: (a) Phase-contrast image of the branches at the end of the experiment. Magenta lines highlight the branches we investigated. Scale bar, 50 µm (b) Measurement points of the neurite tracking with neurite labels as described in the text.

maps in Fig. 4.18 and the traces in Fig. 4.20 that the growth cones do exert forces which lead to displacements well above 0.5 nm, up to 3.5 nm. However, on the other hand it is difficult to assess whether the variations on a time scale of below 15 min are noise or actual fluctuations of the growth cones.

We can see that in most cases, before the splitting into multiple daughter branches happens, the mother branches often show increased activity, i.e. higher indentation. This is difficult to evaluate precisely because determining when the actual branching event happens is somewhat ambiguous. We defined these events as the times just before we saw distinct shapes in the pushing pattern, that is, one would not see a single pushing any more but e.g. two or three pushing sides. This might be an indication that the focal adhesions of the individual daughter growth cones might all originate from the same focal adhesion of the mother growth cone.

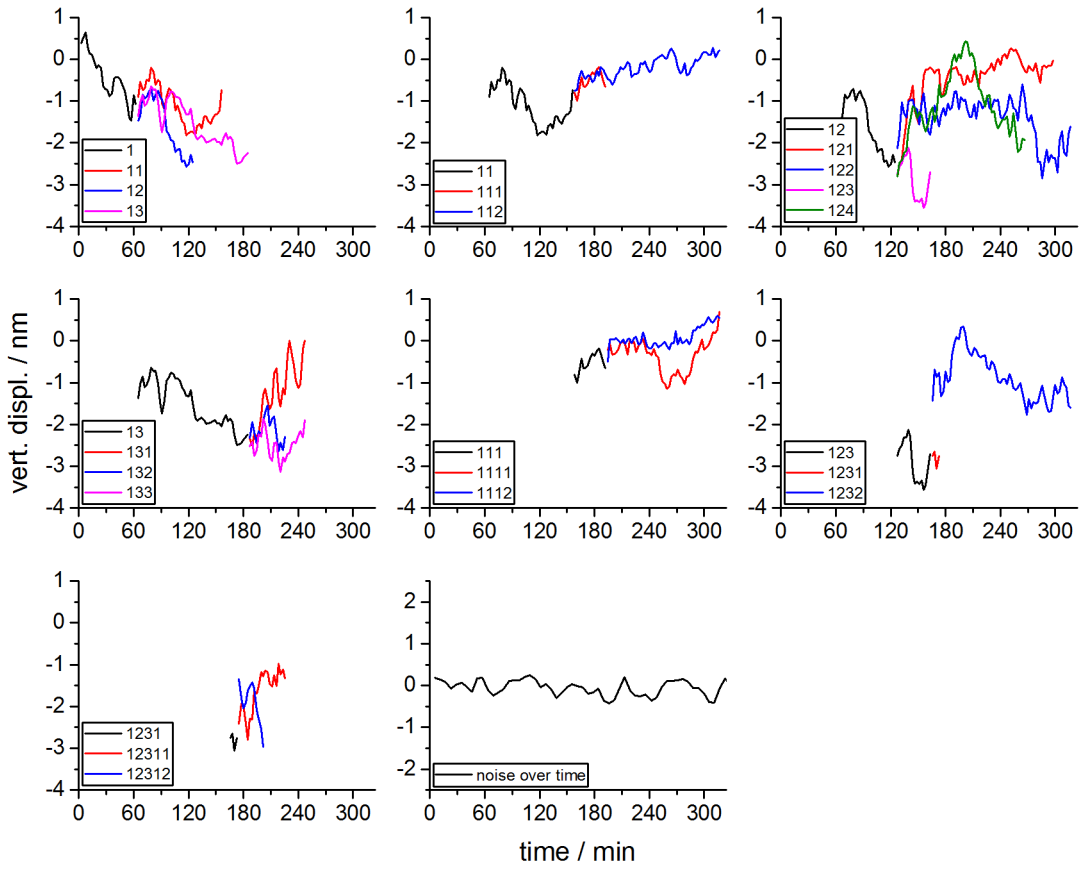

Figure 4.20: Vertical displacement over time for each of the branches. Branches are grouped such that the mother and the daughter neurites of the next generation are visible in one plot. Daughter neurites which become mother neurites are shown in two different plots, once as mother neurite and once as daughter neurite. Last plot (second column, third row) shows a representative example of the noise over time for an area without vertical indentation caused by cells.

4.4.3 Single Growth Cone

Experiment

Three days after we measured the branching of a DRG neuron we observed a single bigger growth cone and tracked it over 8 h taking an ERISM measurement every 3.5 s. We did not measure the whole cell which is why it is difficult to assess whether this was a DRG neuron or possibly a motor neuron from the spinal cord. The morphology seems to be very different, it is a single long axon with a bigger growth cone. Other groups have investigated the morphology of DRG neurons after removing the axon (axotomy) and found that the regenerated axon will show significantly less (to none) branching and bigger growth cones[168, 91]. Although this is speculation, it is possible that the growth cone we investigated here originated from a neuron with a damaged axon.

Data-Analysis

The vertical displacement was calculated as described in Section 3.4.4. Again, we subtract the background by building the average of several time points where no displacement is exerted by cellular structures. However, this yielded less good compensation for the roughness than before (cf. Section 4.4.2), as the focus drift was stronger. Therefore, we applied a Gaussian smoothing in lateral direction (space domain, not time domain) with standard deviation of 4 pixels to remove the pattern of the roughness. This is reasonable as the deformations for this dataset are fairly broad and the smoothing reduces the peak displacement values by less than 10%.

We then extracted the maximum and minimum displacement in the following way: We used the *Imagej* plugin *MTrackJ*[147] to first track the maximum and then the minimum indentation over time. This yielded the vertical displacement, the time point, and the lateral coordinates. In addition, we calculated from the lateral coordinates at each time point the lateral velocity of the points were maximum pushing and pulling occurs.

Results

In Fig. 4.21 we show the phase-contrast images and vertical displacement maps for six different time points. The green arrows have the same position in the corresponding images. We can see that in the beginning the growth cone is advancing (0 h to 0.6 h) and after 1.7 h it starts to retract but advances again between 4.0 h and 7.9 h. In addition to the main growth cone (indicated by the green arrows), we can also see other structures in the images. In fact, there is another motile growth cone to the lower left of the big growth cone, and we observe some smaller deformations for this one as well, e.g. at 1.7 h where we can see another pair of less pushing and pulling compared to the stronger growth cone (magenta and green arrows , respectively). The other visible structures are occasionally exerting forces as well, however all structures are significantly weaker than the growth cone we investigate in more detail. We therefore think that the displacements from the other structures are interfering only very minor with our data and can be neglected for the further analysis.

This dataset is a very clear example that our ERISM micro-cavities deform in vertical direction under lateral stress. In Fig. 4.22 we show a cross-section of the vertical displacement for the frame at 0.6 h from Fig. 4.21. Growth cones are usually not thicker than 1 µm[92], hence, for geometrical reasons it is unlikely that the displacements we see here are the result of a vertical force. More likely, the in-plane traction causes the stiffer surface of the micro-cavity to indent (or pull) into the elastomer. We discussed this in detail in Section 3.5.4 and demonstrated how we can correlate the vertical displacement with a lateral force.

The images in Fig. 4.21 show that the pulling seems to occur close to the leading edge of the growth cone. We think that the point where the force is applied has to be between where the indentation profile passes zero and where the maximum (positive) vertical displacement is visible. The direction of the force should be parallel to a line connecting maximum pulling and pushing. The force also has to act parallel to the axon so that it can be compensated by the cell body. This is indeed what we observe in Fig. 4.21: the line between pulling and pushing is parallel to the axon in all images.

It is worth noting, that the big growth cone is possibly guiding the smaller growth cone (left) to another neurite coming from the right. At 0 h there seems to be no connection,

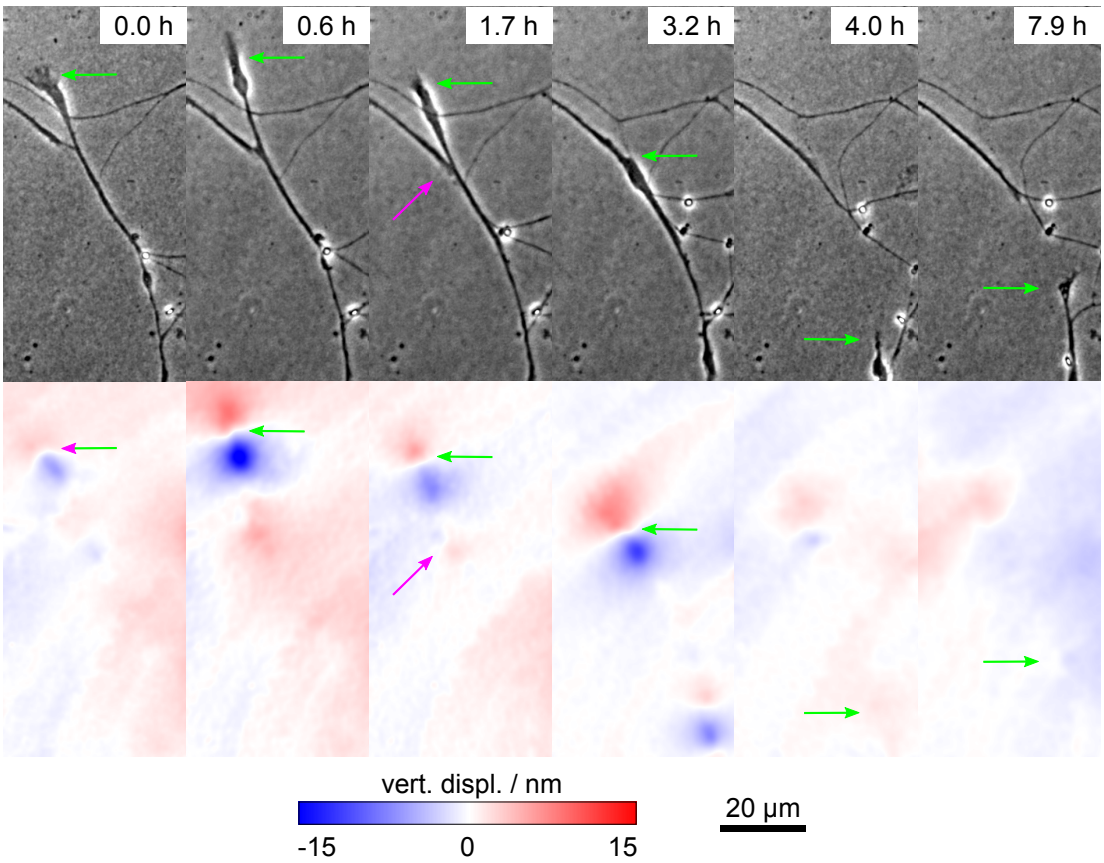

Figure 4.21: Representative time points of data showing a growth cone advancing and retracting. The green arrows are reference points between the phase-contrast images and vertical displacement images.

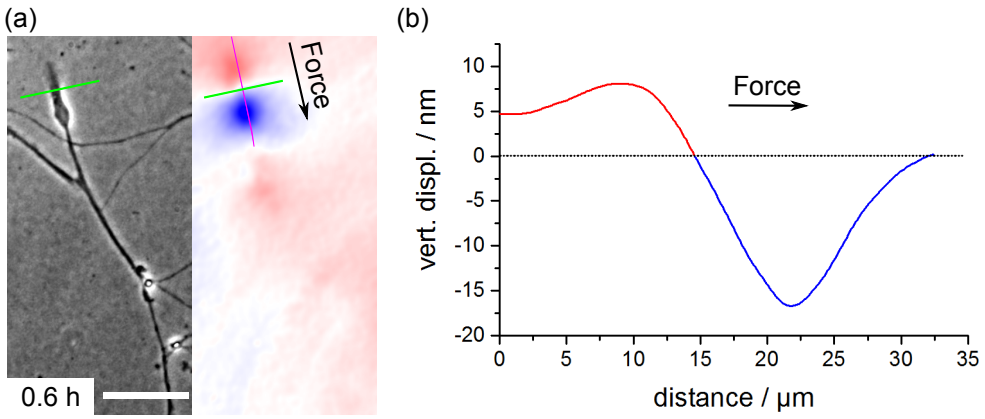

Figure 4.22: (a) Phase-contrast and vertical displacement image for a single growth cone. The green line is at the same position in both images. Scale bar, 20 µm. (b) Profile extracted at magenta line in (a).

then the bigger growth cone and the smaller one seem to be connected with each other at 3.2 h, and in the images from 4.0 h until the end of the experiment there seems to be a stable connection between this smaller growth cone and a neurite coming from the right.

We summarised our results of tracking the vertical displacements of the growth cone over time in Fig. 4.23a. We only tracked the extrema for maximum and minimum vertical displacement until 4.0 h as the growth cone was retracting out of the field-of-view afterwards. However, it extended again at a later time point (cf. last image in Fig. 4.21). We can see that overall the absolute values of the pushing are higher than the pulling. This is most likely because the pulling spreads over a larger area compared to the pushing (cf. Fig. 4.21). The total vertical displaced volume, and therefore the vertical force, should be zero as otherwise the the system would not be in equilibrium (assuming the elastomer is incompressible). Although we did not measure the displaced volume, the traces of pulling and pushing over time seem to counterbalance each other, that is, if particularly strong pulling (red, positive values) can be seen at a specific time point, the pushing (blue, negative values) increases as well.

In order to summarise the total movement of the growth cone, we calculated the distance between the position of the maximum indentation at 0 h and the following time points (black line in Fig. 4.23a). As described before (cf. Fig. 4.21), we can see a slight extension of the growth cone in the beginning, then it retracts a bit and maintains its position over approximately 2 h, finally, it significantly retracts until 4.0 h which can be seen at the constant decline of the black line in Fig. 4.23a.

Because of the long measurement time the details of how big the vertical displacements are at shorter time scales are not visible in Fig. 4.23a. Therefore, we show a close-up of the pushing over 10 min in Fig. 4.23b. The noise (magenta line) alternates between 0.5 nm and −0.5 nm. Clearly, the maximum indentation shows changes of more than 10 nm over longer times, e.g. around 5 min (cf. Fig. 4.23b), but also shows smaller changes of about 1–2 nm (i.e. clearly above the noise level) which happen faster than 30 s (cf. Fig. 4.23b).

Finally, we investigated whether the forces (or vertical displacements) are correlated with the speed of the growth cone. We calculated the speed from the distance between the

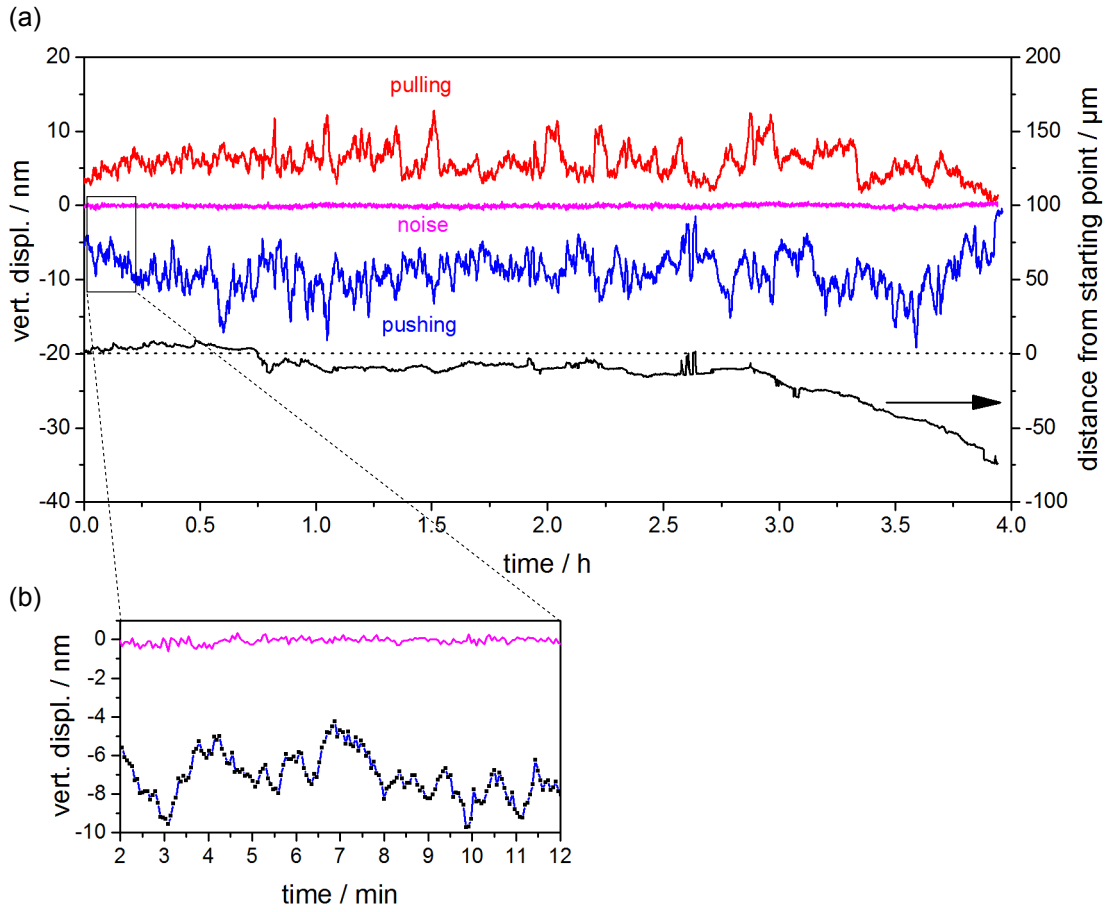

Figure 4.23: Results of tracking maximum pulling and maximum pushing of a growth cone over time. (a) Vertical displacement for maximum pulling (red), maximum pushing (blue), and noise (magenta) at a position where no forces are exerted by growth cone. All three lines correspond to the left axis. Black line, distance between the position of maximum pushing at 0 h and at successive time points, corresponding to the axis at the right. (b) Close-up of maximum indentation and noise level over 10 min. Black squares indicate the actual data points, blue lines drawn as guide to the eye and corresponding to (a).

position of the maximum indentation of adjacent time points divided by the measurement time interval of 3.5 s. We smoothed the data for the maximum indentation and the calculated growth cone speed with a moving average filter with a time window of 5 min which removes the high frequency variations but leaves slower changes in position. The two curves are compared in Fig. 4.24a. Apparently, both curves follow a similar shape, if the speed shows a peak, in most cases, also the maximum indentation shows a peak, which means that at higher growth cone speeds the exerted force is lower. This observation is consistent over the 4 h.

We visualise this further and plot the vertical displacement (multiplied by −1 because stronger indentation corresponds to higher force) against the growth cone speed (Fig. 4.24b). Overall we find what is suggested by Fig. 4.24a, that the stronger the force, the lower the growth cone speed. The values are spread, but they are not randomly distributed. The colour of the data points in Fig. 4.24b indicates when the measurement was performed. With this colour scale we can see that the data points are forming paths indicating that the history of growth cone speed and applied force is important for possible speed-force combinations.

4.4.4 Discussion

These experiments show that ERISM can be a valuable tool to investigate different forms of axon growth. To the best of our knowledge, the forces involved in neurite outgrowth at such an early stage (branching data) have not been investigated so far. The challenge of such an experiment is that it is difficult to know in advance which cells will migrate, show neurite outgrowth or maybe even die. In addition, the branching may span a large area which requires either tracking individual growth cones, having a wide-field setup with low magnification, and/or tacking measurements at different points to stitch the images together. We therefore argue that ERISM is inherently well suited for such experiments because we can observe large fields of view over extended periods of time using, e.g. a 20x objective and measuring at multiple positions.

Up to now, the only force measurements on growth cones of dorsal root ganglia neurons have been reported by Koch et al. and Polackwich et al. (same group)[67, 68]. Polackwich et

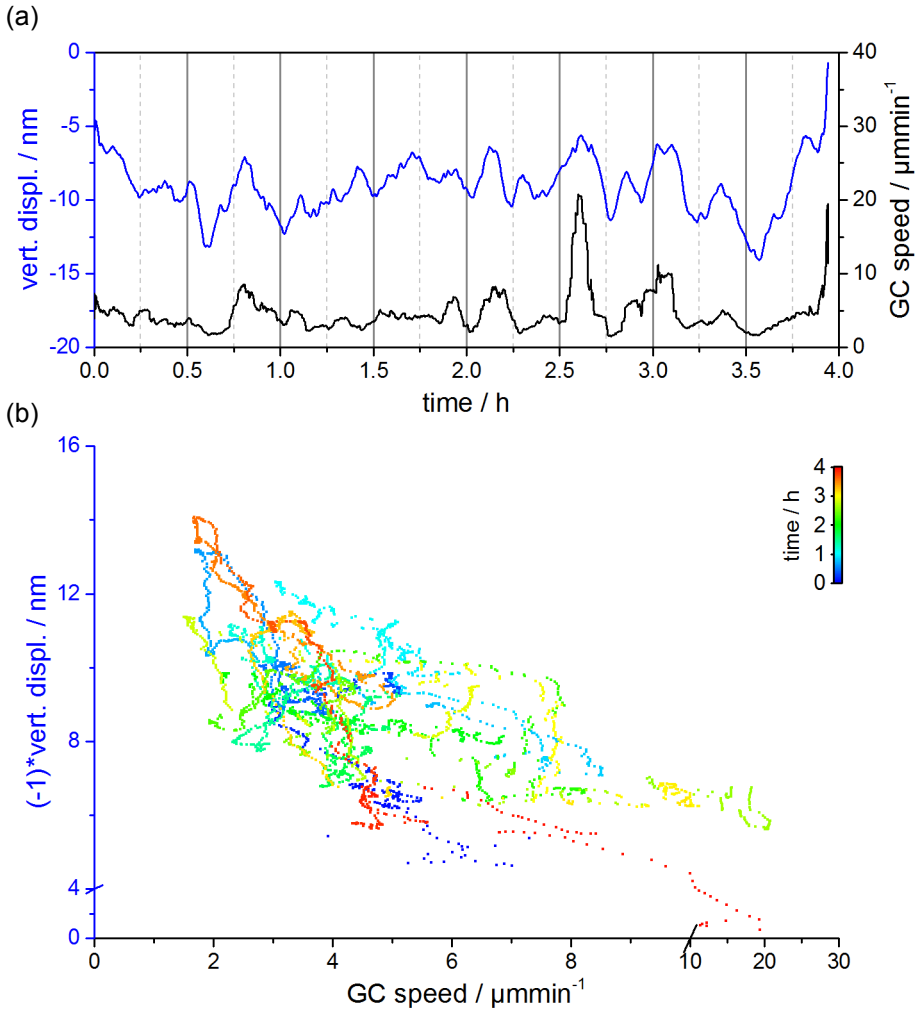

Figure 4.24: Correlation of growth cone (GC) speed and vertical displacement. (a) Vertical displacement (blue) and GC speed (black) over time. (b) Vertical displacement over GC speed. The colour scale indicates the time of each data point.

al. recorded images for 30 min in 2 s time intervals. This required almost continuous illumination with a fluorescence lamp and the authors observed that many processes retracted in response to this illumination. This highlights the limitation of TFM for the investigation of such structures with high time resolution. These problems can be overcome by ERISM. Because of its inherently low light power we are able to take measurements in time intervals of 2 s over hours to weeks[77]. In the experiment discussed above (branching) we seeded the cells at a relatively high density, and the deformations of the micro-cavity by neighbouring cells prevented us from observing the outgrowth over a longer time. Nevertheless, this problem could be easily fixed so that ERISM could be used to observe neurite outgrowth of multiple cells over weeks.

Interestingly, we found indications that growth cone forces increase before branching occurs. It would be reasonable that at some point before branching the force is a superposition of the newly formed growth cones of the daughter branches. Further measurements of the forces before branching may provide insight into when the main branch commits to splitting into multiple branches.

It is known that one purpose of the growth cone is to generate tension in the axon and this tension is known to facilitate vesicle transport[169–171]. In our experiment we observe that the branch in the middle (”12”, cf. Fig. 4.19b) exerted the largest force and is at that time also the thickest branch. This suggests that also the tension inside the neurite might be higher. Moreover, this branch also had the most daughter branches. Therefore, our results support the findings of other groups that axon tension facilitates axonal transport, possibly to favour outgrowth of the neurites with the higher tension.

We also observe other growth cones which apply significantly higher forces than the growth cones of the cell were we observed branching. At present, we do not know whether the growth cone we investigated originated from a DRG neuron, or if it was potentially a motor neuron from the spinal cord due to a possible mixture of spinal cord neurons and DRG neurons during the dissection. However, it is also possible that it was a DRG neuron but has been damaged before. Different groups reported that growth cones originating from DRG neurons where the axon has been cut off are larger and the axon shows less branching

compared to axons/growth-cones from healthy neurons[168, 91]. It is likely that larger growth cones exert stronger forces as in total there are more actin-myosin connections to generate traction. This would align well with our observation and provides a great starting point for further investigations.

In addition, we observed that there is a negative correlation between growth cone speed and traction force. Moreover, the actual growth cone speed and applied force seem to depend on the history of the growth cone. To our knowledge, this has not been reported so far and could have interesting implications on how adhesion complexes are generated and maintained during migration.

Whilst observing the movement of the single growth cone, this growth cone also interacted with other growth cones and neurites. We can basically extend the measurement time to several days or weeks, thus, ERISM could potentially be used to study the mechanical aspects of synapse formation, a process which usually takes more than one week[172, 173].

With the conversion factor we calculated in Section 3.5.4 we can convert the vertical displacements we measured in this section into corresponding lateral forces. The vertical displacement to lateral force conversion factor is $4.7\,\mathrm{nm\,nN^{-1}}$. For the branching data, this results in forces up to almost 1 nN and for the single growth cone around 3 nN . Koch et al. measured forces of DRG neurons (rat) of approximately 0.5 nN after 3–10 h and 1.5 nN after 20–30 h. These values are comparable to our results and even indicate that the difference in forces between our first data set (branching) and the single growth cone might be related to the time the cells were in culture.

The forces of the DRG growth cones (branching) are very small and are just above the noise level in our data on outgrowth and branching of neurites. We think that the noise present in our data mainly originates from the shift in focus during the measurement. This focus shift disturbs the drift correction for lateral image stabilisation which is why the background subtraction does not lead to optimal results. We are confident that we can further reduce the noise by upgrading the setup such that it is more resistant against thermal fluctuations which lead to lateral and vertical drift.

In conclusion, we could successfully demonstrate that we can detect very weak and purely horizontal forces with ERISM. Thus, our experiments prove that ERISM can be used to study the mechanics of neuronal growth cones that involve systematic manipulation of the proteins of the cytoskeleton and mechanosensitive ion channels.

4.5 Human Neural Stem Cells

4.5.1 Biological Background

Stem cells are the origin of all cells in the human body. They have the remarkable capability to differentiate into all kinds of different specialised cells in the human body (e.g. blood cells, neurons, fibroblasts, etc.). In addition to their pluripotency they can also proliferate without differentiating which is known as self-renewal. These features make them excellent tools for developmental studies[174] but also to serve as a source of specific human cells without a reoccurring need for a donor. Moreover, stem cells are promising candidates for new treatments for a wide variety of diseases. In fact, bone marrow transplants are a form of stem cell therapy that has been successfully used for years now to treat, for instance, leukaemia.

In this chapter we will look at human embryonic neural stem cells (hNSC). Neural stem cells are a type of stem cell which is already specialised to some extent and which can only differentiate further into specific cells found in the human brain; differentiating them e.g. into epithelial cells would not work. The cells used in this work were grown from embryonic stem cells which were obtained from blastocysts 4-5 days after fertilisation. HNSC can be differentiated into neurons, astrocytes, and oligodendrocytes by changing growth media and substrate coating (cf. Fig.4.25).

4.5.2 Motivation

Whilst the pluripotency of the stem cells is why stem cells are so appealing for different research areas and medical treatments, this is also what makes their application difficult if specific cell types are required. Stem cell fate (or stem cell lineage choice) is a highly complex process which depends on the chemical and mechanical environment[175]. Therefore, understanding how to guide stem cells in their lineage choices towards the desired target cells is a field of intensive research.

Especially if stem cells are to be used for in vivo stem cell therapies in humans, predicting and controlling the lineage choice is crucial[176, 177]. In vitro the biochemical and

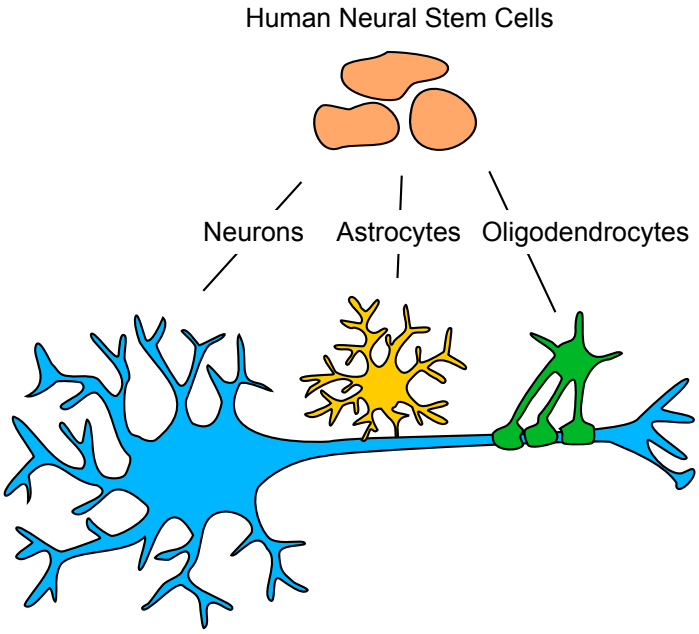

Figure 4.25: Human neural stem cells which can differentiate into neurons, astrocytes, and oligodendrocytes.

biophysical environment can be controlled very well, this is not the case in vivo. Thus, it is important to precisely understand the pathways which lead to specific lineage choices of stem cells so that differentiation can be directed in the most efficient way, e.g. by blocking specific receptors whilst adding growth factors, or even genetically modifying the cells such that they will only be receptive to certain stimuli.

Much research has been done on the biochemical pathways of lineage choice, especially on the influence of growth factors and ECM proteins[175]. Since over a decade, researchers are aware of the importance of the stiffness of cell culture substrates used in stem cell experiments, this has been shown to be an additional factor in stem cell lineage choice[9, 10, 178, 18, 179–181]. When stem cells differentiate, they often change their morphology. This raises the question if, in return, prescribing cell shape can induce differentiation[182]. Indeed, different groups forced cells into specific shapes and observed a tight link to lineage choice[183–186]. These results suggest that stem cells sense their own shape and use this as additional input for specification.

The influence of substrate rigidity and cell shape on linage choice suggests that tension in FA, in the cytoskeleton, and in the cell membrane is coupled to gene expression related to

stem cell differentiation. Currently, the Rho/ROCK pathway has been reported to be a crucial part of this process[15, 18, 187, 182]. In addition, in FA integrins are particularly important for mechanotransduction[188] and β1-integrins are suggested to play a significant role in stem cell linage commitment or maintenance[189]. Integrin signalling has also been linked to epidermal growth factor (EGF) receptor activity[190–192].

Moreover, Ca+ signalling is known to regulate gene expression to guide stem cell differentiation[193, 194]. Pathak et al. investigated the role of the stretch-activated ion channel *Piezo1* in lineage choice of human neural stem/progenitor cells (hNSPC). The authors found that neurogenesis decreases by 45% upon inhibition of Piezo1, whilst differentiation into astrocytes was increased by 48%. These results suggest that Piezo1 activity, caused by stress, favours neuronal specification in hNSPCs. The authors support these findings with additional data showing that for higher substrate stiffnesses Piezo1 activity and neurogenesis increases. By contrast, but in accordance with the findings of other groups, they found that neurogenesis of neural stem cells which originated from rats decreases with increasing substrate stiffness[178, 195, 187]. Their results highlight that the stress stem cells exert on their environment is indeed linked to lineage choice, however, the authors did not perform any cell force measurements.

Surprisingly, even though these mechanical path-ways have been linked to stem cell differentiation, at present, very little literature is available on the observation of cell forces during the stem cell differentiation process. The shortage of such results may be rooted in the experimental challenge that cells have to be cultivated and measured over days to weeks on the same substrate. This is not possible with TFM, because the cells need to be detached after each measurement, and we only found two publications using the micro-pillar-array method which address this question in neural stem cells (rats)[196] and human mesenchymal stem cells[197]. Furthermore, Shi et al. did not observe any influence of the substrate stiffness on the stem cell lineage choice, which is in contrast to the observation of many other groups mentioned above. Shi et al. attribute this to the very different mechanical properties the micro-pillars provide compared to e.g. hydrogel substrates. More precisely, although the micro-pillar substrates can have an overall stiffness comparable to hydrogels,

the local stiffness is higher (or lower) due to the arrangement of micro-pillars and the gaps between them.

The aforementioned literature highlights that stress generation in stem cells is an important factor in linage choice but also that only few experiments have been carried out to investigate this further. We believe that conducting force measurements during stem cell differentiation could add valuable information to connect biochemical and biophysical cues involved in this complex process. ERISM can measure cell forces without the need to detach the cells during the course of the whole experiment (possibly weeks). Furthermore, it is possible to apply immunostaining to the cell on ERISM substrates, a feature required to assess the differentiation state of the cells and to confirm that differentiation into the expected cell type has actually taken place. Thus, ERISM could prove to be an effective tool to measure forces during stem cell differentiation. Here, we will focus on human neural stem cells and measure how the forces they generate change during differentiation into astrocytes. A process which, up to our knowledge, has not been investigated yet.

With the method and tools developed in the previous chapters, the experimental procedure is straightforward. We cultivated hNSC on an ERISM micro-cavity in a medium used for continuous culturing of stem cells and after two days switched to astrocyte differentiation medium. We measured the displacements the cells apply to the surface of the micro-cavity once before and multiple times after switching to differentiation medium. At the end of the experiment we performed antibody staining to assess if the cells indeed differentiated into astrocytes.

In the following, we will first explain the experimental procedure and how we analysed the data. We will then discuss the results in the light of the literature introduced above.

4.5.3 Experiment

We used *Gibco® H9* derived hNSC from *Thermofisher*. The cell culture was established on plastic dishes with CellStart^{TM} coating following the cell culture protocol of the supplier[19]. The stem cell medium (knock-out medium) consists of:

[19] Rebeca Diaz Vazquez started the initial culture and after passaging an aliquot was transferred to our lab.

Component	Final concentration
KnockOut^{TM} D-MEM/F-12	1X
GlutaMAX^{TM}-I Supplement	2 mmol
bFGF	20 ng mL^{-1}
EGF	20 ng mL^{-1}
StemPro® Neural Supplement	2vol%

At passage number 10 the cells were seeded on a CellStart^{TM} coated micro-cavity with an apparent Young's modulus of $E' = (17 \pm 3)$ kPa. We plated the cells at a density of 20,000 cells per square centimetre on the micro-cavity and also plated cells on a 35 mm cell culture dish. The cells on the micro-cavity and the dish were both cultivated in knock-out medium for two days. Then, the first ERISM measurement was taken with the micro-cavity sample, this measurement represents the data point at 0 d in the following plots.

After this measurement, we switched to differentiation medium for the cavity and the dish to induce differentiation into astrocytes in both cultures simultaneously. The formula for the differentiation medium is:

Component	Final concentration
D-MEM	1X
GlutaMAX^{TM}-I Supplement	2 mmol
N-2 Supplement	1vol%
FBS	1vol%

ERISM measurements were performed 1 d, 2 d, 4 d, 6 d, 9 d, 13 d, 20 d, after switching to differentiation medium[20]. The medium was changed every three days. The cells were placed in the on-stage incubator (37°, 5% CO_2) one hour before the ERISM measurement was performed to avoid any influence on the measurements by the temperature change during transporting the cells from the main incubator in the cell culture lab to the ERISM set-up

[20]The cells on the micro-cavity showed contamination with bacteria or fungi after 18 d. We therefore washed the micro-cavity several times thoroughly with medium containing penicillin and streptomycin. Although the contamination seemed to be gone after this procedure, many cells were removed during the washing. To compensate for the loss of cells, we split the cells in the Petri dish cultivated in parallel, treated with the same medium, and seeded 5,000 cells on the micro-cavity on day 19 and performed another ERISM measurement the next day. As apparent in the phase-contrast image (cf. Fig. 4.26 at 20 d) the contamination was still present and we therefore stopped the experiment after the measurement at 20 d.

(approx. 20 m distance, <1 min at room temperature). For each time point we measured multiple fields of view on the sensor to increase the number of investigated cells.

Therefore, we could not stain the cells on the micro-cavity for astrocyte specific markers. However, we performed staining for *glial fibrillary acidic protein* (GFAP) (primary antibody, rabbit anti-GFAP, Dako; secondary antibody, Alexa Fluor 488® goat anti-rabbit, Life Technologies) on the cells from the Petri dish which have been exposed to the same differentiation medium for the same amount of time as the cells on the micro-cavity. We also stained hNSC for *nestin* (primary antibody, rabbit anti-nestin; secondary antibody, Alexa Fluor 594® goat anti-rabbit; both from Life Technologies) to confirm that most of the cells were still in their undifferentiated state. However, this was done at a later stage with another aliquot of cells at passage number 6[21]. When we seeded the cells on the micro-cavity and the Petri dish, we seeded cells in a cell culture flask for further experiments and observed similar proliferation rates as in the previous passage numbers. Hence, we expect that the majority of cells we used for this experiment were in fact in their undifferentiated state. Furthermore, we tested in an additional earlier experiment — were we differentiated hNSC into astrocytes in a Petri dish — the staining for GFAP. These cells had been in differentiation medium for two weeks and seem not to have produced GFAP, yet. This is indicated by the strong background and unspecific binding, even at the nucleus, of the marker as shown in Fig. 4.30b.

4.5.4 Data-Analysis

In order to measure the strength of the cells at different time points we performed the following data analysis. For each ERISM data set the cavity thickness was calculated and the background subtracted as described in Section 3.4.4. This yielded the displacement maps for each measurement (cf. Fig. 4.26). All the following processing steps are summarised in Fig. 4.27. We used phase-contrast images to draw by hand (in ImageJ) the cell outlines for each measurement (cf. Fig. 4.27a).

[21] The cells originated from the same batch as the cells we used for the ERISM measurements, but were cryopreserved in our lab at passage number 2.

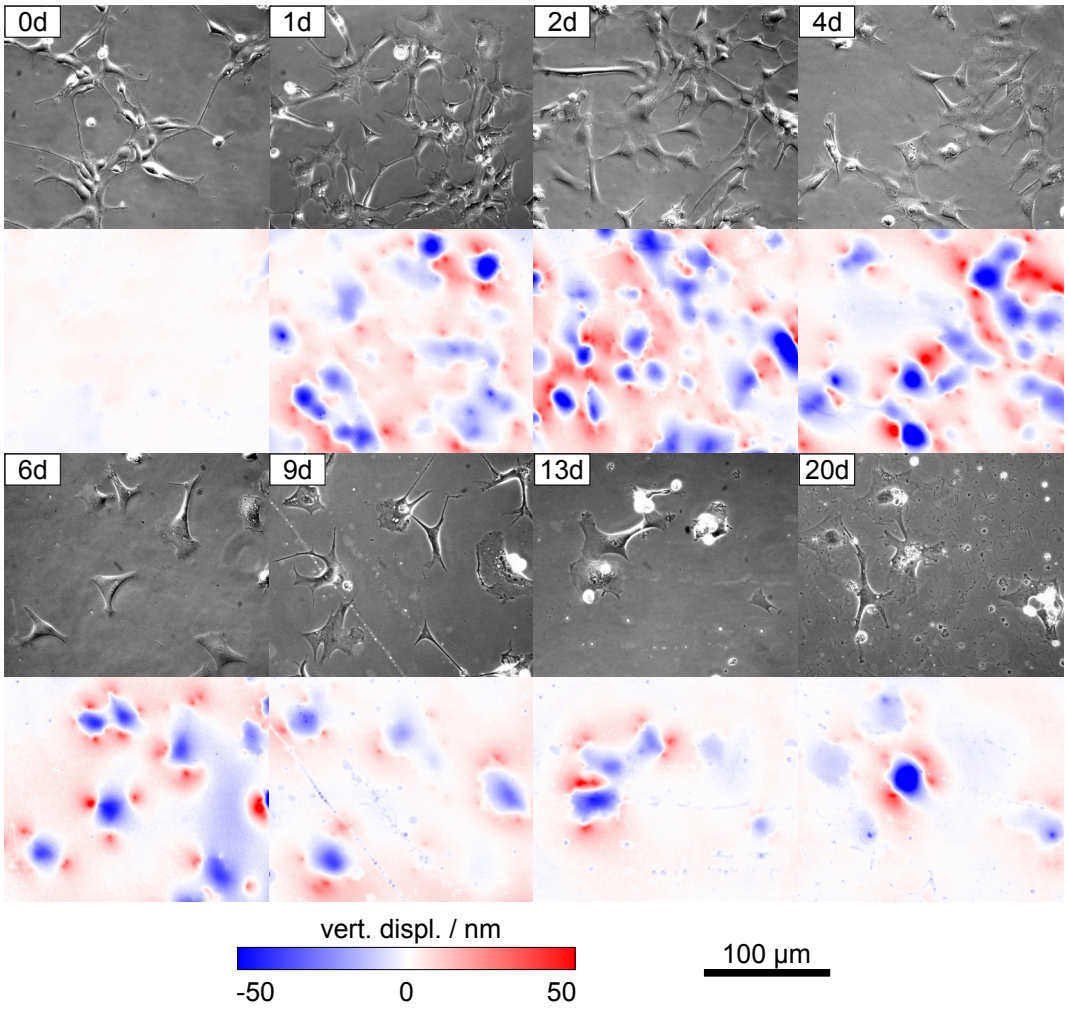

Figure 4.26: Representative phase-contrast and vertical displacement images for each day after differentiation. The measurement at 0 d was taken before changing to differentiation medium. Last measurement (20 d) represents a mix of stem cells seeded on the micro-cavity initially (0 d), and of cells differentiated in parallel in a plastic cell culture dish and seeded on the micro-cavity at day 19.

In the following analysis we only investigated the pushing of the cells. The total force, the sum of the forces acting upwards and downwards, has to be zero as otherwise the cells would experience an acceleration in either direction. This simplifies the data analysis for high cell densities because most of the indented volume as well as the maximum indentation is located under the cell. Hence, for the further analysis we applied a threshold to the data so that all pixels with a value larger than zero are set to zero (cf. Fig. 4.27c).

We then used the cell outlines for each cell to measure cell area, the mean indentation across each cell, and the maximum indentation (smallest value) for each cell. The total displaced volume under each cell was calculated by multiplying the cell area with the mean value.

We analysed all fields of view in this manner to obtain these values for each cell and then summarised the data for all cells at each time point in box plots (cf. Fig. 4.28). Figure 4.27d shows for one example how the distribution of the maximum indentations for, in this case, all 256 cells compares to the box plot. The box plot shows the median value labelled (50% in Fig. 4.27d) and indicates the spread of the data with the whiskers for the 5% and 95% percentile. In addition, to make the comparison between different time points but also between the different variables easier, we show the median value for each complete data set in Fig. 4.29. Note, we plot the volume in negative numbers to allow comparison with the mean value and the maximum indentation.

Furthermore, we performed statistical tests for maximum indentation and total indented volume to probe our data for statistically significant differences. All data sets have a non-normal distribution similar to what we show in Fig. 4.27d. Most data points are close to the median value but there is a long tail towards deeper indentation. Therefore, we applied a two sample U test (Mann-Whitney) between each time point. In Fig. 4.28c and (d) we only show the relation between the measurements for the undifferentiated cells at day 0 and all other time points, and between each adjacent data set. This captures the difference between all differentiation stages and the undifferentiated state as well as the statistically significant changes over time.

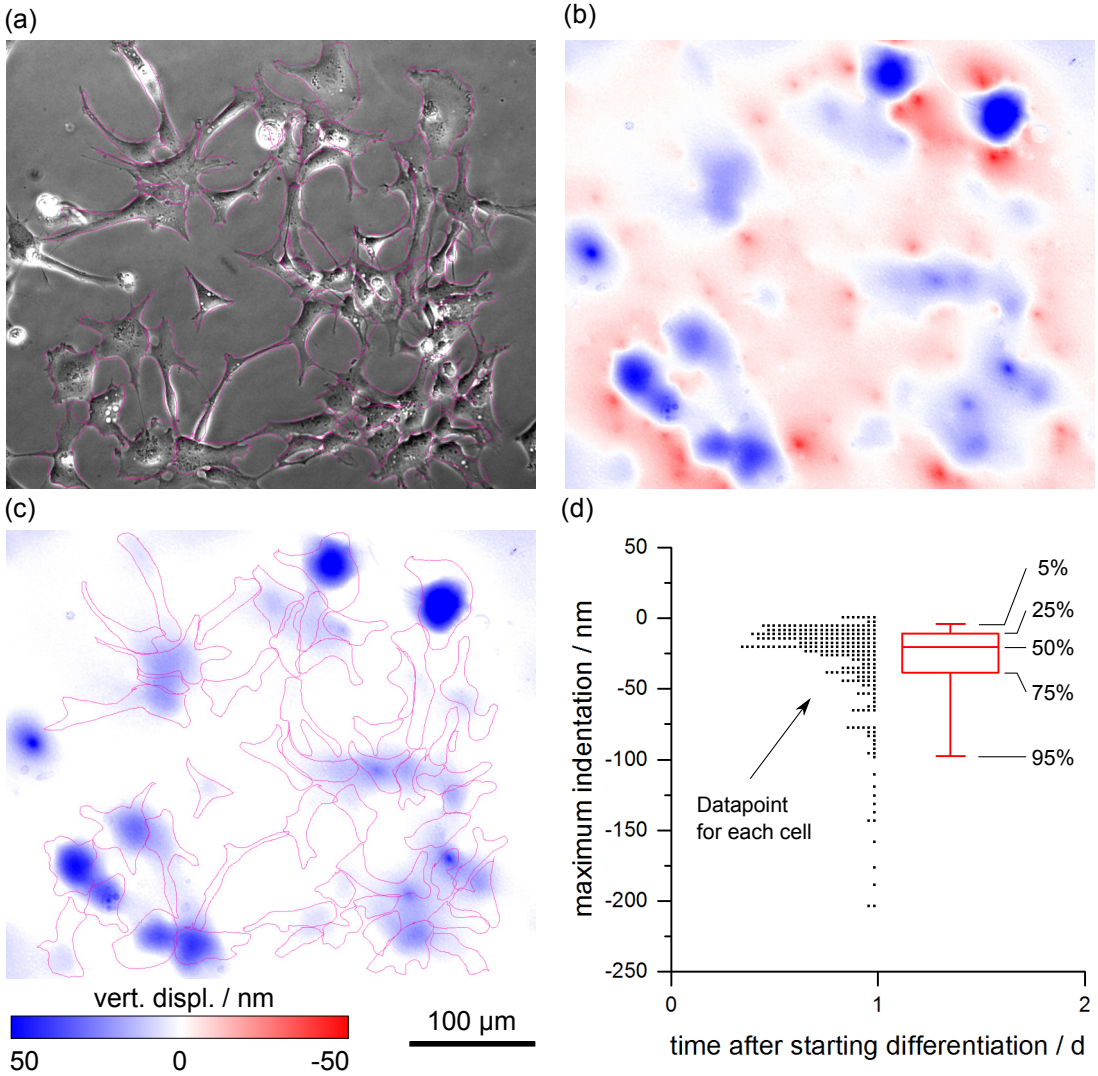

Figure 4.27: Overview of how the data in Fig. 4.26 was analysed. (a) Phase-contrast image with hand drawn cell outlines. (b) Vertical displacement map. (c) Displacement map after threshold was applied. Only values below zero are kept. (d) Summarised results after the analysis steps (a), (b), (c) were done for multiple field of views. Distribution of maximum indentation below each cell for all cells measured at one day after changing the differentiation medium. For this case 256 cells were measured. The distribution is summarised in a box plot. In addition to maximum indentation, we also measured and analysed mean indentation, cell area and indented volume.

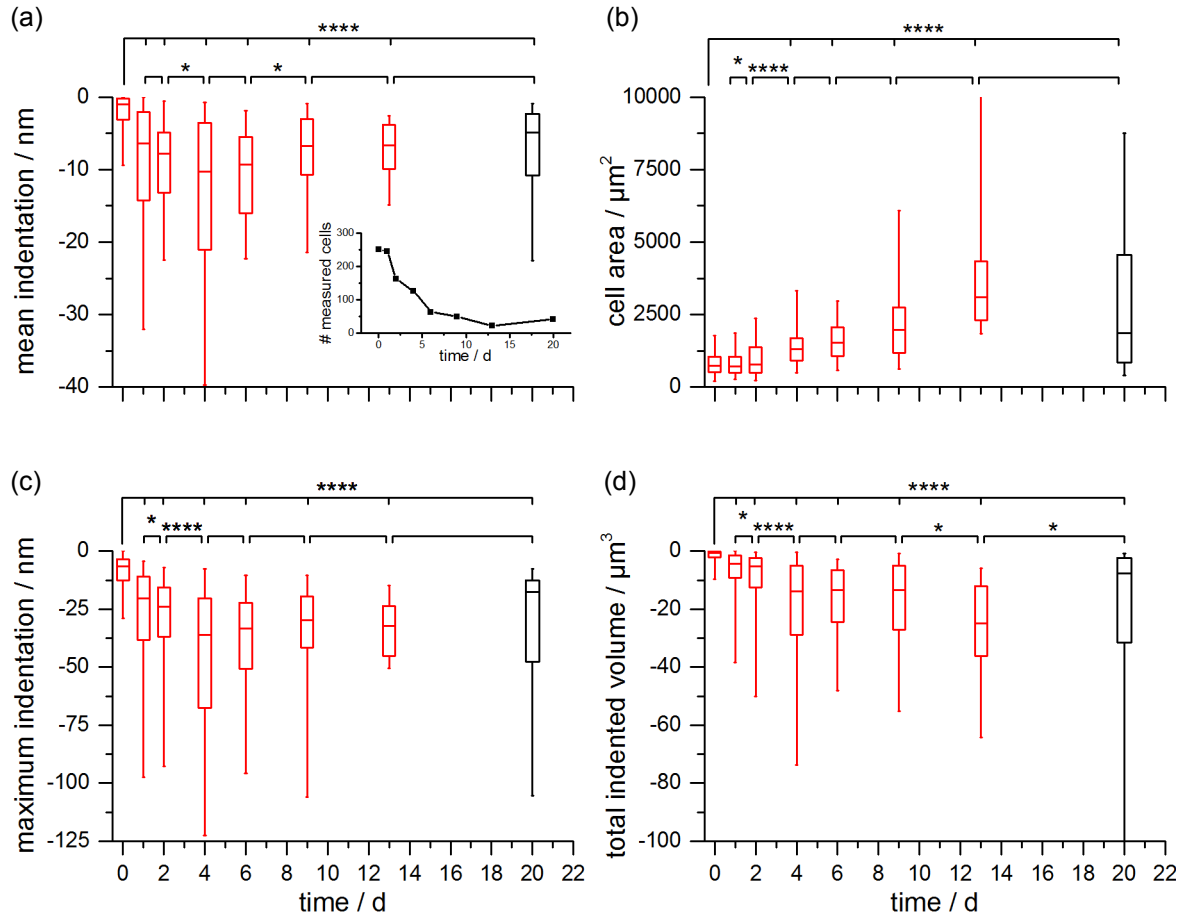

Figure 4.28: Box plots summarising all data collected for the differentiation of hNSC into astrocytes. Data representation according to Fig. 4.27d. Last measurement (black) represents a mix of initially seeded stem cells, and in hNSC differentiated in parallel in a plastic cell culture dish. (a) Mean value for indentation in the area under each cell as indicated in Fig. 4.27c. Inset: total number of cells which were investigated at each time point. (b) Cell area obtained by procedure pictured in Fig. 4.27a. (c) Maximum indentation below each cell. (d) Total indented volume below each cell, i.e. product of cell area and mean value. $^{*}p < 0.05$, $^{****}p < 0.0001$ by two sample U test (Mann-Whitney). Upper bracket refers to tests between 0 d and all other (individual) time points, lower brackets refer to tests between adjacent data sets. Brackets with no * indicate pairs with $p > 0.05$.

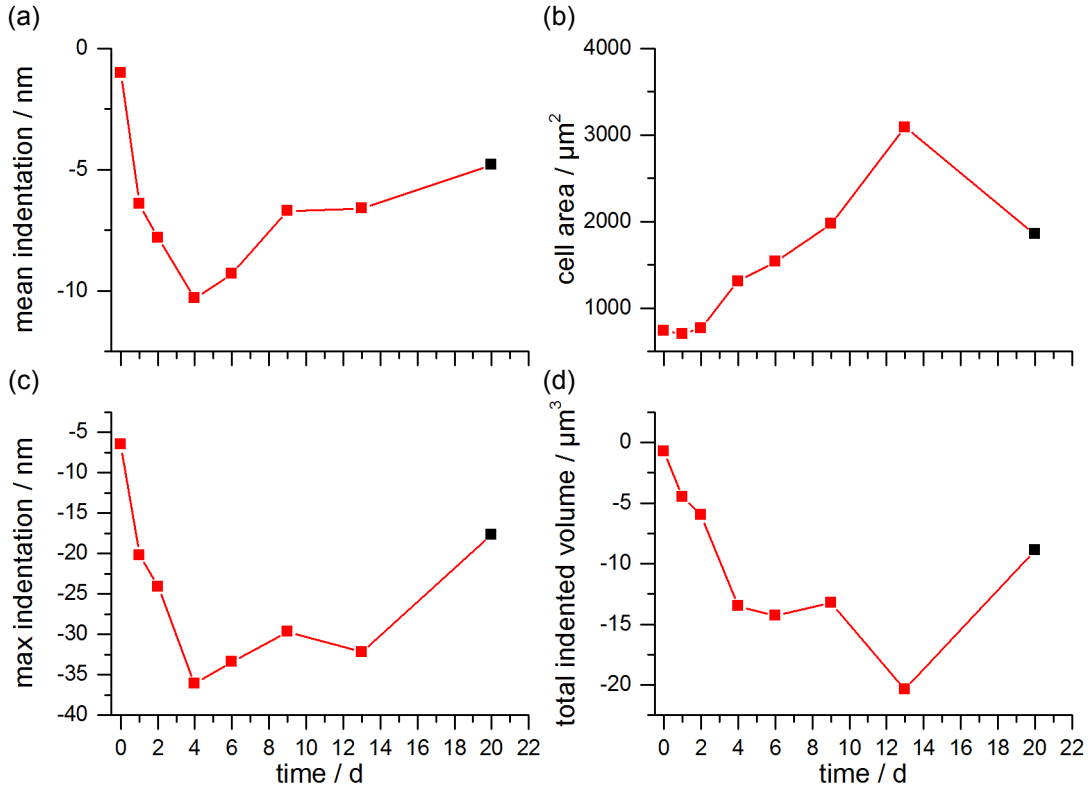

Figure 4.29: Summary of the median values from Fig. 4.28. Lines are drawn as guide for the eye.

4.5.5 Results

From the phase-contrast images in Fig. 4.26 we can see that as expected the cells change their morphology during the differentiation process[198]. Although the cells look more flat after switching the medium, the cell area only increases after day 4 (cf. Fig. 4.26 and Fig. 4.29b). Furthermore, starting at day 9 we can observe different phenotypes differing in cell area and in how elaborate the cell processes are. We can also see that the cell density decreases. We also observe that a significant number of cells die in the (undifferentiated) stem cell culture. However, as long as the stem cells have not started to differentiate, dying cells are replaced by the proliferation.

Apparently, switching to the differentiation medium has an almost immediate impact on the cell forces. The median of the maximum indentation is approximately −7 nm before the medium is changed and is already threefold higher after one day in the differentiation medium. The value increases up to −36 nm after 4 days in differentiation medium. After 4 days the cells seem not to change by how much they deform the micro-cavity any more. We can support this observation with our results from the statistical analysis. We find that at all time points the cells exert significantly higher forces compared to the cells in knock-out medium ($p < 0.0001$, cf. Fig. 4.28). During the first four days the change in maximum indentation is significant, by contrast, the Mann-Whitney U test does not indicate significant changes between subsequent time points after 4 days.

Next, we test if the maximum displaced volume, which is a measure for the overall strength of the cells, shows a similar behaviour. The two curves in Fig. 4.29c and (d) follow almost the same shape and in fact, the total displaced volume is even more stable between 4 and 9 days than compared to the maximum indentation. This is an effect of the increase in surface area covered by the cells. Moreover, our statistical tests indicate that there might be a difference between the cells at 9 and 13 days and between the cells at 13 and 20 days. This could either be attributed to further maturation of the astrocytes and/or to the contamination of the cells and then the change of the cell population by adding cells from the Petri dish.

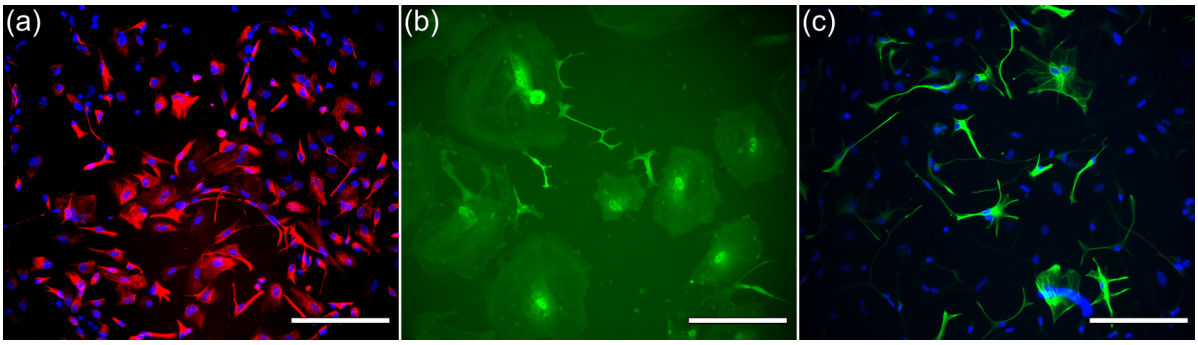

Figure 4.30: Staining for different stages of the stem cell differentiation into astrocytes. (a) Staining for nestin (red) in hNSC in knock-out medium, passage number 6. Counter-stain with Hoechst 33342 (Sigma Aldrich) (blue) (b) Staining for GFAP after 14 days in differentiation medium. (c) Staining for GFAP (green) and counter-stain with Hoechst 33342 (magenta) 23 days after adding differentiation medium. Scale bar 200 µm

For every cell population we observe cells which deform the micro-cavity up to fourfold more than the median of the population. We cannot say if these cells are potentially already differentiated astrocytes or if these cells show a different behaviour for other reasons. Possibly, all cells exert forces that are this strong at certain times (cf. results for the RPE1 cells in Fig. 4.6) and we simply captured some of the cells whilst at a time point where they exerted particularly strong forces.

After 23 days we stained the cells from the Petri dish for GFAP and obtained the Fig. 4.30c. Apparently not all cells stain positive for GFAP as one can see from the counter-stain of the nucleus. However, this could simply be attributed to the fact that the cells are not yet mature enough to produce GFAP. In fact, in an earlier experiment we differentiated hNSC into astrocytes and stained after 14 days. For these cells we did not observe any specific staining (cf. Fig. 4.30b). The fact that a significant amount of cells only starts to express GFAP after three weeks is known and this was also confirmed by the supplier (Thermofisher).

4.5.6 Discussion

This experiment shows that it is possible to cultivate cells on ERISM micro-cavities over weeks and that we can take measurements at individual time points during the course of

this experiment. To the best of our knowledge, these are the first results describing the force evolution during the differentiation of neural stem cells into astrocytes.

We find that already one day after switching to differentiation medium the cells significantly increase the forces they apply on the substrate. We acknowledge that the serum (FBS) in the differentiation medium is likely to be the reason for this behaviour. It has repeatedly been reported that FBS can boost actin-myosin contraction and/or FA assembly[199–204]. However, at this stage it is not clear whether this increase in force is only an artefact of adding FBS to the medium not influencing stem cell fate at all or if it is in-fact a requirement to allow differentiation. Lu et al. reported that the transcription factor SRF (serum response factor) plays a crucial role for astrocyte differentiation[205]. Connelly et al. found that SRF is involved in translating cell shape (spread versus rounded) into a lineage commitment in epidermal stem cells[206]. The authors attributed this effect to the change of G-actin concentration in the cells because G-actin[22] binds to the SER co-factor MAL, preventing in this case differentiation. Although Lu et al. did not make a link between their own results and the observations of Connelly et al. , this might explain why they found SRF to be important for astrogenesis. This would also align well with our own results which show an increase in the number of stress fibres (assuming that this is the origin of the increased stress) and therefore possibly a lower concentration of G-actin. Furthermore, Connelly et al. also found that SRF transcriptional activity is enhanced if FBS is added to the medium. It is possibly that hNSC start to probe their mechanical environment more actively once the biochemical environment allows differentiation. This aligns well with the reports that matrix rigidity influences stem cell fate, as the cells need to have a mechanism to determine the stiffness of the ECM. As we discussed in the beginning of this section, a link between applied stress and differentiation could be provided by stretch activated ion channels and integrin signalling.

We appreciate that from our results alone we can not draw definite conclusions of how exactly the change of stress fits into the picture of astrogenesis of hNSC. However, our results successfully show that ERISM can be an additional tool to investigate this process. We suggest to perform a variety of additional experiments. First, the experiment should be

[22] A reminder of what we explained in Section 2.1.2: G-actin or globular actin is a free actin monomers, compared to the F-actin in actin fibres.

repeated in serum-free medium to investigate how the applied forces change during the differentiation without an addition of serum. Second, it would be interesting to see the difference of forces during neurogenesis and astrogenesis. We assume that the differentiation into neurons would give very different results. As we showed in the previous section, primary neurons exert much weaker forces than astrocytes. We observe similar forces for the primary astrocytes from mice and the hNSC that were differentiated into astrocytes. Therefore, it is likely that also neurons which originate from hNSC are weaker than the astrocytes; in fact, their strength might be comparable to the undifferentiated stem cells. However, it would be interesting to test whether an increase of forces is observed in the beginning of the differentiation process followed by a decline.

Furthermore, ERISM measurements should be performed in combination with approaches which are known to alter stem cell fate. For instance, it would be interesting to investigate whether the inhibition of the stretch activated ion channel Piezo1 only prevents the cells from 'knowing' how much stress they exert, or if it actually leads to a change of the exerted stress itself. Also, it is not clear if one (only the serum) or multiple components, which were added/removed during the change from knock-out to differentiation medium, are responsible for the change in forces. This could be explored by systematically adding and removing the different components of the two media mixtures.

We could not stain the cells which we had on the ERISM micro-cavity because of contamination issues. However, correlating the forces the cells exert on the substrate with the actual percentage of astrocytes in the culture would be important. As a further step, one may want to use cell tagging. Our lab recently developed a technique to tag cells with lasing micro-beads[207]. A combination of this new cell tagging technique with ERISM would allow to track the differentiation process of individual cells and to very accurately link force generation with stem cell fate.

Chapter 5

Concluding Remarks and Outlook

5.1 Summary of the Results

Cell forces have gained increasing interest as important factors involved in cell division, cell migration, morphogenesis, wound healing, gene expression, growth cone guidance, stem cell differentiation, and cancer cell invasion. Existing force sensing techniques have been crucial to identify the importance of force generation and substrate stiffness sensing for the cellular processes mentioned above. However, existing techniques are often limited in their capability to accurately detect vertical forces and to measure a large number of cells over an extended periods of time.

In this thesis we introduced Elastic-Resonator-Interference-Stress-Microscopy (ERISM) as a novel tool to measure cellular forces. ERISM is based on measuring small thickness changes of an elastic optical micro-cavity to which cells apply forces. This is done using a modified inverted fluorescent microscope in wide-field configuration by scanning the illumination over a range of wavelengths to collect the spatially resolved spectral reflectance. By comparing the reflectivity with optical simulations, we calculate the local vertical displacement for each image pixel. In a final step we feed the vertical displacement map into a Finite Element Method (FEM) solver to calculate the stress cells apply to the micro-cavity.

The fully automated setup (and software *ERISM-Read*) allows hours-long measurements in time steps down to 2 s. Furthermore, the motorise translation stage in combination

with an auto-focus function facilitates measurements at multiple sample positions, and thus drastically increases the amount of data which can be collected for each sample. The calculation of the local cavity thickness (*ERISM-Calc*) from the experimental data is accurate enough to resolve the roughness of the micro-cavities which is about 2–3 nm. This resolution can be improved to 0.5 nm if an image of the roughness (without forces applied by cells) is recorded.

We demonstrated that ERISM can be used to measure cell forces of a variety of different cell types. In this thesis we focused on cells of the nervous system.

We first investigated the influence of the protein KIAA0319 on the migration pattern of RPE1 cells. Our measurements on wild-type and knock-out cells revealed that the absence of KIAA0319 at the cell membrane leads to a highly significant reduction in cell speed but increases force generation. Moreover, by analysing about 2000 data points for each cell population we found strong indications that wild-type cells have a control mechanism in-place which regulates cell forces towards smaller values. This is implied by a skewed force distribution curve compared to the distribution of the knock-out cells which has a Gaussian shape with a median at approximately 1.5 times higher force than the median of the wild-type cells.

In our second experiment we compared the forces of primary astrocytes and microglia. We found that astrocytes apply surprisingly high forces on our micro-cavities. We attribute this to the higher substrate stiffness of 4 kPa which we used in our experiment compared to the one order of magnitude smaller stiffness present in the brain. Moshayedi et al. showed that primary astrocytes seeded on substrates with a Young's modulus of 0.1 kPa will assume a star shape morphology whereas astrocytes seeded on substrates with 10 kPa exhibit a larger cell area comparable to what we observed in our experiments and what is observed by many groups for astrocytes in standard cell culture dishes[123]. Together with our results, this shows that astrocyte behaviour can change dramatically at regions of higher stiffness, e.g. glial scars and artificial structures like brain implants.

Furthermore, we showed that we can measure dynamic processes like cell attachment with ERISM. We found a similar shape of the force-time curve as has been observed by other

groups for fibroblasts; however, astrocytes attach significantly more slowly and the evolution of cell force and cell area over time is different than for fibroblasts. In particular, there is a different delay between the increase in force and cell area during the attachment process.

Experiments with primary microglia showed that we can easily measure the forces microglia apply to ERISM micro-cavities in their activated state and their amoeboid state. Our side-by-side comparison of astrocytes and microglia revealed a pronounced difference of the strength between these two cell types. Microglia were approximately 16 times weaker than astrocytes.

We then moved to even weaker cells and investigated the forces during neurite outgrowth and growth cone movement of neurons from dorsal root ganglia. In this experiment we showed that ERISM can track displacements down to 0.5 nm. Our results indicate that the forces of growth cones increases right before the neurite branches into multiple neurites. Moreover, we tracked a single stronger growth cone with high time resolution over more than 4 h and found a negative correlation between growth cone speed and traction force.

In the final experiment of this thesis we demonstrated that ERISM can be used to investigate stem cell differentiation, a process which takes several weeks. We measured how the forces human neural stem cells apply to an ERISM micro-cavity change during differentiation into astrocytes. We found that already 1 d after switching to differentiation medium the cells apply four times higher forces compared to the undifferentiated state. We attribute this behaviour to an increased actin-myosin activity caused by the serum in the differentiation medium. However, an increase of the generated mechanical stress might be a crucial part of the differentiation process itself.

5.2 Advantages and Limitations of ERISM Compared to Existing Force Microscopy Techniques

Two main benefits of ERISM compared to other forces sensing techniques are that ERISM measurements do not require recording a zero-force reference image and that we do not observe any photo-toxic effects. Because of these two features it is possible to measure cells

repeatedly or continuously over long periods of time. Our experiments with RPE1 cells show that this enables the collection of large datasets which reveal new insights into different cell populations. With the experiment on stem cells we proved that we can indeed track the forces involved in the weeks-long process of stem cell differentiation (by taking ERISM measurements at different days over weeks). Because ERISM does not require detaching cells after the force measurement, it is possible to fix cells on the micro-cavities after a measurement to apply staining for specific proteins. This is usually not possible with other force sensing techniques and represents a huge advantage as it allows one to correlate cell forces with the biochemistry inside cells. Polackwich et al. observed that neuronal growth cones retracted when illuminated almost continuously over 40 min during the acquisition of the fluorescence images required for a TFM measurement[68]. The light-source used for ERISM is a relatively low-intensity halogen lamp coupled to a monochromator, and thus the cells are exposed to very low light intensities (~50 $\mu W mm^{-2}$ at 650 nm). In none of our experiments we observe any photo-toxic effects on the cells despite of measurement times well beyond 10 hours and time intervals below one minute.

Moreover, because of the interference based detection principle of ERISM the resolution of the cavity thickness measurement does not change when objectives with lower magnifications are used. TFM and the micro-pillar-array force sensing technique are based on tracking displacements of beads or micro-pillars, and the accuracy of tracking these structures directly scales with the magnification of the objective. Hence these measurements are usually performed at high magnification with oil immersion objectives (NA>1). The ability of ERISM to use low magnification objectives in combination with a motorised setup enables us to cover large areas and thus to measure a large number of cells from the very same or from different cell populations in parallel over a long period of time.

ERISM is very well suited to detect vertical forces, a feature which is lacking in most other force sensing techniques. Interestingly, in order to observe podosome protrusions of macrophages, stamp like structures which vertically probe the ECM underneath the cell, Labernadie et al. invented a novel technique based on seeding cells on an ultra-thin membrane which is then placed upside down to detect the nanometre displacements of

these protrusions with AFM. Although AFM is well suited to detect nanometre displacements, it is a scanning probe technique and therefore slow if larger areas (e.g. multiple cells) are of interest. Although not part of this thesis[1], we demonstrated that we can easily measure the protrusions of podosomes over an extended period of time with ERISM[77].

Although ERISM is inherently well suited to detect vertical forces, we also showed that we can detect purely horizontal forces as for instance exerted by growth cones. The fact that a horizontal force leads to a vertical displacement suggests that in most cases ERISM detects a combination of horizontal and vertical forces. At present we do not know how this entanglement influences the correctness of our stress calculation with FEM. However, we believe that even if only displacements are measured, i.e. no stress or forces calculated, the determined maximum displacement or total indented volume are good measures to compare cell-to-cell variations and especially to compare different cell populations. Moreover, changes of vertical displacements over time can for instance be used to correlate relative exerted stress and cell speed as we did for a growth cone in Section 4.4.3.

Overall, ERISM proves to be an extremely versatile tool to obtain leading edge results for a variety of cell types and cellular structures. It should be noted that the entire development of ERISM and first measurements for a variety of cells were carried out in a single research group, with the main work done by Dr. Nils M. Kronenberg and Philipp Liehm under the supervision of Prof. Malte C. Gather. Within the course of this PhD these efforts have led to very competitive and exciting results. Once other groups adapt ERISM and contribute to its further improvement it is likely that more substantial progress will be made on a short time-scale. So in a way the moderate amount of development time that was required to develop ERISM (relative to other force sensing methods) to its present stage highlights the longer term potential of ERISM.

[1] Experiments performed by Dr. Nils M. Kronenberg.

5.3 Ideas for Further Improvements of ERISM

Whilst ERISM is at a state where we can routinely perform cell force measurements further improvements are already planned.

Although we showed that we can use antibody staining to label cells on ERISM micro-cavities, we think it is also possible to take fluorescence time-lapse data during the course of a long-term ERISM experiment, e.g. to image part of the cytoskeleton. At present, placing filter cubes for fluorescence imaging in the beam path and removing the filter cubes has to be done by hand. This can be motorised which would allow to perform ERISM measurements in combination with fluorescence imaging over several hours.

When we measured astrocytes on an ERISM micro-cavity we observed very high deformations and we had to estimate the cavity thickness by counting interference fringes. We observed even stronger deformations when we placed a larvae of a fruit-fly (drosophila) on an ERISM micro-cavity. Dr. Jan Murawski has started to develop an algorithm which calculates the cavity thickness based on counting fringes as we discusses in Section 4.3.4. Initial results suggest that this will enable us to measure the forces of these larvae at a time resolution well below 1 s as only two or three images at different wavelengths are required for each time frame.

We successfully showed that we can measure lateral forces with ERISM. We also provided an estimate of how vertical displacements measured with ERISM relate to horizontal forces by lateral AFM. Although very challenging, we think that the lateral force calibration can be improved by either functionalisation of the AFM tip and micro-cavity surface and performing the calibration in a high salt concentration to remove any electro static effects, or by performing the measurement in air and applying an electric potential between tip and micro-cavity surface to compensate for the electro static effect. In addition, it might be possible to introduce either fluorescent particles in the micro-cavity or to apply a regular pattern on the top surface of the micro-cavity. This would allow one to perform TFM like measurements to track lateral displacements whilst keeping the benefits of the very high vertical resolution of ERISM.

In this thesis we varied the stiffness of the micro-cavity by increasing the plasma treatment time before evaporating the top gold layer on the micro-cavity. Although this leads to the desired effect of an increased apparent stiffness of the micro-cavity, it may also lead to a big difference of the stiffness in lateral and vertical direction. It is possible to directly vary the stiffness of the elastomer by changing the mixing ratio of the two elastomer components, and thus increasing the stiffness range we can use for ERISM measurements. While we chose a very soft elastomer for the results presented here, applications where higher forces are to be investigated could use, stiffer elastomers.

5.4 Future Applications of ERISM

The focus of this thesis was the development of ERISM and to show that it can be applied to measure forces which different cells apply to the substrate.

In ERISM measurements cellular forces are visible in the live reflectance image recorded for a single wavelength. This suggests that ERISM can be used as a screening technique (e.g. for cancer cells) if a significant difference in cell forces or force pattern exists between the cells of interest. In addition, we showed that ERISM can investigate the influence of a gene/protein knock-out on the forces involved in cell migration for a large number of cells. Investigations of highly complex systems such as gene expression pathways which lead to certain cell forces or migration patterns might benefit from ERISM measurements which can provide a high number of measurement points to reveal whether a gene knock-out leads to a specific phenotype.

We are currently working in our lab on a combination of ERISM and Brillouin-Spectroscopy, a method based on detecting photon-phonon scattering to measure spatially resolved the stiffness of different structures, e.g. cells. The combination of the two techniques is likely to lead to very interesting results as it will be possible to relate the changes of cellular forces to local stiffness changes. For example, AFM measurements have shown that the different domains[2] of neural growth cones have different stiffness[208], however,

[2]The growth cone domains are: P domain, covers filopodia and lamellipodium; C domain, microtubule rich region at transition to axon; T domain, between P and C domain, consists of actin arcs close to the P domain.

probing the stiffness with AFM influences growth cone behaviour because of the applied force. The combination of Brillouin-Spectroscopy as a non-contact method and ERISM is a promising approach to investigate the link between stiffness changes and force generation during growth cone migration.

References

[1] Eugene Hecht. *Optics*. Addison-Wesley, 4th edition, 2002.

[2] Bray Alberts, Johnson Hopkin, Raff Lewis, and Walter Roberts. *Essential Cell Biology*. Garland Science, 4th edition, 2014.

[3] Stefan W. Hell and Jan Wichmann. Breaking the diffraction resolution limit by stimulated emission: stimulated-emission-depletion fluorescence microscopy. *Optics Letters*, 19(11):780, jun 1994.

[4] Thomas A. Klar and Stefan W. Hell. Subdiffraction resolution in far-field fluorescence microscopy. *Optics Letters*, 24(14):954, jul 1999.

[5] Michael J Rust, Mark Bates, and Xiaowei W Zhuang. Sub-diffraction-limit imaging by stochastic optical reconstruction microscopy (STORM). *Nature Methods*, 3(10):793–795, 2006.

[6] G Bao and S Suresh. Cell and molecular mechanics of biological materials. *Nature Materials*, 2(11):715–25, nov 2003.

[7] William J Polacheck and Christopher S Chen. Measuring cell-generated forces: a guide to the available tools. *Nature Methods*, 13(5):415–423, 2016.

[8] James H-C Wang and Jeen-Shang Lin. Cell traction force and measurement methods. *Biomechanics and Modeling in Mechanobiology*, 6(6):361–71, nov 2007.

[9] Adam J Engler, Shamik Sen, H Lee Sweeney, and Dennis E Discher. Matrix elasticity directs stem cell lineage specification. *Cell*, 126(4):677–89, aug 2006.

[10] Sharona Even-Ram, Vira Artym, and Kenneth M Yamada. Matrix control of stem cell fate. *Cell*, 126(4):645–7, aug 2006.

[11] Penelope C Georges and Paul A Janmey. Cell type-specific response to growth on soft materials. *Journal of applied physiology (Bethesda, Md. : 1985)*, 98(4):1547–53, apr 2005.

[12] Penelope C Georges, William J Miller, David F Meaney, Evelyn S Sawyer, and Paul a Janmey. Matrices with compliance comparable to that of brain tissue select neuronal over glial growth in mixed cortical cultures. *Biophysical Journal*, 90(8):3012–3018, 2006.

[13] Darren S Gray, Joe Tien, and Christopher S Chen. Repositioning of cells by mechanotaxis on surfaces with micropatterned Young's modulus. *Journal of biomedical materials research. Part A*, 66(3):605–614, 2003.

[14] Robert J. Pelham and Yu L. Wang. Cell locomotion and focal adhesions are regulated by the mechanical properties of the substrate. *Biological Bulletin*, 194(3):348–350, 1998.

[15] Shelly R. Peyton and Andrew J. Putnam. Extracellular matrix rigidity governs smooth muscle cell motility in a biphasic fashion. *Journal of Cellular Physiology*, 204(1):198–209, 2005.

[16] T. Betz, D. Koch, Y.-B. Lu, K. Franze, and J. A. Kas. Growth cones as soft and weak force generators. *Proceedings of the National Academy of Sciences*, 108(33):13420–13425, 2011.

[17] Tony Yeung, Penelope C. Georges, Lisa A. Flanagan, Beatrice Marg, Miguelina Ortiz, Makoto Funaki, Nastaran Zahir, Wenyu Ming, Valerie Weaver, and Paul A. Janmey. Effects of substrate stiffness on cell morphology, cytoskeletal structure, and adhesion. *Cell Motility and the Cytoskeleton*, 60(1):24–34, 2005.

[18] Farhan Chowdhury, Sungsoo Na, Dong Li, Yeh-Chuin Poh, Tetsuya S Tanaka, Fei Wang, and Ning Wang. Material properties of the cell dictate stress-induced spreading and differentiation in embryonic stem cells. *Nature Materials*, 9(1):82–88, 2010.

[19] Brendon G. Ricart, Michael T. Yang, Christopher a. Hunter, Christopher S. Chen, and Daniel a. Hammer. Measuring traction forces of motile dendritic cells on micropost arrays. *Biophysical Journal*, 101(11):2620–2628, 2011.

[20] James J Tomasek, Giulio Gabbiani, Boris Hinz, Christine Chaponnier, and Robert a Brown. Myofibroblasts and mechano-regulation of connective tissue remodelling. *Nature Reviews. Molecular cell biology*, 3(5):349–63, 2002.

[21] Aaron F. Mertz, Shiladitya Banerjee, Yonglu Che, Guy K. German, Ye Xu, Callen Hyland, M. Cristina Marchetti, Valerie Horsley, and Eric R. Dufresne. Scaling of Traction Forces with the Size of Cohesive Cell Colonies Aaron. *Physical Review Letters*, 108(19):198101, 2012.

[22] Christopher A. Lemmon, Christopher S. Chen, and Lewis H. Romer. Cell traction forces direct fibronectin matrix assembly. *Biophysical Journal*, 96(2):729–738, 2009.

[23] Agustí Brugués, Ester Anon, Vito Conte, Jim H. Veldhuis, Mukund Gupta, Julien Colombelli, José J. Muñoz, G. Wayne Brodland, Benoit Ladoux, and Xavier Trepat. Forces driving epithelial wound healing. *Nature Physics*, 10(9):683–690, aug 2014.

[24] Dhananjay T Tambe, C Corey Hardin, Thomas E Angelini, Kavitha Rajendran, Chan Young Park, Xavier Serra-Picamal, Enhua H Zhou, Muhammad H Zaman, James P Butler, David A Weitz, Jeffrey J Fredberg, and Xavier Trepat. Collective cell guidance by cooperative intercellular forces. *Nature Materials*, 10(6):469–75, 2011.

[25] Daniel A Fletcher and R Dyche Mullins. Cell mechanics and the cytoskeleton. *Nature*, 463(7280):485–92, jan 2010.

[26] J Thomas Parsons, Alan Rick Horwitz, and Martin a Schwartz. Cell adhesion: integrating cytoskeletal dynamics and cellular tension. *Nature Reviews. Molecular cell biology*, 11(9):633–43, sep 2010.

[27] Miguel Vicente-Manzanares, Donna J Webb, and a Rick Horwitz. Cell migration at a glance. *Journal of cell science*, 118:4917–4919, 2005.

[28] Germán Reig, Eduardo Pulgar, and Miguel L Concha. Cell migration: from tissue culture to embryos. *Development (Cambridge, England)*, 141(10):1999–2013, 2014.

[29] Erik W Dent, Stephanie L Gupton, and Frank B Gertler. The growth cone cytoskeleton in Axon outgrowth and guidance. *Cold Spring Harbor Perspectives in Biology*, 3(3):1–39, 2011.

[30] B M Gumbiner. Cell adhesion: the molecular basis of tissue architecture and morphogenesis. *Cell*, 84(3):345–57, feb 1996.

[31] Richard O. Hynes. Integrins: Bidirectional, allosteric signaling machines. *Cell*, 110(6):673–687, 2002.

[32] Miguel Vicente-Manzanares, Colin Kiwon Choi, and Alan Rick Horwitz. Integrins in cell migration–the actin connection. *Journal of Cell Science*, 122(2):199–206, 2009.

[33] Fiona M Watt and Wilhelm T S Huck. Role of the extracellular matrix in regulating stem cell fate. *Nature Reviews. Molecular cell biology*, 14(8):467–73, 2013.

[34] R Zaidel-Bar, M Cohen, L Addadi, and B Geiger. Hierarchical assembly of cell-matrix adhesion complexes. *Biochemical Society transactions*, 32:416–20, jun 2004.

[35] Sabina E Winograd-Katz, Reinhard Fässler, Benjamin Geiger, and Kyle R Legate. The integrin adhesome: from genes and proteins to human disease. *Nature Reviews: Molecular Cell Biology*, 15(4):273–288, 2014.

[36] K Burridge and M Chrzanowska-Wodnicka. Focal adhesions, contractility, and signaling. *Annual review of cell and developmental biology*, 12:463–518, jan 1996.

[37] Tim Lämmermann, Bernhard L. Bader, Susan J. Monkley, Tim Worbs, Roland Wedlich-Söldner, Karin Hirsch, Markus Keller, Reinhold Förster, David R. Critchley, Reinhard Fässler, and Michael Sixt. Rapid leukocyte migration by integrin-independent flowing and squeezing. *Nature*, 453(7191):51–5, 2008.

[38] Oliver T. Fackler and Robert Grosse. Cell motility through plasma membrane blebbing. *Journal of Cell Biology*, 181(6):879–884, 2008.

[39] Ewa K. Paluch and Erez Raz. The role and regulation of blebs in cell migration. *Current Opinion in Cell Biology*, 25(5):582–590, 2013.

[40] Revathi Ananthakrishnan and Allen Ehrlicher. The forces behind cell movement. *International journal of biological sciences*, 3(5):303–17, jan 2007.

[41] C. a. Parent. A Cell's Sense of Direction. *Science*, 284(5415):765–770, apr 1999.

[42] Miguel Vicente-Manzanares, Xuefei Ma, Robert S Adelstein, and Alan Rick Horwitz. Non-muscle myosin II takes centre stage in cell adhesion and migration. *Nature Reviews. Molecular cell biology*, 10(11):778–90, nov 2009.

[43] E Evans and A Yeung. Apparent viscosity and cortical tension of blood granulocytes determined by micropipet aspiration. *Biophysical Journal*, 56(1):151–60, 1989.

[44] K Svoboda and S M Block. Biological applications of optical forces. *Ann. Rev. Biophys. Biomol. Str.*, 23:247–285, 1994.

[45] M. Dao, C. T. Lim, and S. Suresh. Mechanics of the human red blood cell deformed by optical tweezers. *Journal of the Mechanics and Physics of Solids*, 51(11-12):2259–2280, 2003.

[46] J Chen, B Fabry, E L Schiffrin, and N Wang. Twisting integrin receptors increases endothelin-1 gene expression in endothelial cells. *American Journal of Physiology. Cell Physiology*, 280(6):C1475–C1484, 2001.

[47] Giuliano Scarcelli and Seok Hyun Yun. Confocal Brillouin microscopy for three-dimensional mechanical imaging. *Nature Photonics*, 2:39–43, dec 2007.

[48] Anshu B. Mathur, Amy M. Collinsworth, William M. Reichert, William E. Kraus, and George A. Truskey. Endothelial, cardiac muscle and skeletal muscle exhibit different viscous and elastic properties as determined by atomic force microscopy. *Journal of Biomechanics*, 34(12):1545–1553, 2001.

[49] A K Harris, P Wild, and D Stopak. Silicone rubber substrata: a new wrinkle in the study of cell locomotion. *Science (New York, N.Y.)*, 208(4440):177–179, 1980.

[50] M Dembo and Y L Wang. Stresses at the cell-to-substrate interface during locomotion of fibroblasts. *Biophysical Journal*, 76(4):2307–16, 1999.

[51] Robert W Style, Rostislav Boltyanskiy, Guy K German, Callen Hyland, Christopher W MacMinn, Aaron F Mertz, Larry A Wilen, Ye Xu, and Eric R Dufresne. Traction force microscopy in physics and biology. *Soft Matter*, 10(23):4047–55, 2014.

[52] Thomas Grevesse, Marie Versaevel, Géraldine Circelli, Sylvain Desprez, and Sylvain Gabriele. A simple route to functionalize polyacrylamide hydrogels for the independent tuning of mechanotransduction cues. *Lab on a chip*, 13(5):777–80, 2013.

[53] U S Schwarz, N Q Balaban, D Riveline, A Bershadsky, B Geiger, and S A Safran. Calculation of forces at focal adhesions from elastic substrate data: the effect of localized force and the need for regularization. *Biophysical Journal*, 83(3):1380–94, 2002.

[54] Benedikt Sabass, Margaret L Gardel, Clare M Waterman, and Ulrich S Schwarz. High resolution traction force microscopy based on experimental and computational advances. *Biophysical Journal*, 94(1):207–20, jan 2008.

[55] Ulrich S Schwarz and Jérôme R D Soiné. Traction force microscopy on soft elastic substrates: A guide to recent computational advances. *Biochimica et biophysica acta*, 1853(11):3095–3104, 2015.

[56] Matthew S. Hall, Rong Long, Xinzeng Feng, YuLing Huang, Chung Yuen Hui, and Mingming Wu. Toward single cell traction microscopy within 3D collagen matrices. *Experimental Cell Research*, 319(16):2396–2408, 2013.

[57] Sung Sik Hur, Yihua Zhao, Yi-Shuan Li, Elliot Botvinick, and Shu Chien. Live Cells Exert 3-Dimensional Traction Forces on Their Substrata. *Cellular and molecular bioengineering*, 2(3):425–436, sep 2009.

[58] Stacey a Maskarinec, Christian Franck, David a Tirrell, and Guruswami Ravichandran. Quantifying cellular traction forces in three dimensions. *Proceedings of the National Academy of Sciences*, 106(52):22108–22113, 2009.

[59] Christian Franck, Stacey a Maskarinec, David a Tirrell, and Guruswami Ravichandran. Three-dimensional traction force microscopy: A new tool for quantifying cell-matrix interactions. *PLoS ONE*, 6(3):e17833, jan 2011.

[60] Juan C. del Álamo, Ruedi Meili, Begoña Álvarez-González, Baldomero Alonso-Latorre, Effie Bastounis, Richard Firtel, and Juan C Lasheras. Three-Dimensional Quantification of Cellular Traction Forces and Mechanosensing of Thin Substrata by Fourier Traction Force Microscopy. *PLoS ONE*, 8(9):e69850, jan 2013.

[61] Francesco Pampaloni, Emmanuel G Reynaud, and Ernst H K Stelzer. The third dimension bridges the gap between cell culture and live tissue. *Nature Reviews. Molecular cell biology*, 8(10):839–845, 2007.

[62] Wesley R Legant, Jordan S Miller, Brandon L Blakely, Daniel M Cohen, Guy M Genin, and Christopher S Chen. Measurement of mechanical tractions exerted by cells in three-dimensional matrices. *Nature Methods*, 7(12):969–971, 2010.

[63] Huw Colin-York, Dilip Shrestha, James Felce, Dominic Waithe, Emad Moeendarbary, Simon Davis, Christian Eggeling, and Marco Fritzsche. Super-resolved traction force microscopy (STFM). *Nano Letters*, 2016.

[64] Sergey V Plotnikov, Ana M Pasapera, Benedikt Sabass, and Clare M Waterman. Force fluctuations within focal adhesions mediate ECM-rigidity sensing to guide directed cell migration. *Cell*, 151(7):1513–27, dec 2012.

[65] Xavier Trepat, Michael R. Wasserman, Thomas E. Angelini, Emil Millet, David A. Weitz, James P. Butler, and Jeffrey J. Fredberg. Physical forces during collective cell migration. *Nature Physics*, 5(6):426–430, 2009.

[66] Mei Rosa Ng, Achim Besser, Joan S Brugge, and Gaudenz Danuser. Mapping the dynamics of force transduction at cell–cell junctions of epithelial clusters. *eLife*, 3:1–29, 2014.

[67] Daniel Koch, William J Rosoff, Jiji Jiang, Herbert M Geller, and Jeffrey S Urbach. Strength in the periphery: Growth cone biomechanics and substrate rigidity response in peripheral and central nervous system neurons. *Biophysical Journal*, 102(3):452–460, feb 2012.

[68] Robert J. Polackwich, Daniel Koch, Ryan McAllister, Herbert M. Geller, and Jeffrey S. Urbach. Traction force and tension fluctuations in growing axons. *Frontiers in Cellular Neuroscience*, 9:1–9, 2015.

[69] Callen Hyland, Aaron F Mertz, Paul Forscher, and Eric Dufresne. Dynamic peripheral traction forces balance stable neurite tension in regenerating Aplysia bag cell neurons. *Scientific Reports*, 4:4961, jan 2014.

[70] John L Tan, Joe Tien, Dana M Pirone, Darren S Gray, Kiran Bhadriraju, and Christopher S Chen. Cells lying on a bed of microneedles: an approach to isolate mechanical force. *Proceedings of the National Academy of Sciences of the United States of America*, 100(4):1484–9, feb 2003.

[71] Olivia du Roure, Alexandre Saez, Axel Buguin, Robert H Austin, Philippe Chavrier, Pascal Silberzan, and Benoit Ladoux. Force mapping in epithelial cell migration. *Proceedings of the National Academy of Sciences of the United States of America*, 102(7):2390–2395, 2005.

[72] A Saez, E Anon, M Ghibaudo, O du Roure, J-M Di Meglio, P Hersen, P Silberzan, A Buguin, and B Ladoux. Traction forces exerted by epithelial cell sheets. *Journal of Physics: Condensed Matter*, 22(19):194119, may 2010.

[73] Saba Ghassemi, Giovanni Meacci, Shuaimin Liu, Alexander A Gondarenko, Anurag Mathur, Pere Roca-Cusachs, Michael P Sheetz, and James Hone. Cells test substrate rigidity by local contractions on submicrometer pillars. *Proceedings of the National Academy of Sciences of the United States of America*, 109(14):5328–33, 2012.

[74] Carsten Grashoff, Brenton D Hoffman, Michael D Brenner, Ruobo Zhou, Maddy Parsons, Michael T Yang, Mark a McLean, Stephen G Sligar, Christopher S Chen, Taekjip Ha, and Martin a Schwartz. Measuring mechanical tension across vinculin reveals regulation of focal adhesion dynamics. *Nature*, 466(7303):263–6, jul 2010.

[75] Brandon L Blakely, Christoph E Dumelin, Britta Trappmann, Lynn M McGregor, Colin K Choi, Peter C Anthony, Van K Duesterberg, Brendon M Baker, Steven M Block, David R Liu, and Christopher S Chen. A DNA-based molecular probe for optically reporting cellular traction forces. *Nature Methods*, 11(12), oct 2014.

[76] Xuefeng Wang and Taekjip Ha. Defining single molecular forces required to activate integrin and notch signaling. *Science (New York, N.Y.)*, 340(6135):991–4, 2013.

[77] Nils M. Kronenberg, Philipp Liehm, Anja Steude, Johanna A. Knipper, Jessica G. Borger, Giuliano Scarcelli, Kristian Franze, Simon J. Powis, and Malte C. Gather. Long-Term Imaging of Cellular Forces with High Precision by Elastic Resonator Interference Stress Microscopy. 2016.

[78] Alex J. Yuffa and John A. Scales. Object-oriented electrodynamic S-matrix code with modern applications. *Journal of Computational Physics*, 231(14):4823–4835, may 2012.

[79] PB Johnson and RW Christy. Optical constants of the noble metals. *Physical Review B*, 1318(1970), 1972.

[80] I. H. Malitson. Interspecimen Comparison of the Refractive Index of Fused Silica. *Journal of the Optical Society of America*, 55(10):1205, 1965.

[81] P. B. Johnson and R. W. Christy. Optical constants of transition metals: Ti, V, Cr, Mn, Fe, Co, Ni, and Pd. *Physical Review B*, 9(12):5056–5070, jun 1974.

[82] Cory Quammen. Nonuniform Background Removal. http://imagejdocu.tudor.lu/doku.php?id=plugin:filter:nonuniform{_}background{_}removal:start, 2007. Accessed: 2016-01-10.

[83] Eric Betzig, George H Patterson, Rachid Sougrat, O Wolf Lindwasser, Scott Olenych, Juan S Bonifacino, Michael W Davidson, J. Lippincott-Schwartz, and Harald F Hess. Imaging Intracellular Fluorescent Proteins at Nanometer Resolution. *Science*, 313(5793):1642–1645, sep 2006.

[84] Daisuke Takao, Atsushi Taniguchi, Takaaki Takeda, Seiji Sonobe, and Shigenori Nonaka. High-Speed Imaging of Amoeboid Movements Using Light-Sheet Microscopy. *PLoS ONE*, 7(12):1–6, 2012.

[85] Http://www.python.org/. Python, 2014.

[86] Http://cython.org/. Cython, 2014.

[87] Rong Long, Matthew S. Hall, Mingming Wu, and Chung Yuen Hui. Effects of gel thickness on microscopic indentation measurements of gel modulus. *Biophysical Journal*, 101(3):643–650, 2011.

[88] Emilios K Dimitriadis, Ferenc Horkay, Julia Maresca, Bechara Kachar, and Richard S Chadwick. Determination of elastic moduli of thin layers of soft material using the atomic force microscope. *Biophysical Journal*, 82(5):2798–810, may 2002.

[89] David V. Hutton. *Fundamentals of finite element analysis*. McGraw-Hill, 2004.

[90] Ron Milo. Bionumbers. http://www.bionumbers.hms.harvard.edu, 2010. Accessed: 2017-02-01.

[91] Marta Martin, Ouafa Benzina, Vivien Szabo, Attila-Gergely Végh, Olivier Lucas, Thierry Cloitre, Frédérique Scamps, and Csilla Gergely. Morphology and nanomechanics of sensory neurons growth cones following peripheral nerve injury. *PloS One*, 8(2), 2013.

[92] Emilie L Grzywa, Aih Cheun Lee, Gil U Lee, and Daniel M Suter. High-Resolution Analysis of Neuronal Growth Cone Morphology by Comparative Atomic Force and Optical Microscopy. *Journal of Neurobiology*, 66:1529–1543, 2006.

[93] Britta Koch, Anne K. Meyer, Linda Helbig, Stefan M. Harazim, Alexander Storch, Samuel Sanchez, and Oliver G. Schmidt. Dimensionality of Rolled-up Nanomembranes Controls Neural Stem Cell Migration Mechanism. *Nano Letters*, 15(8):5530–5538, 2015.

[94] Martin Munz. Force calibration in lateral force microscopy: a review of the experimental methods. *Journal of Physics D: Applied Physics*, 43(6):063001, 2010.

[95] Onejae Sul and Eui-Hyeok Yang. Step-edge calibration of torsional sensitivity for lateral force microscopy. *Measurement Science and Technology*, 20(11):115104, 2009.

[96] Matthew A. Hopcroft, William D. Nix, and Thomas W. Kenny. What is the Young's modulus of silicon? *Journal of Microelectromechanical Systems*, 19(2):229–238, 2010.

[97] Dale Purves, George J. Augustine, David Fitzpatrick, William C. Hall, Anthony-Samuel LaMantia, and Leonard E. White. *Neuroscience, 5th Edition*. Sinauer Associates, Sunderland, U.S.A., 5th edition, 2012.

[98] Ke Xu, Guisheng Zhong, and Xiaowei Zhuang. Actin, spectrin, and associated proteins form a periodic cytoskeletal structure in axons. *Science (New York, N.Y.)*, 339(6118):452–6, 2013.

[99] C. H. Lin, E. M. Espreafico, M. S. Mooseker, and P. Forscher. Myosin drives retrograde F-actin flow in neuronal growth cones. *Neuron*, 16(4):769–782, 1996.

[100] Jeffrey L Goldberg. How does an axon grow? *Genes & Development*, 17:941–958, 2003.

[101] Robert H Nichol, Kate M Hagen, Derek C Lumbard, Erik W Dent, and Timothy M Gómez. Guidance of Axons by Local Coupling of Retrograde Flow to Point Contact Adhesions. *The Journal of Neuroscience*, 36(7):2267–2282, 2016.

[102] Guo Li Ming, John Henley, Marc Tessier-Lavigne, Hong Jun Song, and Mu Ming Poo. Electrical activity modulates growth cone guidance by diffusible factors. *Neuron*, 29(2):441–452, 2001.

[103] Thomas M Brushart, Paul N Hoffman, Richard M Royall, Beth B Murinson, Christian Witzel, and Tessa Gordon. Electrical stimulation promotes motoneuron regeneration without increasing its speed or conditioning the neuron. *The Journal of Neuroscience*, 22(15):6631–6638, 2002.

[104] Colin D. McCaig, Ann M. Rajnicek, Bing Song, and Min Zhao. Has electrical growth cone guidance found its potential? *Trends in Neurosciences*, 25(7):354–359, 2002.

[105] G. Ibarretxe, D. Perrais, F. Jaskolski, A. Vimeney, and C. Mulle. Fast Regulation of Axonal Growth Cone Motility by Electrical Activity. *Journal of Neuroscience*, 27(29):7684–7695, 2007.

[106] Michael P. Willand, May-Anh Nguyen, Gregory H. Borschel, and Tessa Gordon. Electrical Stimulation to Promote Peripheral Nerve Regeneration. *Neurorehabilitation and Neural Repair*, 30(5):490, 2015.

[107] T E Kenedy, T Serafini, J R de la Torre, and M Tessier-Lavigne. Netrins are diffusable chemotropic factors for comissural axons in the embryonic spinal cord. *Cell*, 78:425–436, 1994.

[108] M Tessier-Lavigne and C S Goodman. The molecular biology of axon guidance. *Science*, 274(5290):1123–33, nov 1996.

[109] H Song and M Poo. The cell biology of neuronal navigation. *Nature Cell Biology*, 3(3):E81–E88, 2001.

[110] Yang Xiang, Yan Li, Zhe Zhang, Kai Cui, Sheng Wang, Xiao-bing Yuan, Chien-ping Wu, Mu-ming Poo, and Shumin Duan. Nerve growth cone guidance mediated by G protein-coupled receptors. *Nature Neuroscience*, 5(9):843–848, 2002.

[111] Kristian Franze, Jens Gerdelmann, Michael Weick, Timo Betz, Steve Pawlizak, Melike Lakadamyali, Johannes Bayer, Katja Rillich, Michael Gögler, Yun-Bi Lu, Andreas Reichenbach, Paul Janmey, and Josef Käs. Neurite branch retraction is caused by a threshold-dependent mechanical impact. *Biophysical Journal*, 97(7):1883–90, oct 2009.

[112] Kristian Franze. The mechanical control of nervous system development. *Development (Cambridge, England)*, 140(15):3069–77, aug 2013.

[113] A. Kamkin and I. Kiseleva, editors. *Mechanosensitivity of the Nervous System*. Springer New York, 2 edition, 2009.

[114] Robin J M Franklin and Timothy J. Bussey. Do your glial cells make you clever? *Cell Stem Cell*, 12(3):265–266, 2013.

[115] Nancy Ann Oberheim, Xiaohai Wang, Steven Goldman, and Maiken Nedergaard. Astrocytic complexity distinguishes the human brain. *Trends in Neurosciences*, 29(10):547–553, 2006.

[116] Xiaoning Han, Michael Chen, Fushun Wang, Martha Windrem, Su Wang, Steven Shanz, Qiwu Xu, Nancy Ann Oberheim, Lane Bekar, Sarah Betstadt, Alcino J. Silva, Takahiro Takano, Steven A. Goldman, and Maiken Nedergaard. Forebrain engraftment by human glial progenitor cells enhances synaptic plasticity and learning in adult mice. *Cell Stem Cell*, 12(3):342–353, 2013.

[117] Andrea Volterra, Nicolas Liaudet, and Iaroslav Savtchouk. Astrocyte Ca(2+) signalling: an unexpected complexity. *Nature Reviews. Neuroscience*, 15(5):327–35, 2014.

[118] Narges Bazargani and David Attwell. Astrocyte calcium signaling: the third wave. *Nature Neuroscience*, 19(2):182–9, 2016.

[119] Eliana Scemes and Christian Giaume. Astrocyte CalciumWaves: What They Are and What They Do. *Glia*, 54:716–725, 2006.

[120] J Silver and J H Miller. Regeneration beyond the glial scar. *Nature Reviews Neuroscience*, 5(2):146–156, 2004.

[121] Asya Rolls, Ravid Shechter, and Michal Schwartz. The bright side of the glial scar in CNS repair. *Nature Reviews. Neuroscience*, 10(3):235–41, 2009.

[122] Mark A. Anderson, Joshua E. Burda, Yilong Ren, Yan Ao, Timothy M. O'Shea, Riki Kawaguchi, Giovanni Coppola, Baljit S. Khakh, Timothy J. Deming, and Michael V. Sofroniew. Astrocyte scar formation aids central nervous system axon regeneration. *Nature*, 532(1):1–20, 2016.

[123] Pouria Moshayedi, Luciano da F Costa, Andreas Christ, Stephanie P Lacour, James Fawcett, Jochen Guck, and Kristian Franze. Mechanosensitivity of astrocytes on optimized polyacrylamide gels analyzed by quantitative morphometry. *Journal of Physics: Condensed Matter*, 22(19):194114, may 2010.

[124] Pouria Moshayedi, Gilbert Ng, Jessica C F Kwok, Giles S H Yeo, Clare E Bryant, James W Fawcett, Kristian Franze, and Jochen Guck. The relationship between glial cell mechanosensitivity and foreign body reactions in the central nervous system. *Biomaterials*, 35(13):3919–25, apr 2014.

[125] Michelle L. Previtera, Christopher G. Langhammer, and Bonnie L. Firestein. Effects of substrate stiffness and cell density on primary hippocampal cultures. *Journal of Bioscience and Bioengineering*, 110(4):459–470, 2010.

[126] Florent Ginhoux, Shawn Lim, Guillaume Hoeffel, Donovan Low, and Tara Huber. Origin and differentiation of microglia. *Frontiers in cellular neuroscience*, 7(April):45, 2013.

[127] Dirk Sieger, Christian Moritz, Thomas Ziegenhals, Sergey Prykhozhij, and Francesca Peri. Long-Range Ca2+ Waves Transmit Brain-Damage Signals to Microglia. *Developmental Cell*, 22(6):1138–1148, jun 2012.

[128] B. Hauss-Wegrzyniak, M.A. Lynch, P.D. Vraniak, and G.L. Wenk. Chronic Brain Inflammation Results in Cell Loss in the Entorhinal Cortex and Impaired LTP in Perforant Path-Granule Cell Synapses. *Experimental Neurology*, 176(2):336–341, 2002.

[129] D. Centonze, L. Muzio, S. Rossi, F. Cavasinni, V. De Chiara, A. Bergami, A. Musella, M. D'Amelio, V. Cavallucci, A. Martorana, A. Bergamaschi, M. T. Cencioni, A. Diamantini, E. Butti, G. Comi, G. Bernardi, F. Cecconi, L. Battistini, R. Furlan, and G. Martino. Inflammation Triggers Synaptic Alteration and Degeneration in Experimental Autoimmune Encephalomyelitis. *Journal of Neuroscience*, 29(11):3442–3452, 2009.

[130] Egle Solito and Magdalena Sastre. Microglia function in Alzheimer's disease. *Frontiers in Pharmacology*, 3 FEB(February):1–10, 2012.

[131] Elizabeth E. Spangenberg, Rafael J. Lee, Allison R. Najafi, Rachel A. Rice, Monica R P Elmore, Mathew Blurton-Jones, Brian L. West, and Kim N. Green. Eliminating microglia in Alzheimer's mice prevents neuronal loss without modulating amyloid-β pathology. *Brain*, 139(4):1265–1281, 2016.

[132] Kira Irving Mosher and Tony Wyss-Coray. Microglial dysfunction in brain aging and Alzheimer's disease, 2014.

[133] Alexei Verkhratsky and Arthur Butt. *Glial Physiology and Pathophysiology*. John Wiley and Sons, 2013.

[134] Douglas McHugh, Daniel Roskowski, Sisi Xie, and Heather B. Bradshaw. Delta9-THC and N-arachidonoyl glycine regulate BV-2 microglial morphology and cytokine release plasticity: Implications for signaling at GPR18. *Frontiers in Pharmacology*, 4:1–8, 2014.

[135] Wenwen Sheng, Yijia Zong, Arwa Mohammad, Deepa Ajit, Jiankun Cui, Dongdong Han, Jennifer L Hamilton, Agnes Simonyi, Albert Y Sun, Zezong Gu, Jau-Shyong Hong, Gary a Weisman, and Grace Y Sun. Pro-inflammatory cytokines and lipopolysaccharide induce changes in cell morphology, and upregulation of ERK1/2, iNOS and sPLA2-IIA expression in astrocytes and microglia. *Journal of Neuroinflammation*, 8(1):121, 2011.

[136] Olivier Pascual, Sarrah Ben Achour, Philippe Rostaing, Antoine Triller, and Alain Bessis. Microglia activation triggers astrocyte-mediated modulation of excitatory neurotransmission. *Proceedings of the National Academy of Sciences of the United States of America*, 109(4):E197–205, jan 2012.

[137] Ruben Orihuela, Christopher A. McPherson, and Gaylia Jean Harry. Microglial M1/M2 polarization and metabolic states. *British Journal of Pharmacology*, 173(4):649–665, 2016.

[138] Clyde Francks, Silvia Paracchini, Shelley D Smith, Alex J Richardson, Tom S Scerri, Lon R Cardon, Angela J Marlow, I Laurence MacPhie, Janet Walter, Bruce F Pennington, Simon E Fisher, Richard K Olson, John C DeFries, John F Stein, and Anthony P Monaco. A 77-kilobase region of chromosome 6p22.2 is associated with dyslexia in families from the United Kingdom and from the United States. *American journal of human genetics*, 75(6):1046–1058, 2004.

[139] Natalie Cope, Denise Harold, Gary Hill, Valentina Moskvina, Jim Stevenson, Peter Holmans, Michael J Owen, Michael C O'Donovan, and Julie Williams. Strong evidence that KIAA0319 on chromosome 6p is a susceptibility gene for developmental dyslexia. *The American Journal of Human Genetics*, 76(4):581, 2005.

[140] D Harold, S Paracchini, T Scerri, M Dennis, N Cope, G Hill, V Moskvina, J Walter, a J Richardson, M J Owen, J F Stein, E D Green, M C O'Donovan, J Williams, and a P Monaco. Further evidence that the KIAA0319 gene confers susceptibility to developmental dyslexia. *Molecular psychiatry*, 11(12):1085–1091, 1061, 2006.

[141] Silvia Paracchini, Colin D. Steer, Lyn Louise Buckingham, Andrew P. Morris, Susan Ring, Thomas Scerri, John Stein, Marcus E. Pembrey, Jiannis Ragoussis, Jean Golding, and Anthony P. Monaco. Association of the KIAA0319 dyslexia susceptibility gene with reading skills in the general population. *American Journal of Psychiatry*, 165(12):1576–1584, 2008.

[142] Jillian M. Couto, Izzy Livne-Bar, Katherine Huang, Zhaodong Xu, Tasha Cate-Carter, Yu Feng, Karen Wigg, Tom Humphries, Rosemary Tannock, Elizabeth N. Kerr, Maureen W. Lovett, Rod Bremner, and Cathy L. Barr. Association of reading disabilities with regions marked by acetylated H3 histones in KIAA0319. *American Journal of Medical Genetics, Part B: Neuropsychiatric Genetics*, 153(2):447–462, 2010.

[143] Tom S. Scerri, Andrew P. Morris, Lyn Louise Buckingham, Dianne F. Newbury, Laura L. Miller, Anthony P. Monaco, Dorothy V M Bishop, and Silvia Paracchini. DCDC2, KIAA0319 and CMIP are associated with reading-related traits. *Biological Psychiatry*, 70(3):237–245, 2011.

[144] Silvia Paracchini, Ankur Thomas, Sandra Castro, Cecilia Lai, Murugan Paramasivam, Yu Wang, Brendan J. Keating, Jennifer M. Taylor, Douglas F. Hacking, Thomas Scerri, Clyde Francks, Alex J. Richardson, Richard Wade-Martins, John F. Stein, Julian C. Knight, Andrew J. Copp, Joseph LoTurco, and Anthony P. Monaco. The chromosome 6p22 haplotype associated with dyslexia reduces the expression of KIAA0319, a novel gene involved in neuronal migration. *Human Molecular Genetics*, 15(10):1659–1666, 2006.

[145] Patrick D. Hsu, Eric S. Lander, and Feng Zhang. Development and applications of CRISPR-Cas9 for genome engineering. *Cell*, 157(6):1262–1278, 2014.

[146] Isabel Martinez-Garay, Luiz G. Guidi, Zoe G. Holloway, Melissa A. G. Bailey, Daniel Lyngholm, Tomasz Schneider, Timothy Donnison, Simon J. B. Butt, Antonio Velayos-Baeza, Zoltán Molnár, and Anthony P. Monaco. Normal radial migration and lamination are maintained in dyslexia-susceptibility candidate gene homolog Kiaa0319 knockout mice. *Brain Structure and Function*, 2016.

[147] Erik Meijering, Oleh Dzyubachyk, and Ihor Smal. Methods for cell and particle tracking. *Methods in Enzymology*, 504(February):183–200, 2012.

[148] Lars Bollmann, David E. Koser, Rajesh Shahapure, Hélène O. B. Gautier, Gerhard a. Holzapfel, Giuliano Scarcelli, Malte C. Gather, Elke Ulbricht, and Kristian Franze. Microglia mechanics: immune activation alters traction forces and durotaxis. *Frontiers in Cellular Neuroscience*, 9, 2015.

[149] Miriam Mecha. An easy and fast way to obtain a high number of glial cells from rat cerebral tissue: A beginners approach. *Protocol Exchange*, 49:1–12, mar 2011.

[150] H G Doebereiner, Benjamin J Dubin-Thaler, Grégory Giannone, Harry S Xenias, Michael P Sheetz, H G Dobereiner, and Hans-Günther Döbereiner. Dynamic Phase Transitions in Cell Spreading. *Physical Review Letters*, 93(10):108105, 2004.

[151] Benjamin J. Dubin-Thaler, Jake M. Hofman, Yunfei Cai, Harry Xenias, Ingrid Spielman, Anna V. Shneidman, Lawrence A. David, Hans Günther Döbereiner, Chris H. Wiggins, and Michael P. Sheetz. Quantification of cell edge velocities and traction forces reveals distinct motility modules during cell spreading. *PLoS ONE*, 3(11), 2008.

[152] H G Döbereiner, Benjamin J Dubin-Thaler, Gregory Giannone, and Michael P Sheetz. Force sensing and generation in cell phases: analyses of complex functions. *Journal of applied physiology (Bethesda, Md. : 1985)*, 98(4):1542–1546, 2005.

[153] Marie Gingras, Vicky Gagnon, Sandra Minotti, Heather D. Durham, and François Berthod. Optimized protocols for isolation of primary motor neurons, astrocytes and microglia from embryonic mouse spinal cord. *Journal of Neuroscience Methods*, 163(1):111–118, 2007.

[154] Rüben F. Iacono and Maria L. Berria. Cell differentiation increases astrocyte phagocytic activity a quantitative analysis of both gfap labeling and pas-stained yeast cells. *Medicina*, 59(2):171–175, 1999.

[155] L Lyck, I Dalmau, J Chemnitz, B Finsen, and H D Schroder. Immunohistochemical markers for quantitative studies of neurons and glia in human neocortex. *J Histochem Cytochem*, 56(3):201–221, 2008.

[156] Ronny Kalash, Hebist Berhane, Jeremiah Au, Byung Han Rhieu, Michael W. Epperly, Julie Goff, Tracy Dixon, Hong Wang, Xichen Zhang, Darcy Franicola, Ashwin Shinde, and Joel S. Greenberger. Differences in irradiated lung gene transcription between fibrosis-prone C57BL/6NHsd and fibrosis-resistant C3H/HeNHsd mice. *In vivo (Athens, Greece)*, 28(2):147–171, 2014.

[157] Bernice Grafstein. The nerve cell body response to axotomy. *Experimental Neurology*, 48(3 PART 2):32–51, 1975.

[158] J Wong and M M Oblinger. A comparison of peripheral and central axotomy effects on neurofilament and tubulin gene expression in rat dorsal root ganglion neurons. *The Journal of neuroscience : the official journal of the Society for Neuroscience*, 10(7):2215–2222, jul 1990.

[159] Ward Plunet, Brian K. Kwon, and Wolfram Tetzlaff. Promoting axonal regeneration in the central nervous system by enhancing the cell body response to axotomy. *Journal of Neuroscience Research*, 68(1):1–6, 2002.

[160] M E Schwab and D Bartholdi. Degeneration and regeneration of axons in the lesioned spinal cord. *Physiol. Rev.*, 76(2):319–370, apr 1996.

[161] Fang Sun and Zhigang He. Neuronal intrinsic barriers for axon regeneration in the adult CNS. *Current Opinion in Neurobiology*, 20(4):510–518, 2010.

[162] Frank Bradke, James W. Fawcett, and Micha E. Spira. Assembly of a new growth cone after axotomy: the precursor to axon regeneration. *Nature Reviews Neuroscience*, 13(3):183–193, 2012.

[163] Tessa Gordon. Electrical Stimulation to Enhance Axon Regeneration After Peripheral Nerve Injuries in Animal Models and Humans. *Neurotherapeutics*, 13(2):295–310, 2016.

[164] Fernando M. Mar, Azad Bonni, and Monica M. Sousa. Cell intrinsic control of axon regeneration. *EMBO Reports*, 15(3):254–263, mar 2014.

[165] Yuanquan Song, David Sretavan, Ernesto A Salegio, Jim Berg, Xi Huang, Tong Cheng, Xin Xiong, Shan Meltzer, Chun Han, Trong-tuong Nguyen, Jacqueline C Bresnahan, Michael S Beattie, Lily Yeh Jan, and Yuh Nung Jan. Regulation of axon regeneration by the RNA repair and splicing pathway. *Nature neuroscience*, 18(6):817–25, 2015.

[166] Marion Burland, Lambert Paris, Patrice Quintana, Jean Michel Bec, Lucie Diouloufet, Chamroeun Sar, Hassan Boukhaddaoui, Benoit Charlot, Jefferson Braga Silva, Michel Chammas, Victor Sieso, Jean Valmier, and Fabrice Bardin. Neurite growth acceleration of adult Dorsal Root Ganglion neurons illuminated by low-level Light Emitting Diode light at 645 nm. *Journal of Biophotonics*, 9(6):1–9, 2014.

[167] Qingzong Tseng. Template matching and slice alignment. https://sites.google.com/site/qingzongtseng/template-matching-ij-plugin, 2011. Accessed: 2016-02-01.

[168] D S Smith and J H Skene. A transcription-dependent switch controls competence of adult neurons for distinct modes of axon growth. *The Journal of neuroscience*, 17(2):646–658, jan 1997.

[169] Matthew O'Toole, Phillip Lamoureux, and Kyle E Miller. A physical model of axonal elongation: force, viscosity, and adhesions govern the mode of outgrowth. *Biophysical journal*, 94(7):2610–20, apr 2008.

[170] Daniel M. Suter and Kyle E. Miller. The emerging role of forces in axonal elongation. *Progress in Neurobiology*, 94(2):91–101, 2011.

[171] Wylie W Ahmed and Taher a Saif. Active transport of vesicles in neurons is modulated by mechanical tension. *Scientific reports*, 4:4481, 2014.

[172] T A Basarsky, V Parpura, and P G Haydon. Hippocampal synaptogenesis in cell culture: developmental time course of synapse formation, calcium influx, and synaptic protein distribution. *The Journal of Neuroscience : the Official Journal of the Society for Neuroscience*, 14(11):6402–6411, 1994.

[173] Zheng Li and Morgan Sheng. Some assembly required: the development of neuronal synapses. *Nature Reviews: Molecular Cell Biology*, 4(11):833–841, 2003.

[174] Shin-Ichi Nishikawa, Lars Martin Jakt, and Takumi Era. Embryonic stem-cell culture as a tool for developmental cell biology. *Nature reviews. Molecular cell biology*, 8(6):502–507, 2007.

[175] Charles E. Murry and Gordon Keller. Differentiation of Embryonic Stem Cells to Clinically Relevant Populations: Lessons from Embryonic Development. *Cell*, 132(4):661–680, 2008.

[176] Elaine Fuchs and J a Segre. Stem cells: a new lease on life. *Cell*, 100(1):143–155, 2000.

[177] D. E. Discher, D. J. Mooney, and P. W. Zandstra. Growth Factors, Matrices, and Forces Combine and Control Stem Cells. *Science*, 324(5935):1673–1677, 2009.

[178] Krishanu Saha, Albert J Keung, Elizabeth F Irwin, Yang Li, Lauren Little, David V Schaffer, and Kevin E Healy. Substrate modulus directs neural stem cell behavior. *Biophysical Journal*, 95(9):4426–38, 2008.

[179] Michele M Nava, Manuela T Raimondi, and Riccardo Pietrabissa. Controlling self-renewal and differentiation of stem cells via mechanical cues. *Journal of biomedicine & biotechnology*, 2012:797410, jan 2012.

[180] Jessica H Wen, Ludovic G Vincent, Alexander Fuhrmann, Yu Suk Choi, Kolin C. Hribar, Hermes Taylor-Weiner, Shaochen Chen, and Adam J Engler. Interplay of matrix stiffness and protein tethering in stem cell differentiation. *Nature Materials*, advance on(October):1–21, 2014.

[181] Shahzad Ali, Ivan B. Wall, Chris Mason, Andrew E. Pelling, and Farlan S. Veraitch. The effect of Young's modulus on the neuronal differentiation of mouse embryonic stem cells. *Acta Biomaterialia*, 25:253–267, 2015.

[182] Yubing Sun, Christopher S Chen, and Jianping Fu. Forcing stem cells to behave: a biophysical perspective of the cellular microenvironment. *Annual review of biophysics*, 41:519–42, 2012.

[183] Rowena McBeath, Dana M. Pirone, Celeste M. Nelson, Kiran Bhadriraju, and Christopher S. Chen. Cell shape, cytoskeletal tension, and RhoA regulate stem cell lineage commitment. *Developmental Cell*, 6(4):483–495, 2004.

[184] Lin Gao, Rowena McBeath, and Christopher S. Chen. Stem cell shape regulates a chondrogenic versus myogenic fate through rac1 and N-cadherin. *Stem Cells*, 28(3):564–572, 2010.

[185] Kristopher A Kilian, Branimir Bugarija, Bruce T Lahn, and Milan Mrksich. Geometric cues for directing the differentiation of mesenchymal stem cells. *Proceedings of the National Academy of Sciences of the United States of America*, 107(11):4872–7, 2010.

[186] Junmin Lee, Amr a Abdeen, Douglas Zhang, and Kristopher a Kilian. Directing stem cell fate on hydrogel substrates by controlling cell geometry, matrix mechanics and adhesion ligand composition. *Biomaterials*, 34(33):8140–8, nov 2013.

[187] Albert J. Keung, Elena M. De Juan-Pardo, David V. Schaffer, and Sanjay Kumar. Rho GTPases mediate the mechanosensitive lineage commitment of neural stem cells. *Stem Cells*, 29(11):1886–1897, 2011.

[188] Simon W. Moore, Pere Roca-Cusachs, and Michael P. Sheetz. Stretchy proteins on stretchy substrates: The important elements of integrin-mediated rigidity sensing. *Developmental Cell*, 19(2):194–206, 2010.

[189] Lia S Campos, Dino P Leone, Joao B Relvas, Cord Brakebusch, Reinhard Fassler, Ueli Suter, and Charles Ffrench-Constant. beta1 integrins activate a MAPK signalling pathway in neural stem cells that contributes to their maintenance. *Development*, 131(14):3433–3444, 2004.

[190] M A Schwartz and M H Ginsberg. Networks and crosstalk: integrin signalling spreads. *Nature Cell Biology*, 4(4):E65–8, 2002.

[191] S Cabodi, L Moro, E Bergatto, E Boeri Erba, P Di Stefano, E Turco, G Tarone, and P Defilippi. Integrin regulation of epidermal growth factor (EGF) receptor and of EGF-dependent responses. *Biochemical Society transactions*, 32:438–442, 2004.

[192] Lia Scotti Campos, Laurence Decker, Verdon Taylor, and William Skarnes. Notch, epidermal growth factor receptor, and beta1-integrin pathways are coordinated in neural stem cells. *Journal of Biological Chemistry*, 281(8):5300–5309, 2006.

[193] Fernanda M P Tonelli, Anderson K Santos, Dawidson A Gomes, Saulo L da Silva, Katia N Gomes, Luiz O Ladeira, and Rodrigo R Resende. Stem cells and calcium signaling. *Advances in experimental medicine and biology*, 740:891–916, 2012.

[194] Catherine Leclerc, Isabelle Néant, and Marc Moreau. The calcium: an early signal that initiates the formation of the nervous system during embryogenesis. *Frontiers in Molecular Neuroscience*, 5:1–12, 2012.

[195] Nic D. Leipzig and Molly S. Shoichet. The effect of substrate stiffness on adult neural stem cell behavior. *Biomaterials*, 30(36):6867–6878, 2009.

[196] P Shi, K Shen, S Ghassemi, J Hone, and LC Kam. Dynamic force generation by neural stem cells. *Cellular and Molecular Bioengineering*, 2(4):464–474, 2009.

[197] Jianping Fu, Yang-Kao Wang, Michael T Yang, Ravi A Desai, Xiang Yu, Zhijun Liu, and Christopher S Chen. Mechanical regulation of cell function with geometrically modulated elastomeric substrates. *Nature methods*, 7(9):733–6, 2010.

[198] Atossa Shaltouki, Jun Peng, Qiuyue Liu, Mahendra S. Rao, and Xianmin Zeng. Efficient generation of astrocytes from human pluripotent stem cells in defined conditions. *Stem Cells*, 31(5):941–952, 2013.

[199] Magdalena Chrzanowska-Wodnicka and Keith Burridge. Rho-stimulated Contractiliry Drives the Formation of Stress Fibers and Focal Adhesions. *The Journal of Cell Biology*, 133(6):1403–1415, 1996.

[200] Xiang Dong Ren, William B. Kiosses, and Martin Alexander Schwartz. Regulation of the small GTP-binding protein Rho by cell adhesion and the cytoskeleton. *EMBO Journal*, 18(3):578–585, 1999.

[201] Michael S Kolodney, Matthew S Thimgan, Henry M Honda, George Tsai, and Hal F Yee Jr. Rapid Report Ca ¥ -independent myosin II phosphorylation and contraction in chicken embryo fibroblasts. pages 87–92, 1999.

[202] Hal F. Yee, Andrew C. Melton, and Binh N. Tran. RhoA/rho-associated kinase mediates fibroblast contractile force generation. *Biochemical and biophysical research communications*, 280(5):1340–5, 2001.

[203] David W. Dumbauld, Heungsoo Shin, Nathan D. Gallant, Kristin E. Michael, Harish Radhakrishna, and Andrés J. García. Contractility modulates cell adhesion strengthening through focal adhesion kinase and assembly of vinculin-containing focal adhesions. *Journal of Cellular Physiology*, 223(3):746–756, 2010.

[204] Florian Schlosser, Florian Rehfeldt, and Christoph F Schmidt. Force fluctuations in three-dimensional suspended fibroblasts. *Philosophical Transactions of the Royal Society B: Biological Sciences*, 370(1661):20140028–20140028, 2014.

[205] Paul P Y Lu and Narendrakumar Ramanan. A Critical Cell-Intrinsic Role for Serum Response Factor in Glial Specification in the CNS. *Journal of Neuroscience*, 32(23):8012–8023, 2012.

[206] John T Connelly, Julien E Gautrot, Britta Trappmann, David Wei-Min Tan, Giacomo Donati, Wilhelm T S Huck, and Fiona M Watt. Actin and serum response factor transduce physical cues from the microenvironment to regulate epidermal stem cell fate decisions. *Nature Cell Biology*, 12(7):711–718, 2010.

[207] Marcel Schubert, Anja Steude, Philipp Liehm, Nils M. Kronenberg, Markus Karl, Elaine C. Campbell, Simon J. Powis, and Malte C. Gather. Lasing within Live Cells Containing Intracellular Optical Microresonators for Barcode-Type Cell Tagging and Tracking. *Nano Letters*, 15(8):5647–5652, 2015.

[208] Ying Xiong, Aih Cheun Lee, Daniel M Suter, and Gil U Lee. Topography and nanomechanics of live neuronal growth cones analyzed by atomic force microscopy. *Biophysical journal*, 96(12):5060–72, jun 2009.

Appendix A

Main Parts of the Optical Setup

- microscope: Eclipse Ti, Nikon
- monochromator: CM110, Spectral Products
- xy-stage: H117P2TE, Prior
- z-drive: H112, Prior
- LED: MWWHL3, Thorlabs
- sCMOS camera: Zyla 5.5, Andor
- CMOS camera: Icube NS4133BU, NET-GmbH

Appendix B

Refractive Index of the Elastomer

Elastomer samples of four different thicknesses were spin-coated on silicone substrates by Andrew Meek. Measurements were performed with a variable angle spectroscopy ellipsometer (J.A. Woollam Co.) at 45, 55, 65, 75 degrees over a wavelength range of 400–1500 nm by Laura Tropf. Sample thickness and refractive index $n(\lambda)$ were fitted assuming a Cauchy Model with:

$$n(\lambda) = A + \frac{B}{\lambda^2} + \frac{C}{\lambda^4}$$

$$A = 1.3978 \pm 0.0005$$

$$B = (3.97 \pm 0.05) \times 10^{-3}\,\mu\text{m}^2$$

$$C = (3.1 \pm 0.8) \times 10^{-5}\,\mu\text{m}^4$$

by Philipp Liehm.

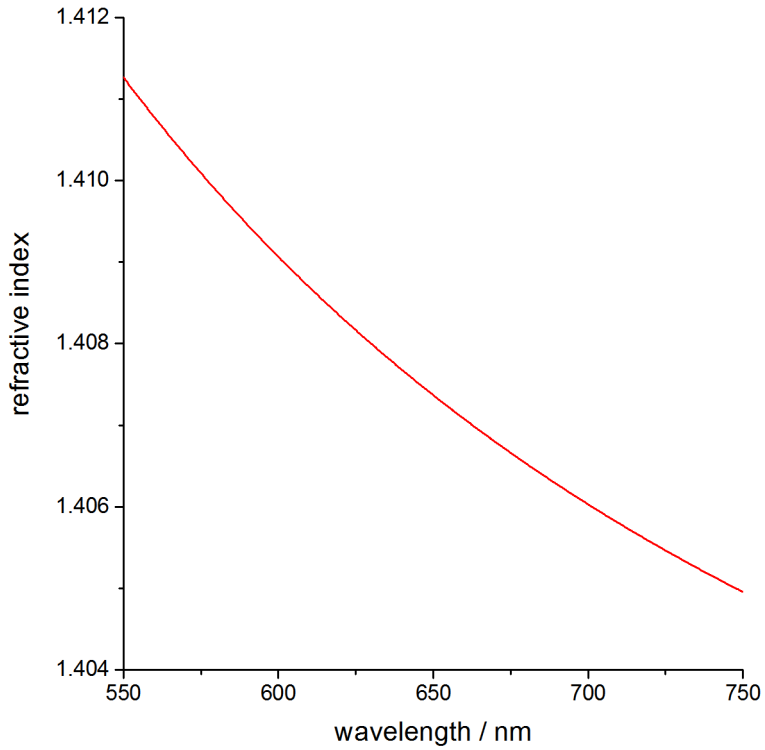

Figure B.1: Refractive index of the elastomer used for the fabrication of the ERISM microcavities.

Appendix C

Protocol for Antibody Staining

Protocol provided by Dr. Hélène O.B. Gautier (Cambridge).

1. Fix cells in 4% paraformaldehyde (PFA) in PBS, 10 min.
2. 4x 10 min PBS wash.
3. Blocking and permeabilisation: Bovine Serum Albumin 1 wt/v%, 0.1vol% triton X-100 in PBS, 1h.
4. Remove block and replace by primary antibody, just dilute in PBS. GFAP, 1:200; CD11b, 1:100.
5. Incubate overnight in fridge, or for 1 h at room temperature.
6. 4x 10 min PBS wash.
7. Secondary antibody: 1:1000 in PBS 1 h. Protect from light from now on.
8. 1x 10 min PBS wash.
9. 1x 10 min Hoechst 33342, e.g. 2 mM 10 µL per 1 ml PBS.
10. 2x 10 min PBS.